

**An Improved Zener-Hollomon Parameter and a New Ductile
Failure Criterion for Modeling and Predicting Sheet Metal
Forming Limit**

by

Ziqiang Sheng

**A dissertation submitted in partial fulfillment
of the requirements for the degree of
Doctor of Philosophy
(Automotive Systems Engineering)
in the University of Michigan – Dearborn
2017**

Doctoral Committee:

**Professor Pankaj Mallick, Chair
Professor Yubao Chen
Professor Ghassan Kridli
Associate Professor German Reyes-Villanueva**

© Ziqiang Sheng

All rights reserved

2017

DEDICATION

To my family and my career.

ACKNOWLEDGEMENTS

First, I would like to sincerely thank my advisor, Prof. Pankaj Mallick for his kindness, encouragement and guidance during this PhD study. It has been a great honor to be his graduate student. I appreciate all his contributions of time, ideas, and resources to make my graduate experience productive and stimulating. I would also like to express thanks and gratitude to my other dissertation committee members, Professor Yubao Chen, Professor Ghassan Kridli, Professor Elsayed Orady, and Professor German Reyes for their help in my PhD study at the University of Michigan - Dearborn.

Special thanks go to my previous supervisor Professor Talan Altan, the director at Center for Precision Forming (CPF) (formerly ERC for Net Shape Manufacturing) at the Ohio State University, for his encouragement on the proposed Ductile Failure Criterion. As he wrote in his email, “Your method for estimating the FLD, using mainly the tensile data, is very promising”. Also thanks to him for directing his PhD student Lei Wu to review, validate and implement the work at the CPF.

Thanks also go to the students in the Automotive Systems Engineering Program, such as Dr. Xuan Zhou, Ramzi Bazzi, Hiroyuki Nishihira, for having valuable discussion and cooperation during my graduate study. Also thanks to my friends, Dr. Lingyuan Kong, Dr. Jinchuan Li, and Dr. Chunlei Xie, who helped me in pursuing this PhD degree.

And last but not the least, I would like to thank my parents and my wife for all their loves, sacrifice and encouragement. Their faithful support during this study is very much appreciated. Thank you.

TABLE OF CONTENTS

| | |
|--|-----|
| DEDICATION | i |
| ACKNOWLEDGEMENTS | ii |
| LIST OF FIGURES | ix |
| LIST OF TABLES | xii |
| ABSTRACT | xiv |
| CHAPTER 1: Introduction | 1 |
| 1.1 Literature review on forming limit at room and elevated temperatures..... | 2 |
| 1.2 Problem statement, research objectives and strategies | 5 |
| 1.3 Dissertation Outline | 6 |
| 1.4 References:..... | 8 |
| CHAPTER 2: Developing a Zener-Hollomon based Forming Limit Surface for Warm Forming of Magnesium Sheet Material | 10 |
| 2.1 Introduction..... | 10 |
| 2.2 Zener-Hollomon Based Forming Limit Surface (Z-FLS)..... | 12 |
| 2.3 Construction of Z-FLS for AZ31 Magnesium Alloy | 14 |
| 2.4 Fracture Prediction Using Z-FLS..... | 18 |

| | |
|--|--------|
| 2.4.1 Flow stress modeling | 19 |
| 2.4.2 FEM modeling of round cup forming..... | 21 |
| 2.4.3 Results and Analysis | 23 |
| 2.5 Conclusions..... | 32 |
| 2.6 References:..... | 33 |
| CHAPTER 3: An Improved Zener-Hollomon Parameter (Z') and Implementation of Z' - FLS in Hot Stamping | 36 |
| 3.1 Introduction..... | 36 |
| 3.2 Improved Zener-Hollomon parameter (Z')..... | 36 |
| 3.2.1 Determination of s | 38 |
| 3.2.2 Validation of Z' | 39 |
| 3.3 Z' -FLS and its implementation in Hot stamping | 42 |
| 3.3.1 Literature review on forming limit in Hot Stamping | 43 |
| 3.3.2 Z' -FLS for boron Steel..... | 46 |
| 3.3.3 Prediction of failure in Hot Stamping | 49 |
| 3.4 Conclusions and discussion | 57 |
| 3.5 References:..... | 58 |
| CHAPTER 4: A New Ductile Failure Criterion for Predicting Sheet Metal Forming Limit | 60 |
| 4.1 Introduction..... | 60 |

| | |
|---|----|
| 4.2 Stretching failure and Critical damage | 65 |
| 4.2.1 Stretching failure..... | 65 |
| 4.2.2 Critical damage | 67 |
| 4.3 A ductile failure criterion..... | 68 |
| 4.3.1 Model..... | 68 |
| 4.3.2 Calculation limit strains at liner strain path | 70 |
| 4.3.3 Determination of $f(t,0)$ and $f(t,1)$ | 72 |
| 4.3.3 Parametric study..... | 73 |
| 4.3.4 Working under Non-linear strain path | 74 |
| 4.4 Calculation of FLCs under proportional strain path | 74 |
| 4.4.1 Calculation procedure | 74 |
| 4.4.2 Results and discussion | 76 |
| 4.5 Calculation of FLCs under bilinear strain path..... | 82 |
| 4.6 Prediction failure in FEM simulation under non-linear strain path | 84 |
| 4.6.1 Experimental setup..... | 85 |
| 4.6.2 FEM modeling | 86 |
| 4.6.3 Results and discussion | 87 |
| 4.7 Conclusions and discussion | 92 |
| 4.8 References:..... | 94 |

| | |
|---|-----|
| CHAPTER 5: Predicting Forming Limit of Aluminum Alloys at Elevated Temperatures by Using an Improved Ductile Failure Criterion | 99 |
| 5.1 Introduction..... | 99 |
| 5.2 Effect function at elevated temperatures..... | 102 |
| 5.3 Calculation of Forming Limit Curves..... | 104 |
| 5.3.1 Procedure | 104 |
| 5.3.2 Calculation FLCs for 1.0mm thick JIS-A5083P-O..... | 105 |
| 5.4 Predicting failure in FEM simulation | 106 |
| 5.5 Rectangular cup warm forming..... | 107 |
| 5.5.1 FEM model | 109 |
| 5.5.2 Modeling flow stress..... | 110 |
| 5.5.3 Calibration the DFC criterion | 112 |
| 5.5.4 Results and discussion | 113 |
| 5.6 Conclusions and discussion | 118 |
| 5.7 References:..... | 119 |
| CHAPTER 6: Conclusions and Recommendations of Future Work | 122 |
| PUBLICATIONS AND PRESENTATIONS | 124 |
| APPENDIX A: NADDRG Formula | 125 |
| APPENDIX B: Hill-Stören Rice (H-SR) Formula | 126 |
| APPENDIX C: Algebraic transformation of DFC..... | 127 |

| | |
|--|-----|
| APPENDIX D: Calculation FLC based on Oyane’s criterion | 129 |
| APPENDIX E: Abbreviations of approaches and tests of Benchmark #1 of Numisheet 2008 and 2014..... | 130 |
| APPENDIX F: Script for Damage Calculation in LS-Prepost | 132 |

LIST OF FIGURES

| | |
|--|----|
| Figure 1.1 Fracture mechanism maps (Ashby et al. 1979) | 4 |
| Figure 1.2 Main body of the dissertation | 7 |
| Figure 2.1 Forming limit curves (FLCs) of AZ31B as reported in References (Chen and Huang 2003) and (Abu-Farha et al. 2012) used for constructing Z-FLS shown in Figure 2.3 | 15 |
| Figure 2.2 Plots of material constants A, B, C under different minor strains | 17 |
| Figure 2.3 Z-FLS for AZ31B magnesium alloy | 17 |
| Figure 2.4 FLCs constructed using the Z-FLS in Figure 2.3 and compared with data reported in References ((Bruni et al. 2010) and (Hsu et al. 2008)) | 18 |
| Figure 2.5 Flow stress curves: a) at temperatures from 25 to 235°C and strain rate of 0.002/s, b) at temperature 200°C and strain rates from 0.002 to 2.0/s (Dröder 1999, Palaniswamy et al. 2004), c) calculated at strain rate of 0.01/s using Eq. (2.9) | 21 |
| Figure 2.6 Finite element model of round cup draw | 22 |
| Figure 2.7 Predicted punch load curves at different temperatures for draw ratio of 2.3 compared with experimental data in (Dröder 1999, Palaniswamy et al. 2004) | 26 |
| Figure 2.8 Comparison of simulated values of thinning (% change in thickness) at a draw ratio of 2.3 with experimental data in (Dröder 1999, Palaniswamy et al. 2004) | 27 |
| Figure 2.9 Fracture identification in drawn cups with the aid of the Z-FLS in Figure 2.3 | 29 |
| Figure 2.10 Historical data of elements on the Z-FLS (200°C, DR = 2.575) | 32 |
| Figure 2.11 LDRs at different warm forming temperatures (punch diameter = 100 mm and blank thickness 1.3 mm) | 32 |
| Figure 3.1 Limit strains as polynomial functions of $\ln(Z)$ and $\ln(Z')$ for Al5xxx (test set A) | 40 |
| Figure 3.2 Limit strains as polynomial functions of $\ln(Z)$ and $\ln(Z')$ for Al5182+Mn (test set B) | 40 |
| Figure 3.3 Limit strains as polynomial functions of $\ln(Z)$ and $\ln(Z')$ for Al5754 (test set C) | 41 |
| Figure 3.4 Limit strains as polynomial functions of $\ln(Z)$ and $\ln(Z')$ for Al6111-T4 (test set D) | 41 |
| Figure 3.5 Limit strains as polynomial functions of $\ln(Z)$ and $\ln(Z')$ for Al5083-O (test set E) | 41 |

| | |
|--|-----|
| Figure 3.6 Limit strains as polynomial functions of $\ln(Z)$ and $\ln(Z')$ for AZ31 (test set F) | 42 |
| Figure 3.7 Limit strains as polynomial functions of $\ln(Z)$ and $\ln(Z')$ for boron steel (test set G) | 42 |
| Figure 3.8 Test equipment and obtained FLCs of boron steel sheet material at elevated temperatures (Cui et al. 2015) | 47 |
| Figure 3.9 Constructed FLS for 1.5mm thick Boron steel sheet material | 48 |
| Figure 3.10 NUMISHEET 2008 #3 B-Pillar hot stamping tooling and FEM model | 49 |
| Figure 3.11 Baseline flow stress curves boron steel 22MnB5 at strain rate of 0.1/s (Shapiro 2009) | 51 |
| Figure 3.12 Temperature distribution of numerically formed B-Pillar part | 53 |
| Figure 3.13 a) thickness distribution in simulation; b-g) comparison of thickness distribution of parts formed in simulation and physical part from experiment at six cross sections from (Oberpriller et al. 2008) | 54 |
| Figure 3.14 Fracture identification in hot forming B-Pillar part with the aid of Z' -FLS | 56 |
| Figure 3.15 Fracture/necking prediction by traditional criteria | 57 |
| Figure 4.1 Schematic diagram for FLC and FFLC | 61 |
| Figure 4.2 Effect of initial sheet thickness and strain path on: a. effect function; b. major limit strain | 74 |
| Figure 4.3 FLCs predicted by the proposed ductile failure criterion (solid line) and experimental measurements (circles) | 78 |
| Figure 4.4 Illustration of the difference between calculated FLC and measured data points | 78 |
| Figure 4.5 FLCs measured from test and calculated by using algorithm of present study and two representative submissions of Numisheet 2008 BM#1 (Volk 2008) | 81 |
| Figure 4.6 Calculated FLCs and experimentally measured FLCs: a) as-received and calculated at with different equivalent biaxial pre-strains; b) as-received and calculated at with different uniaxial tension pre-strains; c – h give comparison between calculation and measurement on each pre-strain condition. | 83 |
| Figure 4.7 Experimental setup for Benchmark #1 of Numisheet 2014 (Wu 2013) | 85 |
| Figure 4.8 Simulation model for Numisheet 2014 BM1 | 86 |
| Figure 4.9 Comparison of Punch load trajectories from simulation prediction and experimental measurement | 88 |
| Figure 4.10 Damage distribution at moment of LN initiation and identified location of LN | 88 |
| Figure 4.11 Strain paths of the element at LN from simulation prediction and experimental measurement | 89 |
| Figure 4.12 Comparison of limit strains and initial locations at LN from calculations and experiment | 92 |
| Figure 5.1 Plots of adjust function at two critical strain paths | 103 |

| | |
|---|-----|
| Figure 5.2 Calculated FLCs (solid markers and solid line) and data points (unfilled markers) from tests at different temperatures and strain rates for sheet material JIS-A5083P-O | 106 |
| Figure 5.3 Experimental and simulation setup for warm forming: (a) experimental tooling setup; (b) a quarter of simulation model setup. Dimensions are listed in Table 5.3 (Li and Ghosh 2004) | 108 |
| Figure 5.4 Flow stress curves for Al5182+Mn at elevated temperatures – solid line and round marked curves are calculated from Eq.(5.11); in a and b, dash line and triangular marked curves are from tensile test (Li and Ghosh 2004) | 112 |
| Figure 5.5 Comparison on in-plane principal strain distribution at failure depth of 21.0mm | 114 |
| Figure 5.6 Damage prediction on the case 1 | 115 |
| Figure 5.7 Prediction on the case 1:a. temperature distribution at draw depth of 21.0mm; b. effective strain rate distribution at draw depth of 21.0mm | 116 |
| Figure 5.8 Evolution of damage of the critical element | 117 |
| Figure 5.9 Damage prediction on the case 2 | 118 |

LIST OF TABLES

| | |
|--|----|
| Table 2.1 Major limit strains at different minor limit strains, temperature and strain rates * | 16 |
| Table 2.2 Material parameters C and P in the Cowper and Symonds equation | 21 |
| Table 2.3 Boundary conditions and material properties used in the simulation of round cup drawing (Doege and Dröder 2001, Palaniswamy et al. 2004) | 23 |
| Table 2.4 Thermal properties of AZ31 sheet material and tool material (Palaniswamy et al. 2004) | 23 |
| Table 2.5 Predicted temperature distribution on the cup being drawn at 200°C | 25 |
| Table 2.6 Failure status of representative elements in non-isothermal cup draw test | 29 |
| Table 3.1 Test conditions of seven sets of tests | 39 |
| Table 3.2 Material data used for calculating data points in Figure 3.1-7 and resulted s and R^2 | 42 |
| Table 3.3 Chemical composition of 22MnB5 (wt. %) | 47 |
| Table 3.4 Data for constructing Z'-FLS | 49 |
| Table 3.5 Dimensions and material properties of boron steel sheet material | 51 |
| Table 3.6 Material parameters C and P of boron steel sheet material (Shapiro 2009) | 51 |
| Table 3.7 Boundary conditions (Oberpriller et al. 2008) | 52 |
| Table 4.1 Post-necking (P-N) deformation in percentage of eight sheet metal materials | 66 |
| Table 4.2 Determined material constants for the effect functions | 72 |
| Table 4.3 Mechanical properties, thickness of the sheet materials used for the case study | 75 |
| Table 4.4 Deviations in true strain from measurement at three critical strain paths by using present algorithm | 79 |
| Table 4.5 Comparison on the deviations (total and breakdown) in true strain of calculated FLCs of three sheet materials from Numisheet 2008 BM1 | 80 |
| Table 4.6 Tensile properties of A-K sheet steel (Ghosh and Laukonis 1976) | 82 |
| Table 4.7 Material properties of 1.05mm thick TRIP780 | 87 |

| | |
|---|-----|
| Table 5.1 Chemical composition of JIS-A5083-P-O (wt.%) (Naka et al. 2001) | 103 |
| Table 5.2 Chemical composition of Al 5182+Mn (wt.%) (Li and Ghosh 2003) | 108 |
| Table 5.3 Dimensions of the tools and boundary conditions in simulation (Li and Ghosh 2004) | 109 |
| Table 5.4 Material parameters C and P in the Cowper and Symonds equation | 112 |
| Table E1 Approaches used in Numisheet 2008 Benchmark #1 (Volk et al. 2008) | 130 |
| Table E2 Approaches used in Numisheet 2014 Benchmark #1(Wu 2013) | 131 |
| Table E3 Abbreviations of test on TRIP780 sheet material in Numisheet 2014 Benchmark #1 | 131 |

ABSTRACT

Sheet metal forming is an important manufacturing process in the automotive industry. Due to the lightweighting trend, increasing amount of sheet metal materials with high strength-to-weight ratios, such as aluminum alloys, magnesium alloys, advanced high strength steel (AHSS), are being used to make automotive components. However, the room temperature formability of those sheet materials is generally inferior to that of conventionally used mild steel. Recent decade has witnessed a fast development of sheet metal forming technologies at elevated temperatures or so-called warm/hot forming that take advantage of the enhanced formability at elevated temperatures for those light weighting sheet materials. Sheng (2102) proposed a Zener-Hollomon (Z) parameter based forming limit surface (Z-FLS) to model the forming limit at elevated temperatures of aluminum warm forming. Further development of this concept motivated this PhD dissertation.

The current research started with the implementation of Z-FLS for the formability prediction of a magnesium alloy under a warm forming condition. It then proposed an improved Zener-Hollomon (Z') parameter to enhance the capability of representing non-linear strain rate effect on the forming limit strain and used the Z' -FLS concept to predict the formability of a boron steel sheet material in a hot stamping condition. Furthermore, it proposed a new ductile failure criterion (DFC) to correctly reflect micromechanical findings on critical damage and failure. It also developed methods to predict forming limit

curves at room and elevated temperatures by using the proposed DFC and Z' . The proposed new Zener-Hollomon parameter and ductile fracture criterion were validated using published test data on different lightweighting sheet materials. It is shown that the forming limit predictions match quite well with the experimental observations.

CHAPTER 1: Introduction

Sheet metal materials with high strength-to-weight ratios, such as aluminum alloys, magnesium alloys, and advanced high strength steels (AHSS), are being used increasingly to make lightweighting automotive components (Mallick 2010). Due to limited sliding system and/or more obstacles to dislocation movement, compared to traditional low carbon sheet steels, these materials generally have inferior formability at room temperature (Sheng and Shivpuri 2006^{1,2}). Sheet metal forming at elevated temperatures or so-called warm/hot forming is used to form components from these lightweighting materials (Neugebauer et al. 2006, Karbasian and Takkaya 2010, Toros et al. 2008, Tabbe and Kridli 2004). In recent years, the automotive industry has witnessed a significant increase in the usage of hot/warm stamped sheet metal parts, such as hot stamped rear rails, B-pillars and A-pillars of boron steel (Karbasian and Takkaya 2010), hot blow formed decklid panels of AA5083, and hot blow formed hood inner panel of AZ31B (Carter et al. 2008).

At elevated temperatures, the formability is enhanced through the activation of additional sliding systems and reduction of defect growth by recovery (Doege and Dröder 2001, Turetta et al. 2006). Since the thermal recovery is rate-sensitive, the formability depends on both strain rate and temperature (Naka et al. 2001, Banabic 2010). Forming simulations based on finite element method are widely used to design and improve sheet metal forming processes at room and elevated temperatures (Sheng et al. 2004, Kim et al. 2006, Oberpriller et al. 2008). To identify fracture or necking failure on the numerically

formed parts, it is essential that the forming limit model can reflect the effect of temperatures and different strain rates during forming.

1.1 Literature review on forming limit at room and elevated temperatures

A brief review of sheet forming limit at room and elevated temperatures is given in this section. Detail review of the start-of-the-art on each related topic will be given in following chapters.

Due to relatively small sheet thickness and contact pressure in the thickness direction, stretching-driven sheet metal forming takes place under plane-stress mode, in which ductile sheet materials usually fail by localized necking (LN), followed by fracture (Chung et al. 2014). Research studies on the forming limits of sheet metal materials started in the 1940s (Gensamer 1944). However, a better understanding of the limits of formability started to occur in the 1960s when the concept of forming limit diagram (FLD) was developed using the major and minor surface strains as the two co-ordinate axes (Keeler, Backofen 1964, Goodwin 1968). To construct FLD, experimentally determined major limit strains at LN are plotted against minor strains and approximated into a so-called Forming Limit Curve (FLC). Since then, a large body of research has appeared in the literature on both mechanics and mechanisms of stretching failure in sheet metal forming at room temperature. Currently, there are three approaches to represent forming limits: 1) the amount of deformation, such as principal strain based Forming Limit Diagram (FLD) or Keeler-Goodwin diagram (Keeler and Backofen 1964, Goodwin 1968), 2) resistance to the deformation, such as principal stress based Forming Limit Diagram (Stoughton 2000), and 3) accumulation of damage, which can be either empirically represented based on energy consideration (Cockcroft, & D.J. Latham 1968, Brozzo et al. 1972) or based on

microscopic void growth (McClintock 1968, Rice and Tracey 1969). A good review of type 1 and 2 forming limits and related studies was given by Stoughton and Zhu (2004) while Atkins (1996) gave a good discussion of type 3 forming limit. A comprehensive discussion of all three types of forming limits is given by Bruschi et al. (2014).

Studies of the forming limit of sheet materials at elevated temperatures started with 5xxx aluminum alloys in the 1970s (Shehata et al. 1978), with magnesium alloys in the late 1990s (Doege and Dröder 2001, Takuda et al. 1998), and recently with press hardening boron steels (Geiger et al. 2005, Turetta et al. 2006). Disregarding the difference in their microstructures, several generally accepted points are as follows.

- 1) Most warm/hot forming operations are conducted in the homologous temperature range of 0.1 to 0.7 T_m and strain rates ranging from 10^{-4} to 10^1 s^{-1} . According to the Fracture Mechanism Maps developed by Ashby et al. (1979), fracture modes of warm/hot forming sheet materials of aluminum alloys, magnesium alloys, and boron steels can be generally categorized as ductile fracture and trans-granular creep fracture (Figure 1.1).
- 2) Strain based forming limit curves (FLCs) are used to report failure in sheet metal forming in warm/hot forming operations (Naka et al 2001, Hsu et al. 2008, Min et al. 2010). Due to the dynamic recovery at elevated temperatures, the material softens and may deform by creep mechanism, and thus the stress components, such as yield stress, may exhibit non-monotonic feature at elevated temperatures. The usage of strain based criterion can avoid the confusion caused by the non-monotonic feature of stress components.

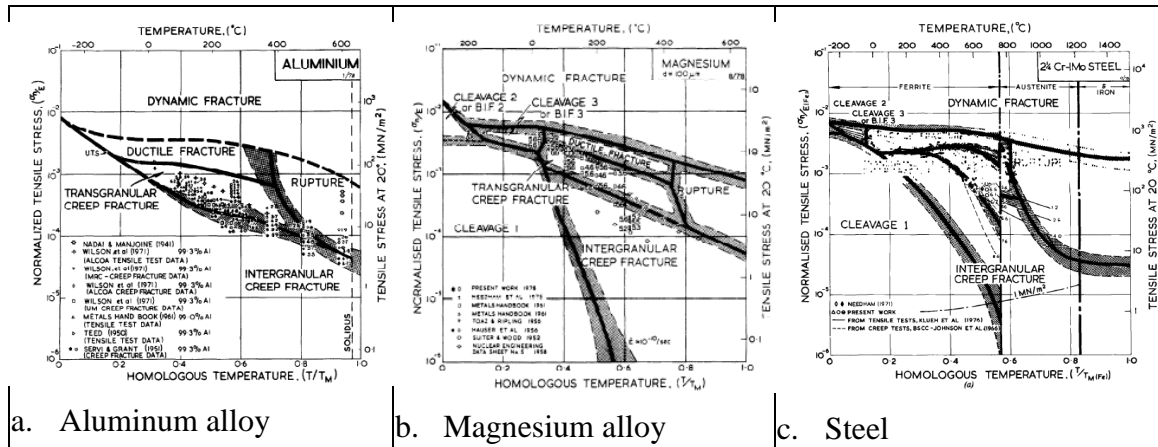


Figure 1.1 Fracture mechanism maps (Ashby et al. 1979)

3) Despite different loading paths, e.g. uniaxial tension to biaxial stretch, the strain at stretching failure increases with increasing temperature and decreasing strain rate (Doerge, Dröder 2001, Turetta et al. 2006, Naka et al. 2001, Li and Ghosh 2004, Bruni et al. 2010). From continuum mechanics point of view, the improvement of forming limit can be attributed to the increase of strain rate hardening at elevated temperatures (Abedrabbo et al. 2007).

4) The formability is affected by the direction of texture developed by the rolling processes. At temperature 400°C (Abu-Farha et al. 2012) and temperature of 200-300°C (Bruni et al. 2010), the forming limit curves of magnesium alloy AZ31 sheet material are generally greater in the rolling direction.

Due to variation in tooling speed and heat transfer between the sheet and the tool, warm forming is, in general a non-isothermal process, which creates spatially and temporally different distribution of strain rates and temperatures on the sheet during the forming operation (Karbasiyan and Tekkaya 2010, Doerge and Dröder 2001, Kim et al. 2006, Zhang et al. 2006, Yoshihara et al. 2003, Chen et al. 2003). Thus, the prediction of

stretching failure in non-isothermal forming requires a continuous representation of forming limits that vary with strain rate and temperature. Three-dimensional forming limit diagrams with either temperature (Krauer et al. 2007) or strain rate (Kröhn et al. 2007, Abu-Farha 2011) as the third axis have been proposed. A three-dimensional forming limit surface that takes into account both temperature and strain rate was proposed by Sheng (2012). In this concept, the Zener-Hollomon parameter (Z), or the so-called temperature-compensated strain rate (Zener and Hollomon 1947), is used to represent the effects of strain rate and temperature on the forming limit. The three-dimensional FLS, which is termed Z-FLS in the current study, was based on the observation that the major limit strains on the forming limit curves of aluminum alloy 5083-O sheet at different strain rates and temperatures can be described as a function of $\ln(Z)$.

1.2 Problem statement, research objectives and strategies

As discussed, the sheet formability in warm and hot forming depends on strain rate and temperature while both temperature and strain rate change continuously as the heated sheet is being formed. It thus becomes important to model the forming limit to reflect their effects on formability. The use of Zener-Hollomon parameter Z as proposed by Sheng (2012) allows to model the forming limit as a function of temperature and strain rate using limited, but selected number of FLCs. Sheng has demonstrated the application of Z in the modeling of a three-dimensional Z-FLS diagram for an aluminum alloy. Its applicability to other lightweighting alloys in non-isothermal forming conditions has not been demonstrated. Furthermore, the Zener-Hollomon parameter considers only a linear effect of strain rate; however, in reality, the strain rate effect can be very non-linear, especially when a wide range of strain is considered, and also varies significant differently among

different sheet metal materials. Another aspect of predicting forming limit is the effects of initial sheet thickness and strain path dependency on the critical damage, both of which are not considered by the available ductile failure criteria that can be applied to forming limit prediction either at room temperature or at elevated temperatures.

Based on the above observations regarding modeling and predicting forming limit under room temperature and/or elevated temperatures, the following objectives were formulated for the current research.

- (1) Demonstrate the application of Z-FLS in predicting formability of a magnesium alloy in non-isothermal warm forming
- (2) Improve the Z-FLS approach by taking into account the varying nonlinear effect of strain rate of the sheet metal materials and demonstrate its application in predicting formability of a boron steel under hot stamping conditions
- (3) Develop a new ductile failure model that takes into account the initial sheet thickness and strain path effect on the formability of sheet metals under both room temperature and elevated temperature forming conditions.

1.3 Dissertation Outline

Accordingly, as shown in Figure 1.2, the main body of this dissertation consists of three parts: 1) construction and application of *Z-FLS* to non-isothermal warm forming of a magnesium alloy, 2) development of an improved Z parameter, which is termed *Z'* in this research, and implementation of *Z'-FLS* to hot stamping and 3) development of a Ductile Failure Criterion (DFC) for modeling forming limit at room temperature and elevated temperatures. This is shown in Figure 1.2.

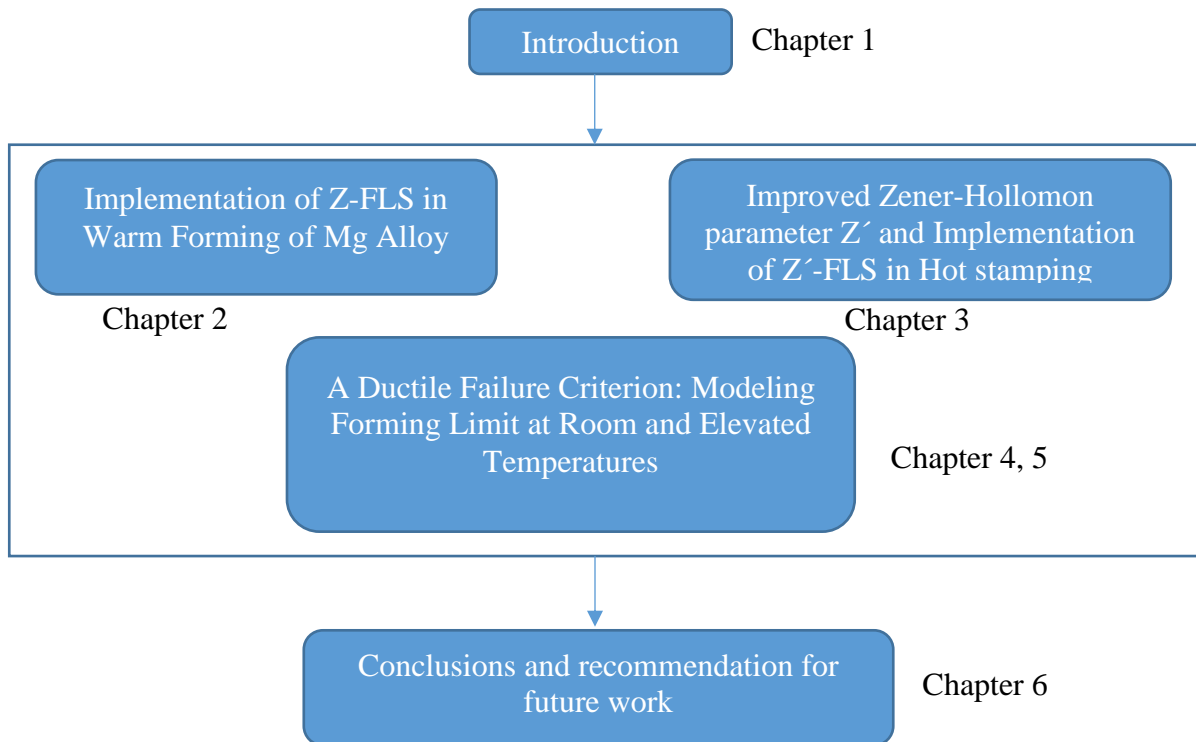


Figure 1.2 Main body of the dissertation

After giving a brief introduction of the background of this study in Chapter 1, Chapter 2 introduces the construction of a Z-FLS for magnesium alloy AZ31B and its implementation to predict failure in a warm forming process. In Chapter 3, an improved Zener-Hollomon parameter (Z') is proposed to represent the non-linear strain rate effect on limit strain and a Z' -FLS is constructed for boron steel sheet material 22MnB5. The Z' -FLS is then used to predict failure in a Numisheet benchmark hot stamping process. Chapter 4 proposes a Ductile Failure Criterion (DFC) for predicting forming limit of sheet materials and validated the criterion by predicting limit strains under linear and nonlinear strain paths for different steels and aluminum alloys. In Chapter 5, the proposed new DFC is modified by the Z' parameter and used to predict forming limits of aluminum alloys in a warm forming condition. Chapter 6 gives conclusions and summarizes contributions of this dissertation, and also gives recommendations for future work.

1.4 References:

- Alexandrov, S., Wang, P.T., and Roadman R.E. 2005. A Fracture Criterion of Aluminum Alloys in Hot Metal Forming, *J. Mat. Processing Tech.*, 160, p 257-265
- Ashby, M.F., Gandhi, C. and Taplin, D. M. R. 1979. Overview No. 3 Fracture-mechanism maps and their construction for fcc metals and alloys. *Acta Metallurgica* 27, no. 5. p. 699-729.
- Banabic D. 2010. *Sheet metal forming processes: constitutive modelling and numerical simulation*. Springer Science & Business Media.
- Bruschi, S., Altan, T., Banabic, D., Bariani, P. F., Brosius, A., Cao, J., & Tekkaya, A. E. 2014. Testing and modelling of material behaviour and formability in sheet metal forming. *CIRP Annals-Manufacturing Technology*,63(2), p.727-749.
- Chung, K., Kim, H., & Lee, C. 2014. Forming limit criterion for ductile anisotropic sheets as a material property and its deformation path insensitivity. Part I: Deformation path insensitive formula based on theoretical models. *International Journal of Plasticity*, 58, p.3-34.
- Doege, E., & Dröder, K. 2001. Sheet metal forming of magnesium wrought alloys—formability and process technology. *Journal of Materials Processing Technology*, 115(1), p.14-19.
- Karbasian, H. & Tekkaya, A. E., 2010. A review on hot stamping. *Journal of Materials Processing Technology*, 210(15), p.2103-2118.
- Kim, H.K. and Kim, W.J., 2010. Failure prediction of magnesium alloy sheets deforming at warm temperatures using the Zener-Holloman parameter. *Mechanics of Materials*, 42(3), p.293-303.
- Kröhn, M.A., Leen, S.B. and Hyde, T.H., 2007. A superplastic forming limit diagram concept for Ti-6Al-4V. *Proceedings of the Institution of Mechanical Engineers, Part L: Journal of Materials Design and Applications*, 221(4), p.251-264.
- Li, D., Ghosh, A. 2004. Biaxial warm forming behavior and stretchability of sheet alloys, *J. Mater. Process. Technol.* 145, pp.281-293. DOI: 10.1016/j.jmatprotec.2003.07.003
- Mallick, P.K. (Ed.). 2010. *Materials, design and manufacturing for lightweight vehicles*. Elsevier.
- Naka T., Torikai G., Hino R., Yoshida F. 2001. The effects of temperature and forming speed on the forming limit diagram for type 5083 aluminum-magnesium alloy sheet, *J. of Mat. Proc. Technol.*, 113, p.648-653.
- Neugebauer, R., Altan, T., Geiger, M., Kleiner, M., Sterzing, A. 2006. Sheet metal forming at elevated temperatures, *CIRP Annals-Manufacturing Technology* 55(2), p. 793-816
- Sheng, Z. Q., Jirathearanat, S., & Altan, T. 2004. Adaptive FEM simulation for prediction of variable blank holder force in conical cup drawing. *International Journal of Machine Tools and Manufacture*, 44(5), p.487-494.
- Sheng, Z. Q., & Shivpuri, R. 2006¹. Modeling flow stress of magnesium alloys at elevated temperature. *Materials Science and Engineering: A*, 419(1), p.202-208.
- Sheng Z.Q., and Shivpuri R. 2006². A Hybrid Process for Forming Thin-Walled Magnesium Parts, *Mater. Sci. Eng.*, A428, p. 180-187.
- Sheng Z.Q. 2012. A Temperature and Time Dependent Forming Limit Surface for Sheet Metal Forming at Elevated Temperatures. *SAE International J. of Materials & Manufacturing*, 5.2, p. 277-284.

Tebbe, P.A., Kridli, G.T. 2004. Warm forming of aluminium alloys: an overview and future directions. *International Journal of Materials and Product Technology*, 21(1), p. 24-40.

Toros, S., Ozturk, F., & Kacar, I. 2008. Review of warm forming of aluminum–magnesium alloys. *Journal of materials processing technology*, 207(1), p.1-12.

Yoshihara, S., Nishimura, H., Yamamoto, H., & Manabe, K. I. 2003. Formability enhancement in magnesium alloy stamping using a local heating and cooling technique: circular cup deep drawing process. *Journal of Materials Processing Technology*, 142(3), p.609-613.

Zener C., and Hollomon J.H. 1944. Effect of strain rate upon plastic flow of steel, *Journal of Applied physics* 15, no. 1, p. 22-32.

Zhang, X.M., Zeng, W. D., Ying, S., Zhou, Y. G., Zhao, Y. Q., Huan, W. U., & Yu, H. Q. 2009. Fracture criterion for predicting surface cracking of Ti40 alloy in hot forming processes. *Transactions of Nonferrous Metals Society of China*, 19(2), p.267-271.

CHAPTER 2: Developing a Zener-Hollomon based Forming Limit Surface for Warm Forming of Magnesium Sheet Material

2.1 Introduction

As the lightest structural metal, magnesium alloys are attractive candidates for lightweighting automotive components (Mallick 2010). However, magnesium alloys have poor formability at room temperature, which is attributed to the fact that basal slip and twinning of the HCP crystal structure of magnesium are the only two active deformation mechanisms at room temperature. At elevated temperatures, the formability of magnesium alloys is improved substantially due to the activation of additional slip systems, e.g. $\langle c+a \rangle$ slip, and thermally activated dynamic recrystallization (Agnew and Özgür 2005). This is the reason for developing warm forming processes for manufacturing magnesium alloy parts (Neugebauer et al. 2006). Among the wrought magnesium alloys, AZ31 is the most frequently considered sheet material for automotive applications. Considerable increase in the formability of the AZ31 alloy was observed at temperatures ranging from 200 to 350°C in warm forming of conical cups by (Chen and Huang 2003), circular cups by (Doege and Dröder 2001, Zhang et al. 2006, Yoshihara et al. 2003) and square cups by (Cheng et al. 2003). With improved formability, vehicle decklid inner panels formed from AZ31 sheet alloy using hot gas pressure forming process at 450°C have been reported by Carter et al. (Charter et al. 2011).

Finite element method based forming simulations are widely used to design and optimize sheet metal forming processes (Sheng et al. 2004). Fracture and necking failure in sheet metal forming are usually predicted using strain-based Forming Limit Curves (FLCs), in which major local strains at the initiation of localized necking and fracture are plotted against minor local strains (Banabic 2010). Although it is sensitive to the strain path, the convenience of its implementation and lack of a better criterion has made the use of FLC a widely accepted method in both academia and industry for the identification of localized necking and fracture in sheet metal forming (Stoughton 2000, Bruschi et al. 2014).

In various studies on formability of magnesium alloys in warm forming conditions, it is observed that the levels of FLCs increase with increasing temperature, but decrease with increasing strain rate (Chen and Huang 2003, Zhang et al. 2006, Lee et al. 2007, Bruni et al. 2010, Abu-Farha et al. 2012, Hsu et al. 2008). Due to variation in tooling speed and heat transfer between the sheet and the tool, warm forming is, in general a non-isothermal process, which creates spatially and temporally different distribution of strain rates and temperatures on the sheet during the forming operation (Doege and Dröder 2001, Zhang et al. 2006, Yoshihara et al. 2003, Chen et al. 2003). Thus, prediction of fracture in warm forming requires a complete representation of forming limits that vary with strain rates and temperatures. Three-dimensional forming limit diagrams with either temperature or strain rate as the third axis have been proposed (Abu-Farha 2011, Kröhn et al. 2007). A three-dimensional forming limit surface that takes into account both temperature and strain rate was proposed in (Sheng 2012). In this concept, the Zener-Hollomon parameter (Z), or the so-called temperature-compensated strain rate (Zener and Hollomon 1944), is used to represent the effects of strain rate and temperature on the forming limit and forms the third

axis in the Forming Limit Surface diagram. The three-dimensional FLS, which is termed Z-FLS in the current paper, was based on the observation that the major limit strains on the forming limit curves of aluminum alloy 5083-O sheet at different strain rates and temperatures can be described as a function of $\ln(Z)$. In the current study, the concept of Z-FLS is revisited. A Z-FLS is constructed for AZ31B sheet material using available forming limit curves and then used to identify failure by fracture using FEM simulations of a non-isothermal round cup drawing process.

2.2 Zener-Hollomon Based Forming Limit Surface (Z-FLS)

The Zener-Hollomon based forming limit surface (Z-FLS) is a three dimensional representation of forming limits of sheet materials that can be expressed in the following equation form.

$$F(\varepsilon_1, \varepsilon_2, \ln(Z)) = 0 \quad (2.1)$$

In this equation, ε_1 and ε_2 are the major and minor local strains, and Z represents the Zener-Hollomon parameter (Zener and Hollomon 1944) given by Equation (2.2).

$$Z = \dot{\varepsilon} e^{Q/RT} \quad (2.2)$$

where, $\dot{\varepsilon}$ is the strain rate, Q is the activation energy, R is the gas constant and T is the sheet temperature in K.

The dependency of the effective strain at fracture on $\ln(Z)$ was reported in hot tensile/torsion tests on bulk aluminum alloys (Alexandrov et al. 2005) and warm forming of magnesium sheet material (Kim and Kim 2010). Alexandrov et al. (2005) used a polynomial function of the form to represent the effective limit strain:

$$\bar{\varepsilon}^{fl} = A(\ln Z)^2 + B(\ln Z) + C \quad (2.3)$$

where, A , B and C are material parameters that are determined by regression analysis of effective limit strains from tensile tests at a few selected temperatures and strain rates.

The warm forming of magnesium alloy sheet material is normally conducted at temperatures ranging from 200 to 350°C and strain rate ranging from 0.001 to 1s⁻¹ (Chen and Huang 2003, Doege and Dröder 2001, Zhang et al. 2006, Yoshihara et al. 2003, Chen et al. 2003). Based on the observation on several groups of FLCs at different temperatures and strain rates, Sheng (2012) proposed that a polynomial relationship, similar to Equation (3) can be used for the limit major strain on the FLCs of AA 5083 sheet at elevated temperatures. At different minor strains, the major limit strain ε_1^* is expressed as:

$$\varepsilon_1^* = A(\varepsilon_2)(\ln Z)^2 + B(\varepsilon_2)(\ln Z) + C(\varepsilon_2) \quad (2.4)$$

where, A , B and C are assumed to be functions of the minor strain ε_2 . They are determined by fitting Equation (4.4) to experimentally determined FLCs at a few selected temperatures and strain rates. Using control curves at each minor strain defined by Equation (2.4) and linearly interpolating values between them, a 3D Forming Limit Surface or Z-FLS can then be constructed (Sheng 2012).

When working with a finite element forming simulation model to predict forming limit, the risk of fracture can be determined by considering the difference of the major limit strain ε_1^* on the surface of the Z-FLS diagram and the calculated major strains ε_1 in various elements on the model. In equation form, the difference is given by

$$\Delta\varepsilon_1 = \varepsilon_1 - \varepsilon_1^* \quad (2.5)$$

If $\Delta\varepsilon_1$ is higher than or equal to zero, fracture will occur. Given a safe margin of 0.05, if $\Delta\varepsilon_1$ is between 0 and -0.05, the element is considered to be in a risk of fracture; otherwise, the element is considered safe.

2.3 Construction of Z-FLS for AZ31 Magnesium Alloy

Forming Limit Curves (FLCs) reported in the literature at four different temperatures and two different strain rates were used to construct the Z-FLS for an AZ 31 magnesium alloy. Three forming limit curves, shown in Figure 2.1a, were generated using Nakajima dome test data on 1.2 mm thick rectangular specimens of AZ31 sheet under isothermal temperature conditions of 100, 200 and 300°C and a constant punch speed of 0.1 mm/s (Chen and Huang 2003). In constant speed mechanical stretching tests (Albakri et al. 2013), such as the Nakajima dome test, the strain rate increases with punch travel and its value depends on the punch speed. Albakri et al. (2013) have shown that under balanced biaxial test condition in a Nakajima dome test, the strain rate in AZ31B sheets reached 0.008 s^{-1} at a punch speed of 0.1 mm/s and punch displacement of 32 mm. Since the strain rate value was not given in (Chen and Huang 2003), it is assumed that the strain rate in Figure 1a is approximately 0.008 s^{-1} .

The strategy of strain rate determination confirms to the method used by Naka et al. (Naka et al. 2001), which used the strain rate close to the failure in their tests on determining FLCs. The fourth forming limit curve, shown in Figure 2.1b, was developed using pneumatic stretching tests on 0.98 mm thick rectangular specimens of AZ31B sheet at 400°C and a constant strain rate of 0.005 s^{-1} (Abu-Farha et al. 2012). It is to be noted that the sheet thickness in the second set of FLC is different than that in the first set. Antoniswamy et al (Antoniswamy et al. 2013) have shown that initial sheet thickness did

not affect the limit strain based on their tests on AZ31B sheet material at two different thicknesses (1.28 mm and 2.0 mm) at a temperature of 350°C and different strain rates.

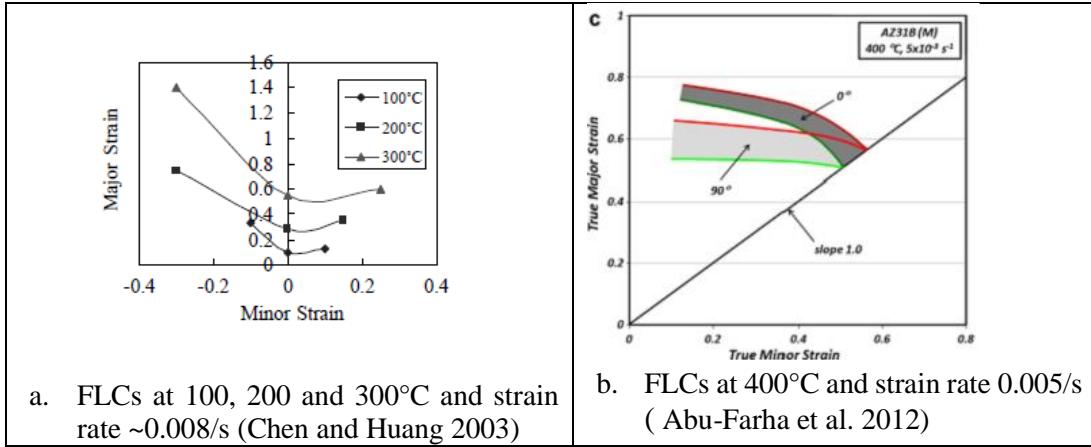


Figure 2.1 Forming limit curves (FLCs) of AZ31B as reported in References (Chen and Huang 2003) and (Abu-Farha et al. 2012) used for constructing Z-FLS shown in Figure 2.3

Since strains in sheet forming range from -2 to 1 and $\ln(Z)$ is a much larger number, a normalized value of $\ln(Z)$ was used to make it compatible with the strain values. The normalized value, represented by $\overline{\ln(Z)}$, is calculated using the following equation.

$$\overline{\ln(Z)} = \frac{\ln(Z)}{\ln(Z_0)} \quad (2.6)$$

where, $\ln(Z_0)$ is the value of $\ln(Z)$ at the lowest strain rate and the highest temperature in the selected warm forming experiments. Accordingly, $\ln(Z)$ is replaced with $\overline{\ln(Z)}$ in Eq.(2.4) so that the major limit strain becomes

$$\varepsilon_1^* = A(\varepsilon_2) \overline{\ln(Z)}^2 + B(\varepsilon_2) \overline{\ln(Z)} + C \quad (2.7)$$

Table 2.1 lists the major limit strain values corresponding to minor strains ranging from -0.3 to 0.25. The major limit strain values in white boxes were obtained from Figure 4.1.

Table 2.1 Major limit strains at different minor limit strains, temperature and strain rates*

| $\dot{\epsilon}_1$ (s ⁻¹) | T(°C) | ln(Z) | $\overline{\ln(Z)}$ | Major Limit Strain (ϵ_1^f) at | | | | | |
|---------------------------------------|-------|-------|---------------------|--|-------|------|------|-------|-------|
| | | | | Minor Strain (ϵ_2) | | | | | |
| | | | | -0.3 | -0.1 | 0 | 0.1 | 0.175 | 0.25 |
| 0.005 | 400 | 18.83 | 1.0 | 1.68 | 1.10 | 0.62 | 0.62 | 0.61 | 0.6 |
| 0.008 | 300 | 23.51 | 1.138 | 1.4 | 0.8 | 0.5 | 0.53 | 0.54 | 0.56 |
| 0.01 | 300 | 23.73 | 1.260 | 0.767 | 0.657 | 0.4 | 0.44 | 0.47 | 0.527 |
| 0.008 | 200 | 29.50 | 1.456 | 0.72 | 0.45 | 0.28 | 0.32 | 0.38 | |
| 0.008 | 100 | 38.70 | 1.945 | 0.259 | 0.2 | 0.1 | 0.15 | 0.228 | |
| 0.01 | 50 | 45.67 | 2.425 | 0.0948 | 0.087 | 0.04 | 0.07 | 0.138 | |

*: The experimental data in white boxes were obtained from published FLCs in (Chen and Huang 2003, Abu-Farha et al. 2012)

The values of A, B and C as a function of minor strain were determined using regression analysis of the data given in Table 2.1 and are plotted in Figure 2.2. Using Equation (2.7), major limit strains corresponding to several other minor strains and ln (Z) were then calculated. These values are in the blue boxes in Table 2.1. All of the strain values listed in Table 2.1 were used in constructing the Z-FLS diagram shown in Figure 2.3.

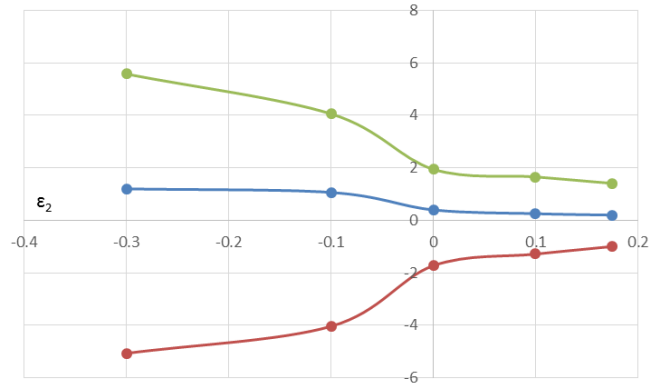


Figure 2.2 Plots of material constants A, B, C under different minor strains

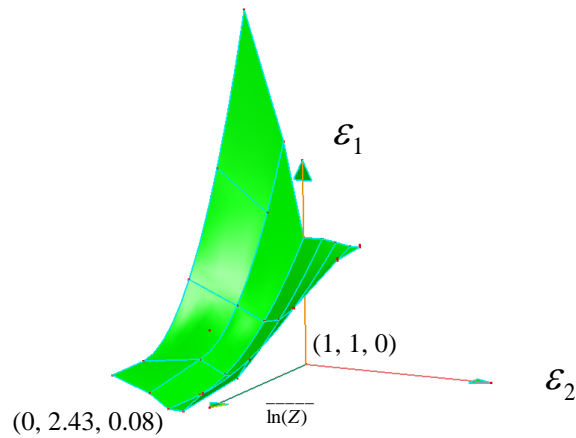


Figure 2.3 Z-FLS for AZ31B magnesium alloy

As shown in Table 2.1, among the four FLCs selected, the lowest $\ln(Z)$ is at 400°C and strain rate of 0.005 s⁻¹, which was calculated using R as 8.31 J mol⁻¹ K⁻¹ and an average activation energy Q of 135 kJ mol⁻¹ (Sheng and Shivpuri 2006¹). Its value is 18.83, which was used as $\ln(Z_0)$ for normalizing $\ln(Z)$. The upper limit of $\overline{\ln(Z)}$ on the Z-FLS diagram corresponds to a combination of 50°C temperature and 0.01 s⁻¹ strain rate. Its values is 2.425, which corresponds to a $\ln(Z)$ value of 45.67. The selection of this upper limit is based on an assumption that the strain rate effect is trivial at room temperature.

The use of Eq. (2.7) to construct of Z-FLS was validated by determining FLCs from Figure 2.3 and comparing them with the experimental FLCs reported by Bruni et al. (2010) and Hsu et al. (2008). The experiments were conducted at 300°C and two different strain rates, namely 0.001 s^{-1} and 0.01 s^{-1} . The corresponding $\overline{\ln(Z)}$ are 1.138 and 1.26 as shown in Figure 4. The forming limit curves determined using Z-FLS and shown by the solid lines match well with the distribution of experimental data (Bruni et al. 2010) and (Hsu et al. 2008).

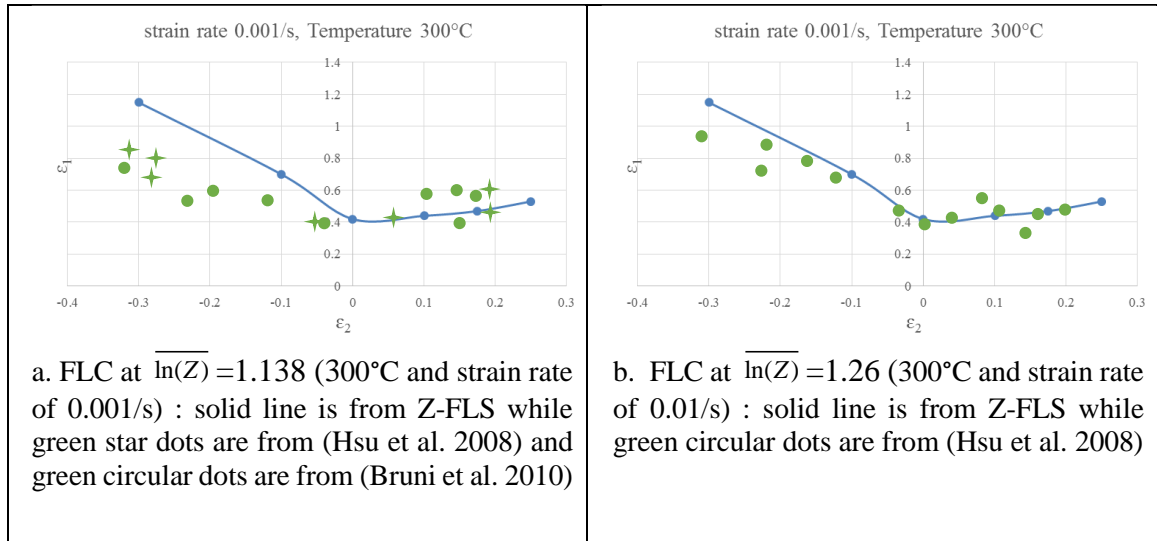


Figure 2.4 FLCs constructed using the Z-FLS in Figure 2.3 and compared with data reported in References ((Bruni et al. 2010) and (Hsu et al. 2008))

2.4 Fracture Prediction Using Z-FLS

The Z-FLS constructed in Figure 2.3 is now used to predict fracture in an AZ31 sheet material during a non-isothermal round cup drawing process conducted by Dröder (1999) and investigated numerically by Palaniswamy et al. (2004). In the experiments, Dröder determined the limiting draw ratio (LDR) of AZ31B at blank holder/die temperatures ranging from 150 to 300°C and an initial punch temperature of 25°C. The punch diameter and initial sheet thickness were 100 mm and 1.3 mm, respectively. At 5

mm/s punch speed and blank holder/die temperature of 200°C, the maximum LDR was 2.52. In the test, the sheet blank was initially heated to a uniform temperature that is equivalent of blank holder/die temperature. During drawing, the cup bottom lost heat to cold punch while the flange area stayed at a high level due to the heating effect of blank holder/die. In order to predict failure, a thermo-mechanically coupled finite element simulation of the cup drawing process was conducted using the implicit and explicit codes of LS-DYNA. The plastic strains, thickness distribution in the sheet and punch load were calculated using the explicit dynamic algorithm, while the temperature distribution was calculated using the implicit algorithm.

2.4.1 Flow stress modeling

The flow stress at different temperatures and strain rates are expressed by a set of baseline flow stress curves while the strain rate effect is calculated by the Cowper-Symonds equation (Tari and Worswick 2015):

$$\sigma = \sigma_0 \left[1 + \left(\frac{\dot{\epsilon}_{eff}^P}{C} \right)^{1/P} \right] \quad (2.8)$$

where, σ_0 is the baseline flow stress and $\dot{\epsilon}_{eff}^P$ is the effective plastic strain rate. C and P are temperature-dependent material parameters and are determined by minimizing the difference between the calculated flow stress and the flow stress at the target high strain rate.

In order to determine C and P in Eq. (2.8), flow stress curves are needed at several temperatures and strain rates that are representative of the warm cup forming process being analyzed. Before localized necking, the strain rate in the cup wall during the cup drawing process with a punch speed of 5 mm/s is estimated to be in a range from 0.01 s⁻¹ to 0.1 s⁻¹.

Thus, flow stress curves at temperatures ranging from 25°C to 300°C at strain rate of 0.01 s⁻¹ were chosen for baseline while those at strain rate of 0.1 s⁻¹ were chosen as target for determining C and P in Equation (2.8). The baseline flow stress curves and target flow stress curves were generated using the flow stress model (Sheng and Shivpuri 2006¹) given by Eq. (2.9) and the tensile test data from Reference (Dröder 1999, Palaniswamy et al. 2004). Based on this model, the strain rate and temperature effect on flow stress is expressed in terms of $\log(Z/2)$ as:

$$\sigma = K(\log(Z/2))\bar{\epsilon}^{n(\log(Z/2))} \quad (2.9)$$

From the tensile stress-strain diagrams shown in Figure 5a and 5b, K and n in Eq. (2.9) were determined by regression as:

$$K = 3.105\log^2(Z/2) - 52.109\log(Z/2) + 379.24 \text{ MPa}$$

$$n = -0.0004\log^2(Z/2) + 0.0222\log(Z/2) - 0.1068$$

Based on Eq. (2.9), two sets of target flow stress curves at temperatures ranging from 25°C to 300°C were generated as shown in Figures 2.5c and 2.5d. Then C and P at different temperatures were generated by minimizing the difference between the target flow stress and the flow stress obtained from Eq. (2.8). Table 2.2 gives the C and P values obtained by the process described above.

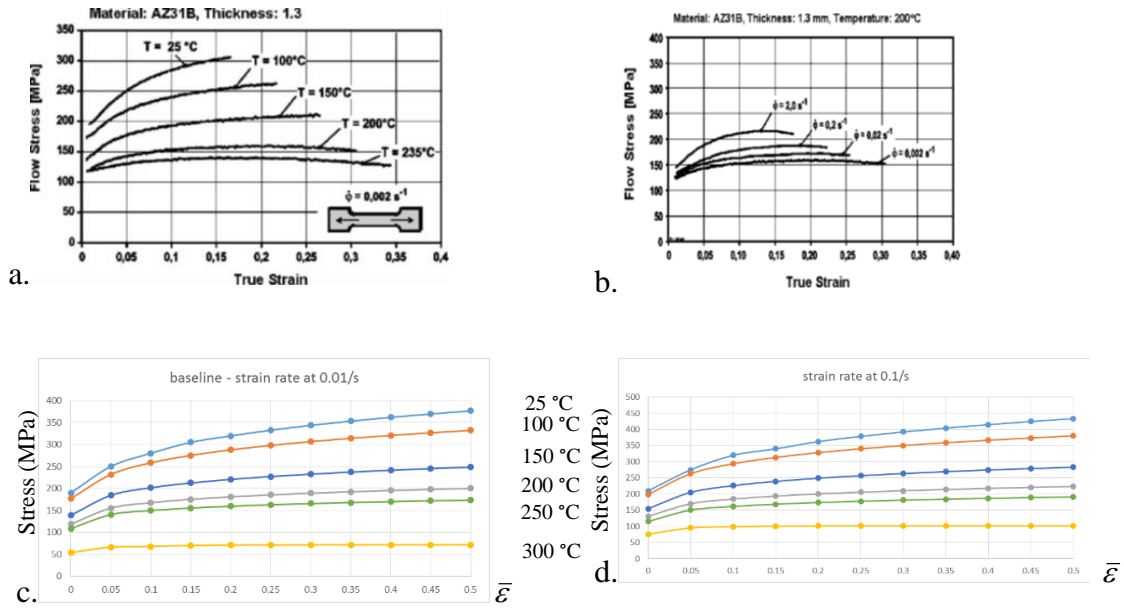


Figure 2.5 Flow stress curves: a) at temperatures from 25 to 235°C and strain rate of 0.002/s, b) at temperature 200°C and strain rates from 0.002 to 2.0/s (Dröder 1999, Palaniswamy et al. 2004), c) calculated at strain rate of 0.01/s using Eq. (2.9)

Table 2.2 Material parameters C and P in the Cowper and Symonds equation

| | Temperature (°C) | | | | | |
|----------|------------------|-----|-----|-----|------|-----|
| | 25 | 100 | 150 | 200 | 250 | 300 |
| <i>C</i> | 4e5 | 462 | 10 | 11 | 14.5 | 15 |
| <i>P</i> | 1.9 | 2.3 | 2.2 | 2.1 | 2.2 | 4.2 |

2.4.2 FEM modeling of round cup forming

Figure 2.6 shows the FEM model for the round cup draw. Table 2.3 lists the processing conditions and Table 2.4 lists the material properties used in the simulation. The blank holder pressures varies at different setups to be at a minimum level to prevent wrinkling. Due to the axisymmetric nature of the problem and based on isotropic yielding assumption in warm forming conditions, only a quarter of the geometry was modeled. The isotropic assumption is supported by the observation made by Agnew and Duygulu (2005) that the anisotropy of AZ31 sheet material is reduced significantly at elevated temperatures.

The tooling components were modeled as rigid, while the sheet blank was modeled as an elastic-viscoplastic material with thermal effects. Material model 106 (MAT 106) in LS-DYNA, which uses von-Mises criteria for yielding, was used to describe the elastic-viscoplastic behavior of the sheet material. The punch was modeled using tetrahedron solid elements with 10 nodes and an average mesh size of 3 mm and had 8 elements distributed over punch radius to calculate the heat transfer between punch and blank. Since the blank holder and the die temperatures are higher than the punch and blank temperatures, they function as heat source and were modeled by shell elements with an average mesh size of 2.5 mm, which ensured nine elements distributed over the die radius. The sheet blank was meshed with mixed quad and triangular shell elements with an average size of 2 mm. The quad elements were uniformly distributed from the edge of the blank to the start of the bottom flat surface of the punch to avoid high stiffness introduced by the triangular elements. The die displacement was constrained while the punch and the blank holder were allowed to move only in the vertical direction.

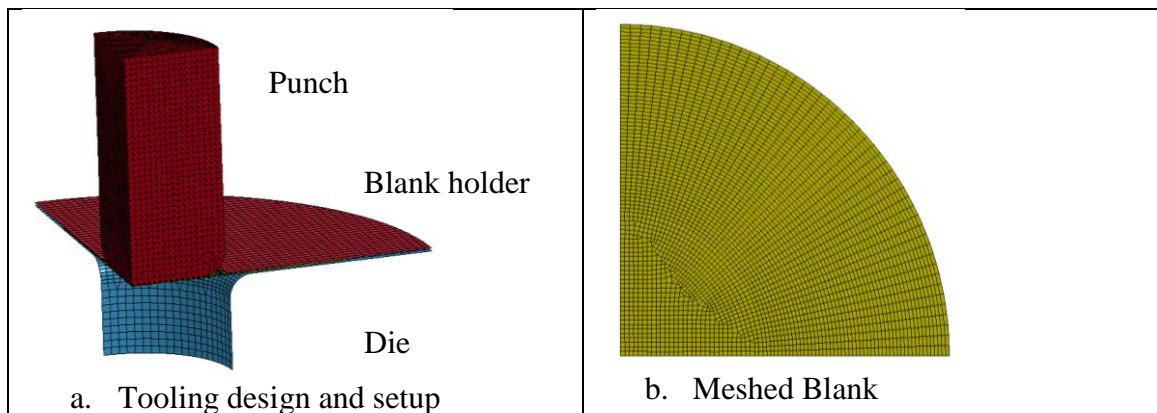


Figure 2.6 Finite element model of round cup draw

Table 2.3 Boundary conditions and material properties used in the simulation of round cup drawing (Doege and Dröder 2001, Palaniswamy et al. 2004)

| | |
|-------------------------------------|------------------------|
| Tooling setup | |
| Punch diameter (mm) | 100 |
| Punch and die corner radii (mm) | 12 |
| Punch speed (mm/s) | 5 |
| Blank thickness (mm) | 1.3 |
| Flow stress curves | Figure 2.5 (c) and (d) |
| Interfacial coefficient of friction | 0.1 ~0.4 |
| Thermal properties | Given in Table 4 |
| Blank holder pressure | 0.5 ~ 2.0 MPa |

Table 2.4 Thermal properties of AZ31 sheet material and tool material (Palaniswamy et al. 2004)

| | |
|--|--------|
| Thermal conductivity of the sheet material (N/s °C) | 159 |
| Heat capacity of the sheet material (N/mm ² °C) | 1.7675 |
| Thermal conductivity of the tool material (N/s °C) | 60.5 |
| Heat capacity the tool material (N/mm ² °C) | 3.41 |
| Interface contact heat conductance (N/s mm °C) | 4.5 |
| Factor to convert plastic deformation energy to heat | 0.95 |

The Coulomb friction coefficient at the interfaces between the tooling components and the sheet material was assumed as 0.1 at 25-100°C, 0.2 at 200 and 250°C and 0.4 at 300°C. The selection of relatively high values of friction coefficients at higher temperatures is based on friction study on magnesium alloys at different lubrication conditions at elevated temperatures (250 to 450°C) (Sivapragash et al. 2008, Verma et al. 2009, Gontarz et al. 2011), local increase of friction coefficient at elevated temperature due to the possible failure of lubricant and friction coefficient selection strategy discussed in (Kim et al. 2006).

2.4.3 Results and Analysis

In this study, cup drawing at four different temperatures of sheet blank/die/blank holder, namely 150, 200, 250 and 300°C were simulated. The initial punch temperature was assumed to be 25°C. The finite element models were first validated by comparing the calculated temperature distribution, punch load, and thickness distribution on the formed

cups with the experimental measurements. Then, the Z-FLS in Figure 2.3 was used to predict fracture and determine the LDR of the numerically formed cups.

(1) Temperature distribution

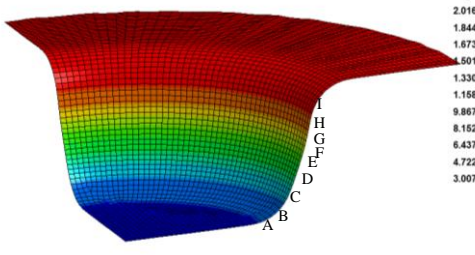
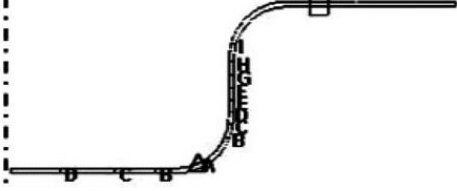
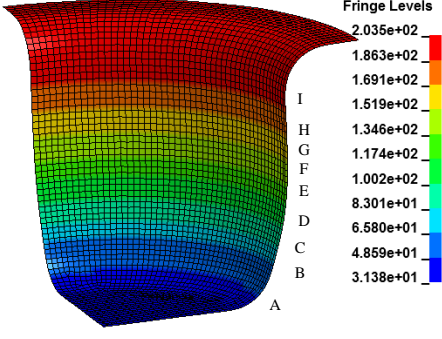
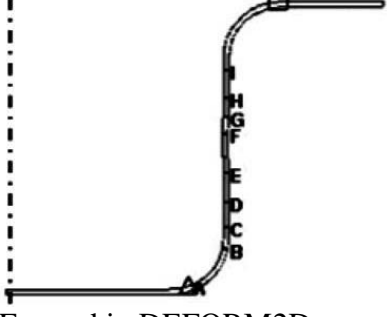
During simulations, blank holder and die temperatures were maintained at the initial temperature, which caused the flange area to remain at a higher temperature than the rest of the cup. As the sheet blank was drawn into a cup, the cup wall was cooled due to heat loss to the cold punch. The temperature distribution on the cup wall is given in Table 2.5. The difference between the predicted values in this study and the reported values in (Palaniswamy et al. 2004) is small ($< 3\text{ }^{\circ}\text{C}$).

(2) Punch loads

Punch loads predicted by finite element simulations are compared with the measured values in Figure 2.7. The cups drawn at 150 and 200°C do not exhibit any fracture, while the cups drawn at 300°C fractures at 33 mm punch displacement. The punch loads reach the peak values at about 40 mm stroke at 150 and 200°C, then decrease due to a reduction of restraining force from the workpiece with reduced flange area clamped between the blank holder and the die. At 300°C, the peak load is reached at a stroke of about 25 mm and stays at this level till the stroke reaches 33 mm, then drops due to the fracture of the cup wall. These trajectories are similar in trend to the punch load trajectories obtained in round cup draw (Dröder 1999, Palaniswamy et al. 2004). At 150°C, the predicted punch load is very close to the experimental value; however, at 200 and 300°C, the predicted punch loads are higher at larger punch travels and the peak punch load is higher compared with the experimental values. The possible reasons are: 1) the stress-strain curves were extrapolated after the peak stress in the tensile test data and did not consider

the softening stage and 2) the elements were not deleted when the fracture criterion was met in the case of 300°C.

Table 2.5 Predicted temperature distribution on the cup being drawn at 200°C

| Time = 6 s, stroke = 30 mm | | | | |
|--|--------------------------------|---|--------------------------------|--|
|  <p>Formed in LS-DYNA 3D</p> | |  <p>Formed in DEFORM2D</p> | | |
| <p>Fringe Levels</p> <ul style="list-style-type: none"> 2.016e+02 1.844e+02 1.673e+02 1.501e+02 1.330e+02 1.158e+02 9.867e+01 8.152e+01 6.437e+01 4.722e+01 3.007e+01 | | <p>Obj 2 (x10E2)</p> <ul style="list-style-type: none"> A = 0.6136 B = 0.7718 C = 0.9299 D = 1.0880 E = 1.2462 F = 1.4043 G = 1.5624 H = 1.7205 I = 1.8787 J = 2.0368 | | |
| Time = 14 s, stroke = 70 mm | | | | |
|  <p>Formed in LS-DYNA 3D</p> | |  <p>Formed in DEFORM2D</p> | | |
| <p>Fringe Levels</p> <ul style="list-style-type: none"> 2.035e+02 1.863e+02 1.691e+02 1.519e+02 1.346e+02 1.174e+02 1.002e+02 8.301e+01 6.580e+01 4.859e+01 3.138e+01 | | <p>Obj 2 (x10E2)</p> <ul style="list-style-type: none"> A = 0.5006 B = 0.6714 C = 0.8422 D = 1.0131 E = 1.1839 F = 1.3547 G = 1.5256 H = 1.6964 I = 1.8672 J = 2.0380 | | |
| | @30mm stroke | | @70mm stroke | |
| Measurement points | Temperature in LS-DYNA 3D (°C) | Temperature in DEFORM 2D (°C) (Ref 25) | Temperature in LS-DYNA 3D (°C) | Temperature in [] by DEFORM 2D (°C) (Ref 25) |
| A | 58.3 | 61.3 | 47.5 | 50.1 |
| B | 75 | 77.2 | 64.3 | 67.1 |
| C | 92 | 92.99 | 84.3 | 84.2 |
| D | 107.6 | 108.9 | 102.1 | 101.3 |
| E | 123.8 | 124.6 | 112.5 | 110.4 |
| F | 147.1 | 148.4 | 136.2 | 134.5 |
| G | 154.7 | 156.2 | 154.4 | 152.6 |
| H | 169.7 | 172.1 | 167.5 | 169.6 |
| I | 186.8 | 187.9 | 187.9 | 186.7 |
| J | 201.6 | 203.7 | 203.5 | 203.8 |

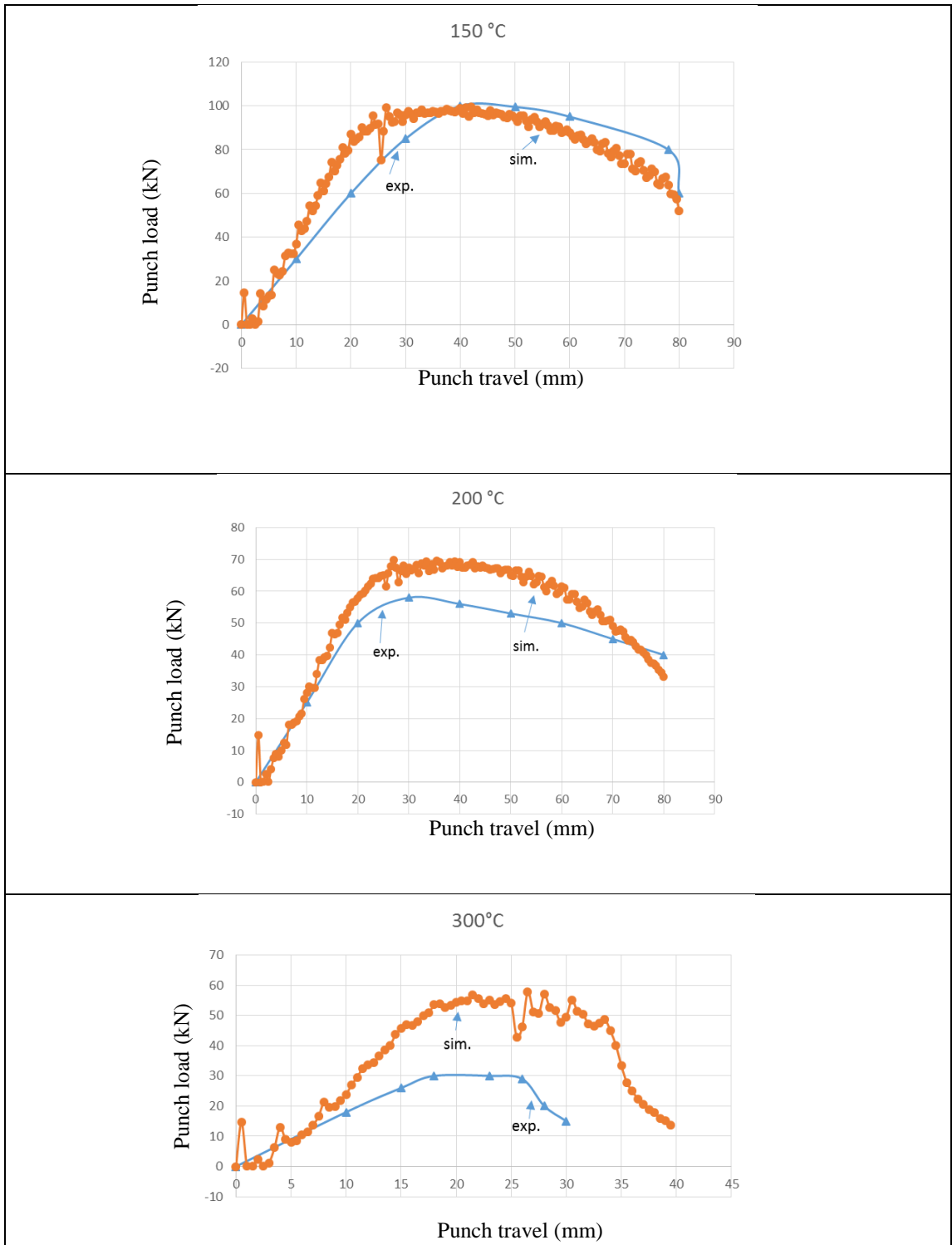


Figure 2.7 Predicted punch load curves at different temperatures for draw ratio of 2.3 compared with experimental data in (Dröder 1999, Palaniswamy et al. 2004)

(3) Thickness distribution

Figure 2.8 shows a comparison of the predicted thinning of the cup wall with experimental measurements at 200 and 250°C at a draw ratio (DR) of 2.3 (Dröder 1999, Palaniswamy et al. 2004). The patterns of thinning distribution match with the experimental data. The maximum thinning increases with increase in temperature. Compared with the measurement, the predicted maximum thinning is 3~5% lower while the maximum thickening at the flange is about 8~11% lower in both cases. One possible reason for the difference is our assumption of constant coefficient of friction at each temperature investigated.

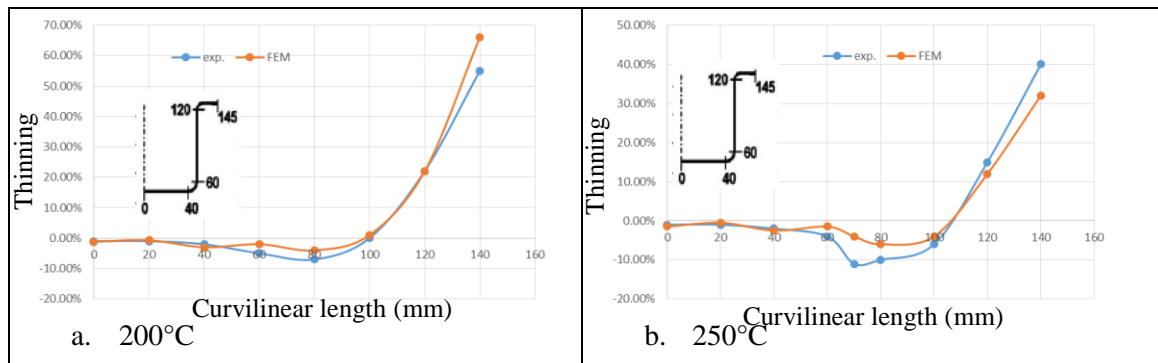
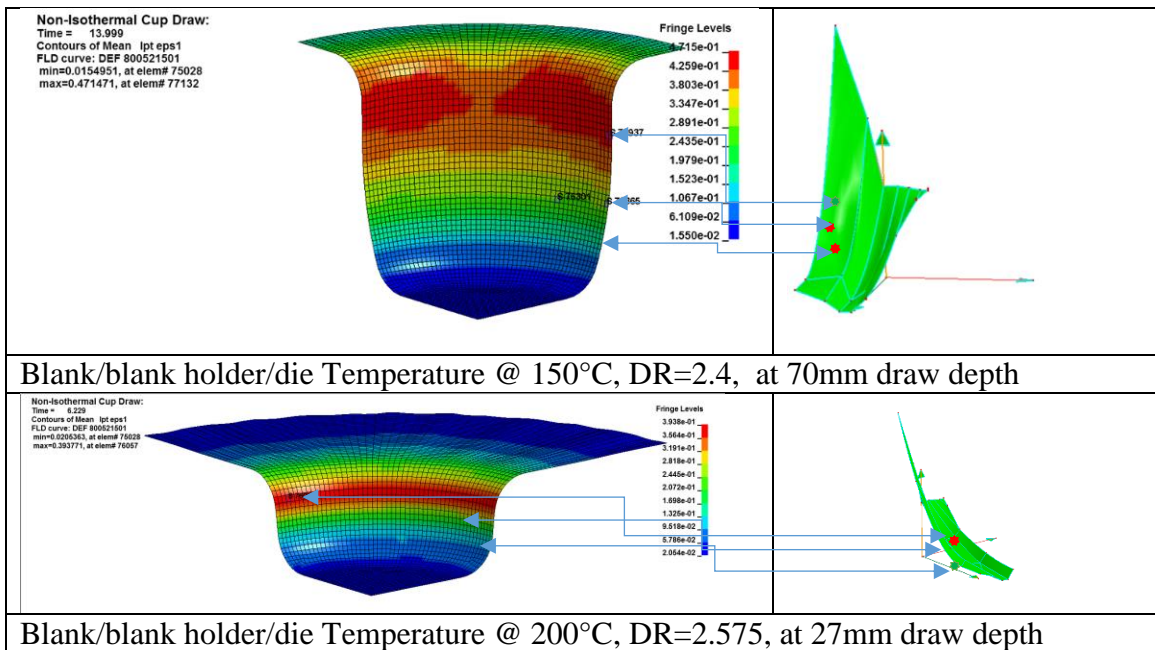


Figure 2.8 Comparison of simulated values of thinning (% change in thickness) at a draw ratio of 2.3 with experimental data in (Dröder 1999, Palaniswamy et al. 2004)

(4) Fracture and Limiting Draw Ratio (LDR)

The constructed Z-FLS in Figure 2.3 was used to predict fracture and its location on the numerically formed cup. The maximum blank diameter (D_o) that can be drawn in the die without fracture was used to calculate the LDR, which is a ratio of D_o and punch diameter D_p . The fracture of numerically formed cups was identified by plotting the data points (ϵ_1 , ϵ_2 and $\overline{\ln(Z)}$) of concerned elements against the Z-FLS, see Figure 2.9. The data

points of three elements representing maximum thinning, maximum major strain and no risk of fracture are plotted at the initiation of fracture, see Table 2.6. In all cases, the elements with the maximum major strain and maximum thinning fracture at the same depth of draw. At 250°C, the thinnest element also develops the highest major strain. Fracture location shifts from location close to punch corner at 150°C to the upper portion of cup wall at 200, 250 and 300°C, which conforms to the observation in (Palaniswamy et al. 2004). This can be explained by increased strength difference between sheet material at the die curvature area and that at the punch radius area, which is strengthened by the cold punch. The identified depths of cup at the initiation of fracture are close to the observations in the experiment (Palaniswamy et al. 2004). For example, at 300°C and DR = 2.3, the calculated depth is 33 mm while 32 mm is the measured depth, and at 250°C and DR = 2.4, the calculated depth is 28.5 mm while 30 mm is the depth reported in the experiment.



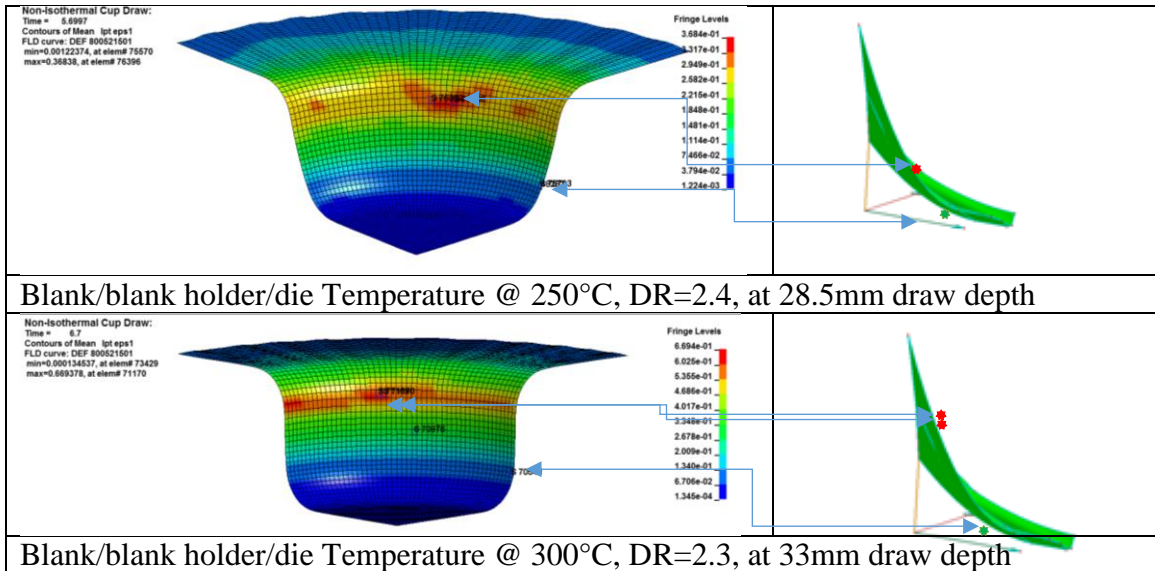


Figure 2.9 Fracture identification in drawn cups with the aid of the Z-FLS in Figure 2.3

Table 2.6 Failure status of representative elements in non-isothermal cup draw test

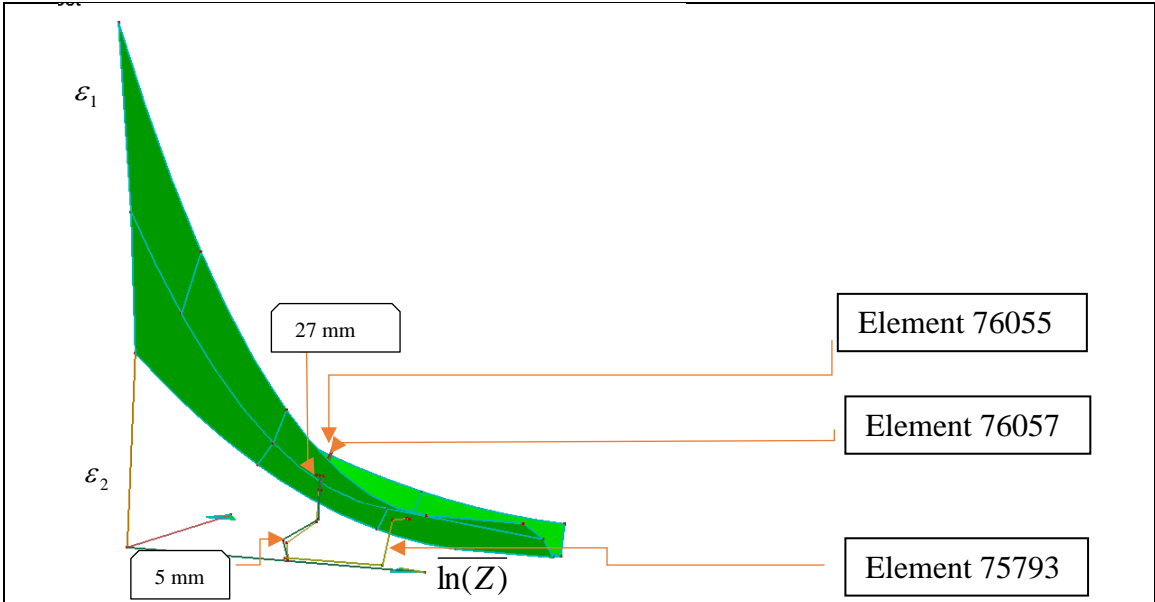
| Die/Blank Holder T (°C) | Status | Element | ϵ_2^* | ϵ_1^* | ϵ_1^* | T | $\ln(Z)$ | $\Delta\epsilon_1^*$ | Thinning (%) |
|-------------------------|----------|---------|----------------|----------------|----------------|-----|----------|----------------------|--------------|
| 150 | Fracture | 76365 | -0.230 | 0.3 | 0.09 | 89 | 2.254 | 0.002 | 6.8 |
| | Fracture | 76301* | -0.210 | 0.284 | 0.092 | 85 | 2.282 | 0.004 | 7.1 |
| | Safe | 76937 | -0.400 | 0.40 | 0.004 | 130 | 1.847 | -0.055 | 3.9 |
| 200 | Fracture | 76057* | -0.15 | 0.31 | 0.07 | 199 | 1.70 | 0.015 | 15.6 |
| | Fracture | 76055 | -0.13 | 0.3 | 0.06 | 199 | 1.68 | 0.01 | 15.2 |
| | Safe | 75793 | -0.06 | 0.13 | 0.02 | 121 | 1.981 | -0.068 | 6.3 |
| 250 | Fracture | 76369* | -0.215 | 0.422 | 0.5 | 227 | 1.67 | 0.001 | 18.5 |
| | Safe | 76793 | -0.06 | 0.077 | 0.016 | 135 | 2.1 | -0.09 | 1.4 |
| 300 | Fracture | 71169* | -0.31 | 0.668 | 0.6 | 285 | 1.52 | 0.003 | 30.1 |
| | Fracture | 71170 | -0.334 | 0.67 | 0.6 | 280 | 1.54 | 0.01 | 28.5 |
| | Safe | 70548 | -0.074 | 0.095 | 0.013 | 112 | 2.01 | -0.055 | 1.9 |

* indicates the element has the maximum thinning

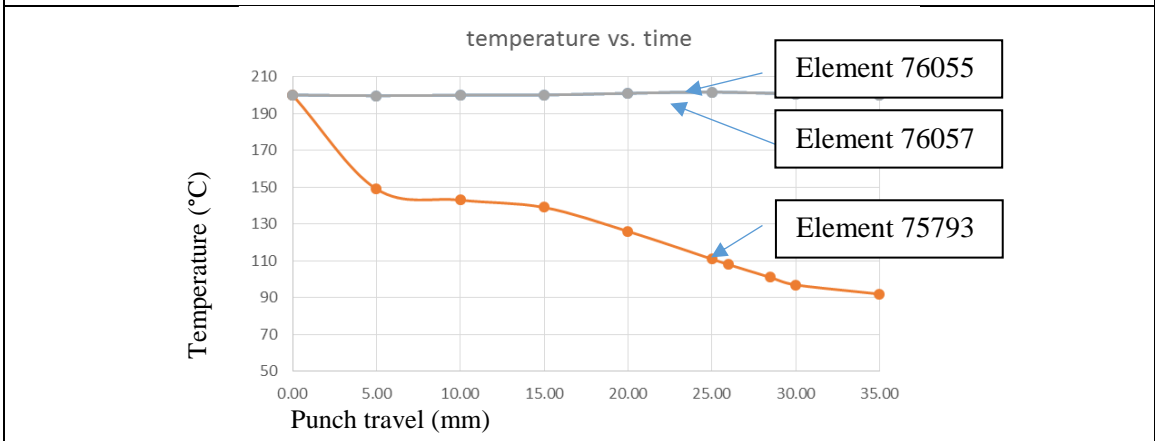
The evolution of the risk of fracture can be observed by plotting historical traces of the elements the Z-FLS diagram. Figure 2.10a gives a plot of three critical elements in the case of temperature 200°C. Element #76055 and element #76057 are at about same radial distance from the center of blank and thus are in contact with die and blank holder during most of the punch stroke. Because of this, their temperature remains approximately at 200°C as shown in Figure 2.10b. As a result, their major strain traces are close to each

other, which reaches the limit strain on the Z-FLS at strain rates of 0.06 s^{-1} and 0.07 s^{-1} , respectively, when the punch travel becomes equal to 27 mm as shown in Figure 10a. Element #76793, on the other hand, makes an early contact with the cold punch, which brings its temperature down at a faster rate (Figure 2.10b). The decrease in temperature leads to a faster increase in $\overline{\ln(Z)}$ which increases to about 2.03 at a punch travel of 27 mm, see Figure 2.10d. However, a decrease in temperature also strengthens the local material and major strain has a slower growth ($\dot{\epsilon}_1 \leq 0.02 \text{ s}^{-1}$) thereafter, as shown in Figure 2.10c. The slowly increasing major strain helps to keep the element #76793 safe under the Z-FLS.

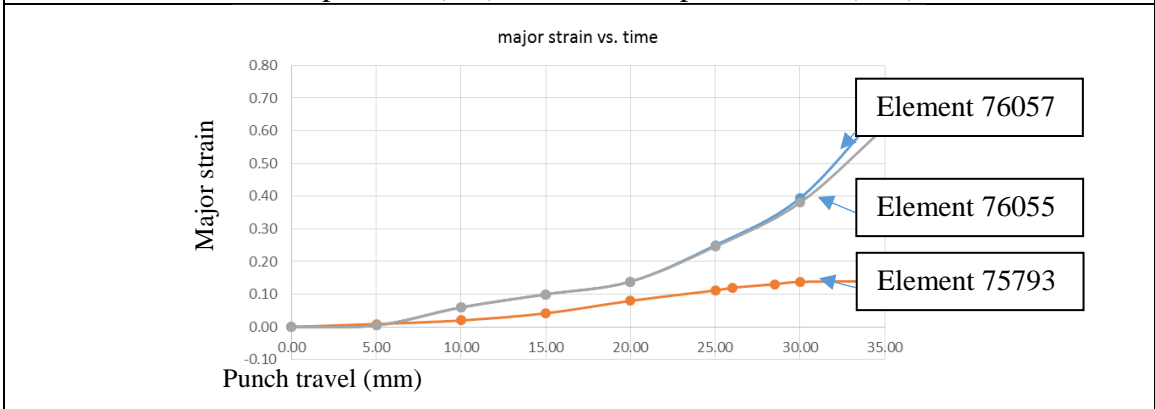
Figure 2.11 shows that the predicted LDRs at different temperatures match well with those obtained in the experiment. One exception is at temperature of 200°C , the prediction is higher by 0.03 (which is less than 0.15%) than the experimental value. One possible reason for the difference is that the strain rate effect varies with developing strain during plastic deformation (Sheng and Shivpuri 2006¹) while in the Cowper-Symonds equation used in this analysis, a constant strain rate effect was assumed during the entire deformation. Smaller increments of blank diameters used in the cup drawing experiments may have also contributed to the difference.



a. Data evolution in Z-FLS



b. Temperature ($^{\circ}\text{C}$) evolution vs. punch travel (mm)



c. Major strain evolution vs. time (s)

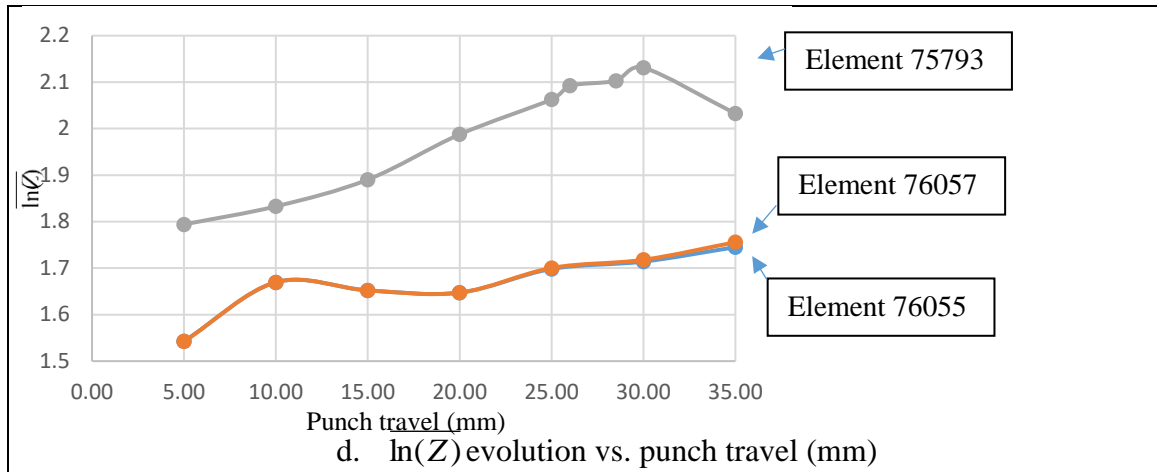


Figure 2.10 Historical data of elements on the Z-FLS (200°C, DR = 2.575)

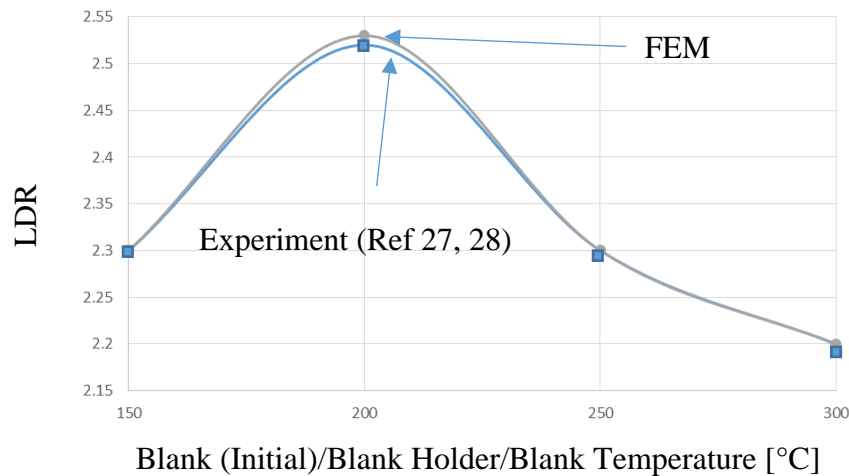


Figure 2.11 LDRs at different warm forming temperatures (punch diameter = 100 mm and blank thickness 1.3 mm)

2.5 Conclusions

In this study, the concept of forming limit surface (Z-FLS), which utilizes $\ln(Z)$ to represent the combined effect of strain rate and temperature on forming limit strains, is revisited and the process of constructing Z-FLS is demonstrated using the available experimental data on warm forming of AZ31 magnesium alloy. A non-isothermal cup drawing process of AZ31 sheet material was modeled using thermo-mechanically coupled finite element forming simulation. The Z-FLS was used to identify failure by fracture on the numerically formed cups. Results show that the depths at fracture and limiting draw

ratios match well with the experimental data. The results also indicate that the maximum thinning at fracture increases with decreasing $\ln(Z)$.

Since both strain rate and temperature effects are represented by a single parameter Z , the Z-FLS may provide a concise and convenient way to take them into account in predicting formability in warm and hot forming in which both strain rate and temperature change with increasing punch travel. Thus, its usefulness becomes evident in elevated temperature forming which involves non-isothermal transient conditions in which both temperature and strain rate change continuously with punch travel. The use of available experimental data from various sources may have introduced some error in the construction of Z-FLS in this paper, but the validity of Z-FLS has been demonstrated by using it to predict LDR in a cup drawing test and correlating it closely with experimental data. The maximum error was less than 0.15 percent. In practice, Z-FLS will be constructed using the tensile and forming limit data at a few carefully selected temperatures and strain rates. The Z-FLS can then be used for representing continuously distributed temperature/strain rate field in warm forming condition.

2.6 References:

Abu-Farha, F. 2011. The development of a forming limit surface for 5083 aluminum alloy sheet. *JOM* 63.11, p. 72-78.

Abu-Farha, F., Verma, R., & Hector, L. G. 2012. Hot Formability Curves for Four AZ31B Magnesium Alloy Sheets Obtained by the Pneumatic Stretching Test. *Magnesium Technology*, p.289-294.

Agnew, S. R., & Duygulu, Ö. 2005. Plastic anisotropy and the role of non-basal slip in magnesium alloy AZ31B. *International Journal of plasticity*, 21(6), p.1161-1193.

Albakri, M., Abu-Farha, F., & Khraisheh, M. 2013. A new combined experimental–numerical approach to evaluate formability of rate dependent materials. *International Journal of Mechanical Sciences*, 66, 5, p.5-66.

Alexandrov, S., Wang, P. T., & Roadman, R. E. 2005. A fracture criterion of aluminum alloys in hot metal forming. *Journal of materials processing technology*, 160(2), p.257-265.

Antoniswamy, A. R., Carpenter, A. J., Carter, J. T., Hector Jr, L. G., & Taleff, E. M. 2013. Forming-limit diagrams for magnesium AZ31B and ZEK100 alloy sheets at elevated temperatures. *Journal of materials engineering and performance*, 22(11), p.3389-3397.

Banabic, D. 2010. *Sheet metal forming processes: constitutive modelling and numerical simulation*. Springer Science & Business Media.

Bruni, C., Forcellese, A., Gabrielli, F., & Simoncini, M. 2010. Effect of temperature, strain rate and fibre orientation on the plastic flow behaviour and formability of AZ31 magnesium alloy. *Journal of Materials Processing Technology*, 210(10), p.1354-1363.

Bruschi, S., Altan, T., Banabic, D., Bariani, P. F., Brosius, A., Cao, J., & Tekkaya, A. E. 2014. Testing and modelling of material behaviour and formability in sheet metal forming. *CIRP Annals-Manufacturing Technology*, 63(2), p.727-749.

Carter, J. T., Melo, A. R., Savic, V., Hector, L. G., & Krajewski, P. E. 2011. Structural evaluation of an experimental aluminum/magnesium decklid. *SAE International Journal of Materials & Manufacturing*, 4(1), p.166-174.

Chen, F. K., Huang, T. B., & Chang, C. K. 2003. Deep drawing of square cups with magnesium alloy AZ31 sheets. *International Journal of Machine Tools and Manufacture*, 43(15), 1553-1559.

Chen, F. K., & Huang, T. B. 2003. Formability of stamping magnesium-alloy AZ31 sheets. *Journal of Materials Processing Technology*, 142(3), p.643-647.

Doerge, E., & Dröder, K. 2001. Sheet metal forming of magnesium wrought alloys—formability and process technology. *Journal of Materials Processing Technology*, 115(1), p.14-19.

Dröder, K. 2001. Analysis on forming of thin magnesium sheets. Dr. Ing. Thesis, IFUM, University of Hannover (in German) .

Gontarz, A., Dziubińska, A., & Okoń, Ł. 2011. Determination of friction coefficients at elevated temperatures for some Al, Mg and Ti alloys. *Archives of Metallurgy and Materials*, 56(2), p.379-384.

Hsu, E., Carsley, J. E., & Verma, R. 2008. Development of forming limit diagrams of aluminum and magnesium sheet alloys at elevated temperatures. *Journal of materials engineering and performance*, 17(3), p.288-296.

Kim, H. K., & Kim, W. J. 2010. Failure prediction of magnesium alloy sheets deforming at warm temperatures using the Zener-Holloman parameter. *Mechanics of Materials*, 42(3), p.293-303.

Kim, H. S., Koc, M., Ni, J., & Ghosh, A. 2006. Finite element modeling and analysis of warm forming of aluminum alloys—validation through comparisons with experiments and determination of a failure criterion. *Journal of Manufacturing Science and Engineering*, 128(3), p.613-621.

Kröhn, M. A., Leen, S. B., & Hyde, T. H. 2007. A superplastic forming limit diagram concept for Ti-6Al-4V. *Proceedings of the Institution of Mechanical Engineers, Part L: Journal of Materials Design and Applications*, 221(4), p.251-264.

Lee, Y. S., Kim, M. C., Kim, S. W., Kwon, Y. N., Choi, S. W., & Lee, J. H. 2007. Experimental and analytical studies for forming limit of AZ31 alloy on warm sheet metal forming. *Journal of Materials Processing Technology*, 187, p.103-107.

Mallick, P.K. 2010. *Materials, design and manufacturing for lightweight vehicles*. Woodhead Pub., Cambridge, UK.

- Naka, T., Torikai, G., Hino, R., & Yoshida, F. 2001. The effects of temperature and forming speed on the forming limit diagram for type 5083 aluminum–magnesium alloy sheet. *Journal of Materials Processing Technology*, 113(1), 648-653.
- Neugebauer, R., Altan, T., Geiger, M., Kleiner, M., & Sterzing, A. 2006. Sheet metal forming at elevated temperatures. *CIRP Annals-Manufacturing Technology*, 55(2), p.793-816.
- Palaniswamy, H., Ngaile, G., & Altan, T. (2004). Finite element simulation of magnesium alloy sheet forming at elevated temperatures. *Journal of Materials Processing Technology*, 146(1), p.52-60.
- Sheng, Z. Q., Jirathearanat, S., & Altan, T. 2004. Adaptive FEM simulation for prediction of variable blank holder force in conical cup drawing. *International Journal of Machine Tools and Manufacture*, 44(5), p.487-494.
- Sheng, Z. Q., & Shivpuri, R. 2006. Modeling flow stress of magnesium alloys at elevated temperature. *Materials Science and Engineering: A*, 419(1), p.202-208.
- Sheng, Z. 2012. A Temperature and Time Dependent Forming Limit Surface for Sheet Metal Forming at Elevated Temperatures. *SAE International Journal of Materials & Manufacturing*, 5(2), p.277-284.
- Sivapragash, M., Lakshminarayanan, P. R., Karthikeyan, R., Hanumantha, M., & Bhatt, R. R. 2008. Hot deformation behavior of ZE41A magnesium alloy. *Materials & Design*, 29(4), p.860-866.
- Stoughton, T. B. 2000. A general forming limit criterion for sheet metal forming. *International Journal of Mechanical Sciences*, 42(1), p.1-27.
- Tari, D. G., & Worswick, M. J. 2015. Elevated temperature constitutive behavior and simulation of warm forming of AZ31B. *Journal of Materials Processing Technology*, 221, p.40-55.
- Verma, R., Hector, L. G., Krajewski, P. E., & Taleff, E. M. 2009. The finite element simulation of high-temperature magnesium AZ31 sheet forming. *Jom*, 61(8), p.29-37.
- Yoshihara, S., Nishimura, H., Yamamoto, H., & Manabe, K. I. 2003. Formability enhancement in magnesium alloy stamping using a local heating and cooling technique: circular cup deep drawing process. *Journal of Materials Processing Technology*, 142(3), p.609-613.
- Zener, C., & Hollomon, J. H. 1944. Effect of strain rate upon plastic flow of steel. *Journal of Applied physics*, 15(1), p.22-32.
- Zhang, K. F., Yin, D. L., & Wu, D. Z. 2006. Formability of AZ31 magnesium alloy sheets at warm working conditions. *International Journal of Machine Tools and Manufacture*, 46(11), p.1276-1280.

CHAPTER 3: An Improved Zener-Hollomon Parameter (Z') and Implementation of Z' -FLS in Hot Stamping

3.1 Introduction

In this chapter, an improved Zener-Hollomon parameter (Z') is proposed to enhance its capability on reflecting strain rate effect on limit strain. Then, the proposed Z-FLS concept is improved by the Z' and a Z' -FLS is constructed for Boron steel sheet material for predicting failure in a hot stamping process.

3.2 Improved Zener-Hollomon parameter (Z')

Zener-Hollomon parameter (Z), or so-called temperature-compensated strain rate factor introduced in Chapter 2 has been used in many studies to define the strain rate and temperature effects on limit strains. The dependency of the effective strains at fracture on $\ln(Z)$ has been observed in hot tensile/torsion test on Al-Mg alloys in bulk shape specimens (Alexandrov et al. 2005) and limit major strains at localized necking from Maciniak test on Al 5083 sheet material (Sheng 2012), critical effective fracture strain in hot compression tests on Ti40 alloy (Zhang et al. 2009), and sheet material AZ31 in a forging-drawing hybrid warm forming condition (Sheng and Shivpuri 2006) and in tensile tests at strain rates ranging from 2×10^{-4} to $1 \times 10^{-1} \text{ s}^{-1}$ and temperatures ranging from 323 to 523°K (Kim et al. 2010).

However, when the Z is used to express the limit strain, two phenomenon can be observed. First, it is found that the limit strains do not fit well with the regressed trend lines when wide range of strain rate change is included. For example, the data point at temperature 480°C and strain rate 10 s⁻¹ in (Alexandrov et al. 2005) and data points at strain rate of 0.1 s⁻¹ from the Marciniak tested FLCs of sheet material Al5083 (Sheng 2012). This phenomenon suggests that the strain rate effect may increase with the increase of strain rate in a nonlinear pattern. On the other hand, the correlation coefficients (R^2) between the regressed lines and measurement of different materials vary widely among different sheet metals, i.e. 74% for Al6111-T4 to 95% for Al5754 under same warm forming conditions (see detail discussion in session 3.2.2). This varying correlation coefficients shows that the strain rate effect also varies among different materials. The varying strain rate effect can be further proven by observing that different material can achieve different limit strain improvements under same strain rate change. For example, at a temperature 250°C, when strain rate decreases from 1.5 to 0.015 s⁻¹, Al5754, Al5182+Mn and Al6111-T4 achieved 140%, 350% and 54% improvement on limit major strain, respectively (Li and Ghosh 2003). On the other hand, boron steel 22MnB5 exhibits much less sensitivity on strain rate change, i.e. the tensile test on Boron steel conducted by Jang et al. (2009) shows very small amount of change of major limit strain.

To reflect the varying strain rate effect, an exponential parameter s , which is named as strain rate sensitivity factor, is introduced into Z parameter to reflect the strain rate effect as below:

$$Z' = \bar{\dot{\epsilon}}^s e^{Q/RT} \quad (3.1)$$

where, s represents the strain rate sensitivity of the material. Since for most materials, the limit strain generally increases with decreasing strain rate (Banabic, 2010), s has a positive value. The contribution from the strain rate increases with increasing value of s . When s is equal to 0, Z' becomes a parameter only governed by the temperature T , and the material does not exhibit any strain rate sensitivity. When s is equal to 1, $Z' = Z$, and the strain rate effect becomes equal at all temperatures.

3.2.1 Determination of s

The limit strain of a sheet material under uniaxial tension can be represented by $\ln(Z')$:

$$\varepsilon^*(\ln(Z')) = A(\ln(Z'))^2 + B(\ln(Z')) + C \quad (3.2)$$

where, A , B , and C in Eq.(3.2) are material parameters that can be determined by curve fitting from measured limit strains at fracture or localized necking at different temperatures and strain rates. The closeness between the estimation from regressed model and measured data can be expressed by R^2 and can be calculated as below:

$$R^2 = 1 - \frac{(\sum (\varepsilon^* - \varepsilon^{*av})(\varepsilon^{*m} - \varepsilon^{*mav}))^2}{\sum (\varepsilon^* - \varepsilon^{*av})^2 \sum (\varepsilon^{*m} - \varepsilon^{*mav})^2} \quad (3.3)$$

where, ε^{*av} is an average value of limit strains ε^* , which is calculated by Equation (3.2), ε^{*mav} is an average value of measured limit strains ε^{*m} from tests. The parameter s can be determined by an optimization process, which treats the R^2 as an objective value that can be maximized by altering the value of s . Using a unconstrained optimization heuristic, e.g.

Golden-section search, the value of s can be determined when the increase of R^2 is smaller than a threshold, e.g. $1e^{-3}$ (Chong and Žak 2013).

3.2.2 Validation of Z'

The effectiveness of the proposed Z' parameter is validated by calculating limit strains of five different aluminum alloys, one magnesium alloy AZ31, and boron steel 22MnB5. Table 3.1 summarizes the setups of those tests. Data set A is from tensile test on samples of bulk shape while the rest of the data are from tests on thin sheet samples under uniaxial tension. In the test for obtaining data set A, the fracture limit strain is defined as $\bar{\varepsilon}^f = \ln\left(\frac{l_f}{l_0}\right)$, where l_0 is the initial length of sample and l_f is its length at fracture. In the tests for obtaining data sets B-D, the major limit strains at fracture were determined by measuring the change in cross-sectional area on a logarithm scale. The major limit strains in data set E are measured at localized necking by using CCD camera.

Table 3.1 Test conditions of seven sets of tests

| No. | Aluminum alloy | Temperature (°C) | Strain rate (1/s) | Test |
|-----|---------------------------------|------------------------|-------------------|----------------|
| A | Al 5xxx bulk shape ¹ | 340, 400, 480 | 0.1, 1, 10 | Tension test |
| B | Al 5182+Mn sheet ² | 25, 200, 250, 300, 350 | 0.015, 0.15, 1.5 | Tension test |
| C | Al 5754 sheet ² | 25, 200, 250, 300, 350 | 0.015, 0.15, 1.5 | Tension test |
| D | Al6111-T4 sheet ² | 25, 200, 250, 300, 350 | 0.015, 0.15, 1.5 | Tension test |
| E | Al 5083-O sheet ³ | 20, 80, 150, 200, 300 | 0.0001, 0.01, 0.1 | Marciniak test |
| F | Mg alloy AZ31 ⁴ | 25, 100, 150, 200, 235 | 0.002, 0.02, 2.0 | Tension test |
| G | 22MnB5 ⁵ | 700, 800 | 0.01, 5.0 | Tension test |

¹: (Alexandrov et al. 2005); ²: (Li and Ghosh 2003); ³: (Naka et al. 2001); ⁴: (Doege and Dröder 2001); ⁵: (Jang et al. 2009)

Figure 3.1-7 give the plots of limit strains from uniaxial tension as square polynomial functions of $\ln(Z)$ and $\ln(Z')$. Table 3.2 gives the material data used for the calculation and s values chosen for each test set along with resulted R^2 values. Results show that, with chosen different s values, varying amounts of improved R^2 values have been achieved for seven different test data. For example, the largest improvement is from sheet material AZ31, the R^2 value increases from 0.78 by using $\ln(Z)$ to 0.99 by using $\ln(Z')$ when s is chosen at 2.4. Similar amount of improvement of R^2 value are achieved on aluminum alloy Al5182+Mn and Al6111-T4. The Boron steel is not sensitive to the strain rate change and thus a small value of 0.4 is chosen for s parameter in $\ln(Z')$. With the improvement, the limits strains of seven different tests can be represented by polynomial functions of $\ln(Z')$ with high R^2 values (>0.94).

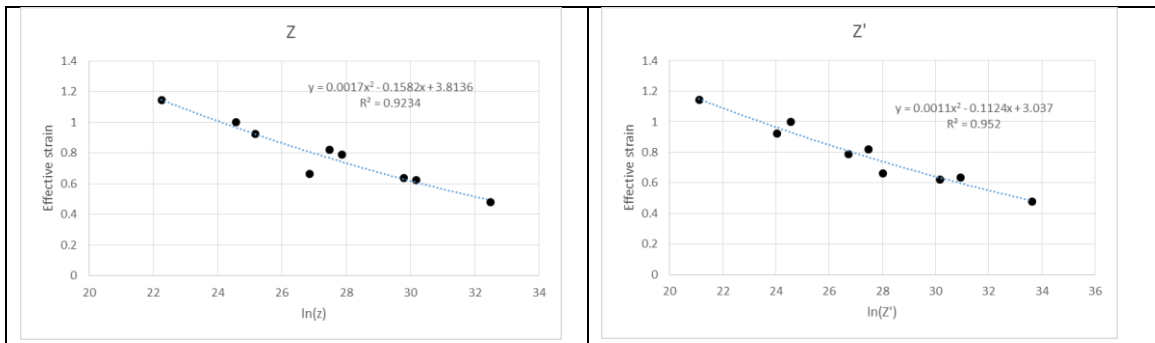


Figure 3.1 Limit strains as polynomial functions of $\ln(Z)$ and $\ln(Z')$ for Al5xxx (test A)

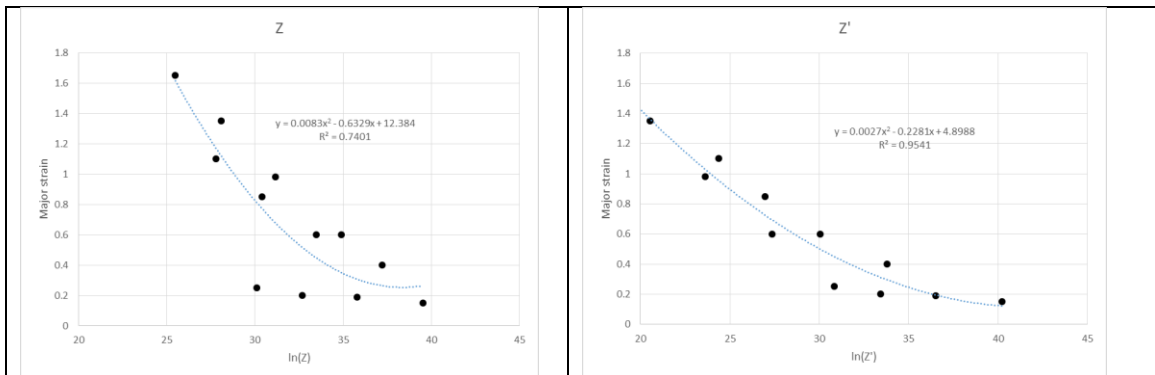


Figure 3.2 Limit strains as polynomial functions of $\ln(Z)$ and $\ln(Z')$ for Al5182+Mn (test B)

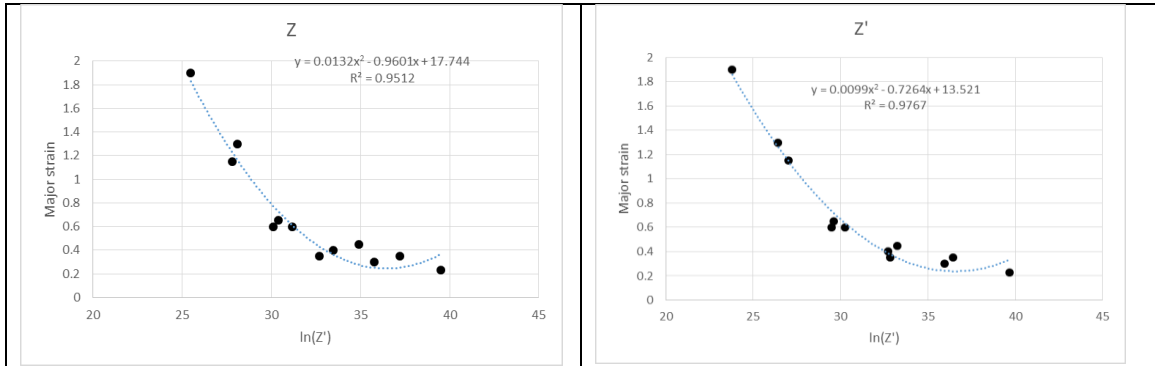


Figure 3.3 Limit strains as polynomial functions of $\ln(Z)$ and $\ln(Z')$ for Al5754 (test C)

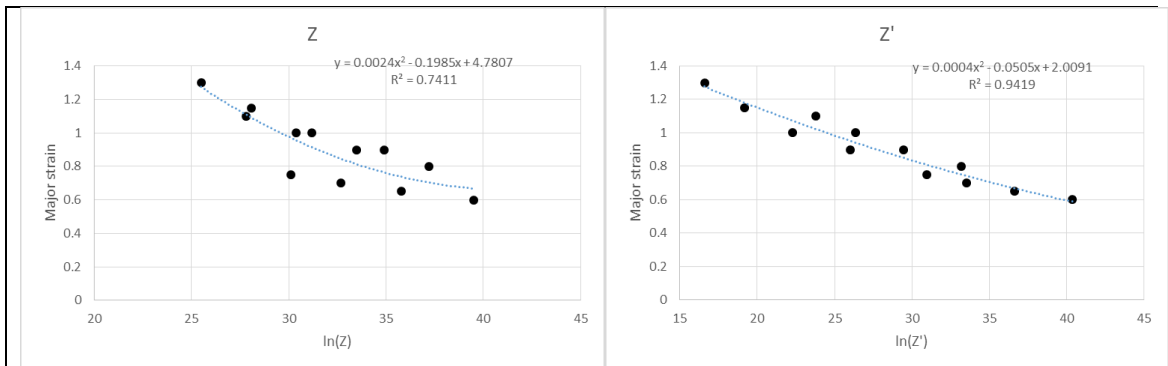


Figure 3.4 Limit strains as polynomial functions of $\ln(Z)$ and $\ln(Z')$ for Al6111-T4 (test D)

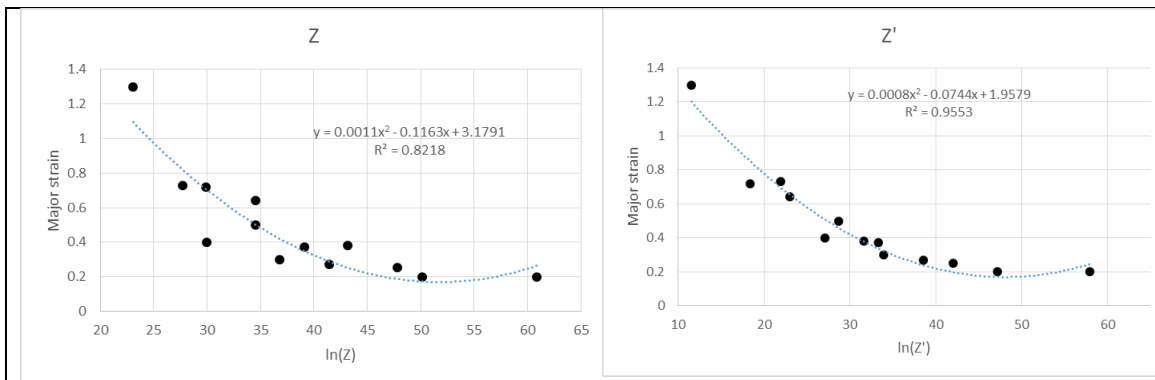


Figure 3.5 Limit strains as polynomial functions of $\ln(Z)$ and $\ln(Z')$ for Al5083-O (test E)

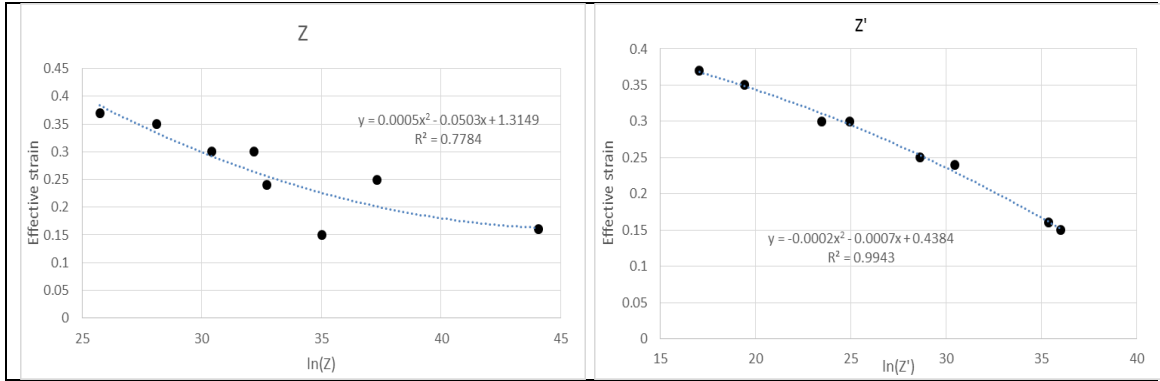


Figure 3.6 Limit strains as polynomial functions of $\ln(Z)$ and $\ln(Z')$ for AZ31 (test F)

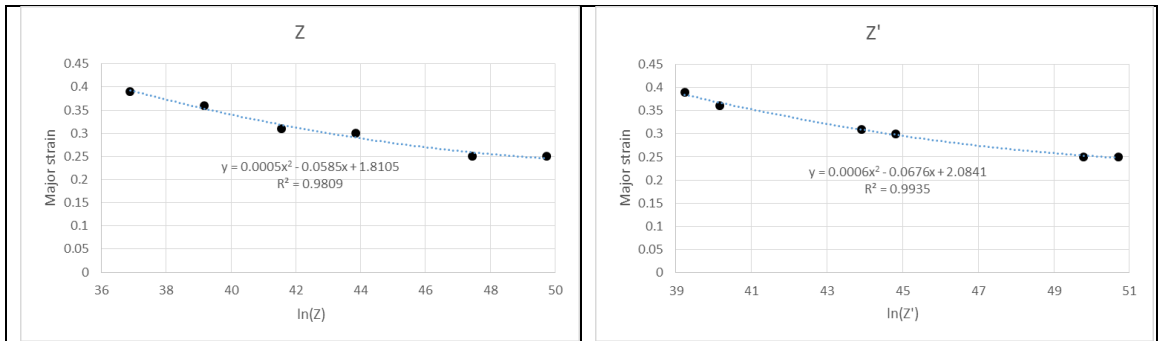


Figure 3.7 Limit strains as polynomial functions of $\ln(Z)$ and $\ln(Z')$ for boron steel (test G)

Table 3.2 Material data used for calculating data points in Figure 3.1-7 and resulted s and R^2

| Test | Gas constant (R) $\text{J mol}^{-1} \text{K}^{-1}$ | Average Activation Energy (Q) kJ mol^{-1} | s | R^2 at | |
|------|--|--|------|----------|-----------|
| | | | | $\ln(Z)$ | $\ln(Z')$ |
| A | 8.31 | 153.7 (Alexandrov et al. 2005) | 1.35 | 0.92 | 0.95 |
| B | 8.31 | 153.7 (Alexandrov et al. 2005) | 3.2 | 0.826 | 0.919 |
| C | 8.31 | 153.7 (Alexandrov et al. 2005) | 1.4 | 0.95 | 0.98 |
| D | 8.31 | 153.7 (Alexandrov et al. 2005) | 3.12 | 0.74 | 0.94 |
| E | 8.31 | 153.7 (Sheng 2012) | 2.25 | 0.82 | 0.96 |
| F | 8.31 | 135 (Sheng and Shivpuri 2006) | 2.4 | 0.78 | 0.99 |
| G | 8.31 | 330 (Eriksson et al. 2002) | 0.4 | 0.984 | 0.994 |

3.3 Z' -FLS and its implementation in Hot stamping

The proposed Z' is used to replace Z in the Z -FLS. To be compatible with the representation of strains in sheet forming, which may range from -2 to 1, the $\ln(Z')$ is normalized as:

$$\overline{\ln(Z')} = \frac{\ln(Z')}{\ln(Z_0)} \quad (3.4)$$

where, Z_0' is calculated at the lowest strain rate and the highest temperature in the process.

Replacing $\ln(Z)$ in Eq.(2.4) with $\overline{\ln(Z')}$, Eq.(2.4) becomes:

$$\varepsilon_1^*(\varepsilon_2, \overline{\ln(Z')}) = A(\varepsilon_2) \overline{\ln(Z')}^2 + B(\varepsilon_2) \overline{\ln(Z')} + C(\varepsilon_2) \quad (3.5)$$

Then, a 3D Forming Limit Surface (Z' -FLS) is constructed using control lines defined by Eq.(3.5). When working with a finite element forming simulation model, the risk of localized necking or failure is indicated by the difference of the major limit strain ε_1^* on the surface and the calculated major strains ε_1 in each element as:

$$\Delta\varepsilon_1 = \varepsilon_1 - \varepsilon_1^* \quad (3.6)$$

The value of Δ can be determined either empirically with a consideration of safety factor, e.g. 10%, or by DIC technology (Wang et al. 2014). If $\Delta\varepsilon_1 \geq \Delta$, a fracture is reported; else if $\Delta > \Delta\varepsilon_1 \geq 0$, a localized necking is reported. In both conditions, the element is painted red in color. If $0 > \Delta\varepsilon_1 \geq -\Delta$, a risk of localized necking is reported and painted yellow in color; otherwise, a safe status is reported and painted green.

3.3.1 Literature review on forming limit in Hot Stamping

In iron carbon alloy system, austenitic phase can transform to hard martensitic phase under a rapid cooling rate or so-called quenching process. Inspired by this mechanism, Swedish company Plannja developed and patterned the hot stamping process (GB14905535 1977), in which quenchable sheet steel is heated to an austenitization temperature and held until fully austenitized, then formed and quenched in a die. Adding

alloying elements boron and Mn, fully martensitic transformation can be achieved at a technically feasible low cooling rate, e.g. about 30°C/s (Aranda et al. 2002). Among several boron steel sheet materials, 22MnB5 is the most commonly used grade in the hot stamping industry (Naderi 2007). At room temperature, the boron steel has a mixed microstructure of ferrite and pearlite, and a tensile strength of about 600MPa. After a fully martensitic transformation, the tensile strength of hot stamped part can reach about 1500MPa. The enhancement of strength leads to a high specific ratio (tensile strength over density) of 1.63×10^5 N.m/kg, which is 18% higher than that of the lightest structural automotive alloy, such as AZ31. To take advantage of such mass saving feature, increasing number of structural components in automotive vehicles are being hot stamped in recent years. From 1997 to 2007, the number of hot stamped parts had significantly increased from 8 million to 107 million (Sheng et al. 2013). According to Volvo Car Group (2013), over 40 percent of safety cage components in new XC90 model are made of hot-stamped boron steel. Along with the fast growth of the hot stamping industry, the past decade has witnessed a rapid development of related technologies and knowledge. A comprehensive review on the development was conducted by Karbasian and Tekkaya (2010).

Thermo-mechanical-metallurgical FEM simulation is an indispensable tool for developing hot stamping process. The simulation can be realized in two ways. Tekkaya et al. (2007) developed a method to reduce computation time about 20% by simulating thermal and mechanical phenomenon separately through two FE codes, MARC 2005 and PAMSTAMP 2G. Another way is to carry out the calculations alternatively in one special purpose software, such as LS-DYNA, AutoForm, PAM-STAMP, and FORGE®. For example, to simulate a hot stamping process of a B-pillar component, Shapiro (2009) used

LS-DYNA, which calculates the plastic deformation by explicit algorithm while solving the thermal problem by implicit time integration. Tang et al. (2014) used FE code FORGE® to simulate a tailor tempering process on a laboratory scale U-channel and validate the prediction on Vickers hardness and microstructure with experimental results.

In stamping FEM simulation analysis, criteria are needed to identify localized necking and fracture failure. According to Åkerström (2006), in the forming stage of hot stamping, boron steel sheet material is in full austenitic phase and its plastic deformation is at temperatures ranging from 500 to 900 °C and strain rates ranging from 10^{-3} to 10/s. In the forming condition, the plastic deformation of boron steel sheet material is primarily due to thermally activated dislocation mobility (Abspoel et al. 2015) while its fracture is due to ductile fracture mechanism (Güler et al. 2014). Recently, Shi et al. (2015) confirmed the ductile fracture mechanism in their tensile tests on 22MnB5 steel sheet material at temperatures ranging from 650 to 800°C and strain rates ranging from 0.01 to 1.0/s. For the ductile fracture mechanism, sheet metal experiences diffuse necking followed by localized necking before fracture (Hostford and Caddell 1993). In tension-compression deformation mode, such process is quite clear and a constant amount of strain $\Delta = \varepsilon_1^f - \varepsilon_1^{nl}$ may develop after the initiation of localized necking (Atkins 1996). The limit major strains at the initiation of localized necking and fracture under different strain paths, which range from biaxial stretching to pure shear, can be plotted as a Forming Limit Curve (FLC) (Banabic 2010).

FLCs of 22MnB5 steel sheet material can be measured at elevated temperatures by conducting Nakajima or Marciniak tests with temperature control (Karbasian and Tekkaya 2010). The general procedure of the tests has three steps: 1) heat the boron steel

sheet material to an austenitization temperature ($\sim 950^{\circ}\text{C}$) and hold until fully austenitized; 2) rapidly cool the coupon to a target temperature to avoid phase transformation; 3) draw the coupon till localized necking. The cooling rate during step 2 is higher than 30K/s . Bariani et al. (2006) used a Nakajima dome tester with temperature control to measure FLC of 1.5 mm thick 22MnB5 sheet material and published a FLC obtained at 600°C and a punch speed of 10 mm/s . Li et al. (2014) used a similar procedure and obtained FLCs of 22MnB5 steel sheet material with thicknesses ranging from 1.4 mm to 1.8 mm at temperatures ranging from 600°C to 800°C . They found that the level of FLCs generally increases with the increasing of temperature and thickness. The thickness effect on FLCs conform to the observation by Pellegrini et al. (2009). In their comparison study on the FLCs measured at 600°C , 22MnB5 steel sheet materials with different thicknesses of 1.5 mm and 1.7 mm were tested by two different institutes (LFT and DIMEG). The temperature effect is observed by many other studies. For example, Cui et al. (2015) measured FLCs of 1.5 mm thick 22MnB5 steel sheet material at temperatures ranging from 400°C to 900°C at a punch speed of 10mm/s and found the levels of FLCs increase with an increase in temperature. Georgiadis et al. (2016) used Nakajima test to investigate initial sheet thickness effect on forming limit of boron steel sheet material under both isothermal and non-isothermal conditions.

3.3.2 Z'-FLS for boron Steel

In this study, a group of FLCs, which were obtained from Nakajima dome test at temperatures ranging from 400 to 900°C at a punch speed of 10mm/s (Cui et al. 2015), are used to construct a Z'-FLS. Table 3.3 gives the chemical composition of the 1.5mm thick 22MnB5 steel used in the test. Figure 3.8 a & b give Nakajima dome tester and obtained

FLCs, respectively. The average major strain rate of 0.2/s before necking is calculated for the dome test with a punch speed of 10mm/s by conducting a FEM simulation. Compared with FLCs measured by Bariani et al. (2008) and Li et al. (2014), several differences are observed: 1) the levels of FLCs increase in temperatures and thickness, but they are less sensitive to the strain rate; 2) the measurement on the lowest major limit strains shift to the right side of FLD and has some dispersions, e.g. at 600°C, major limit strain of 0.2 is measured at minor strain of 0.1 by Bariani et al (2008) while major limit strain of 0.3 is measured by Cui et al. (2014). The difference can be attributed to variation of material properties and different standard used in identifying the initiation of localized necking.

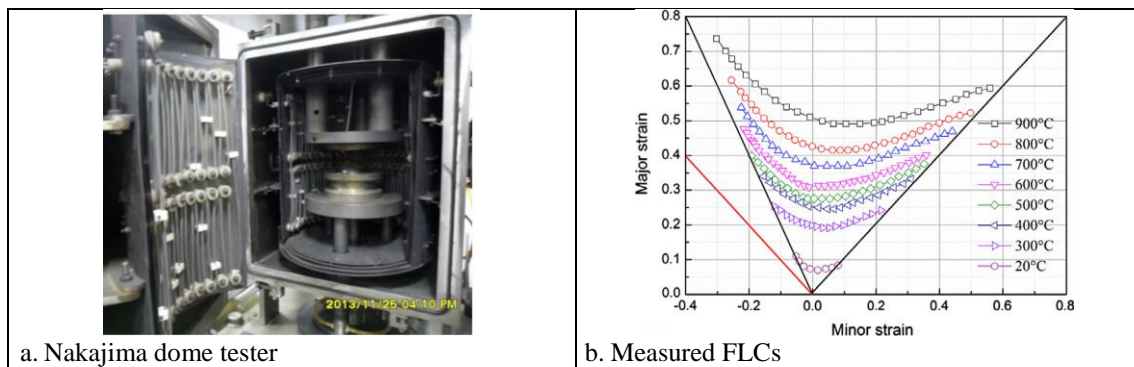


Figure 3.8 Test equipment and obtained FLCs of boron steel sheet material at elevated temperatures (Cui et al. 2015)

Table 3.3 Chemical composition of 22MnB5 (wt. %)

| C | Si | Mn | N | Ni | Cr | Ti | B | Al |
|------|------|------|-------|------|------|------|-------|------|
| 0.23 | 0.22 | 1.18 | 0.005 | 0.12 | 0.16 | 0.04 | 0.002 | 0.03 |

The adjusted FLCs are used to construct a Z' -FLS. To calculate Z' value, the s parameter is chosen at 0.4 as discussed in above section. The $\ln(Z'_0)$ is calculated at 33.19, which represents a process condition at a temperature of 900°C and a strain rate of 0.2/s.

The martensitic transformation starts at about temperature of 425°C (Somani et al. 2001), at which $\ln(Z')$ and $\overline{\ln(Z')}$ are calculated at 56.2 and 1.70, respectively.

Table 3.4 lists the data for constructing Z' -FLS. The values of A , B , and C are determined by using square polynomial curve fitting on the adjusted FLCs at temperatures ranging from 500 to 900°C. With the values of A , B , and C , the R^2 s of those square polynomial regressions are above 0.96. The limit major strains at the temperature of 425°C and strain rate of 0.2/s are calculated from the polynomial regression functions with $\overline{\ln(Z')} = 1.70$. Figure 3.9 displays the constructed Z' -FLS. In the Z' -FLS, the minimum limit major strain is 0.18 at $\overline{\ln(Z')} = 1.70$ and $\varepsilon_2 = 0$, which is the plane strain condition at 425°C while the highest limit major strain is 0.85 in uniaxial stretching condition at 900°C.

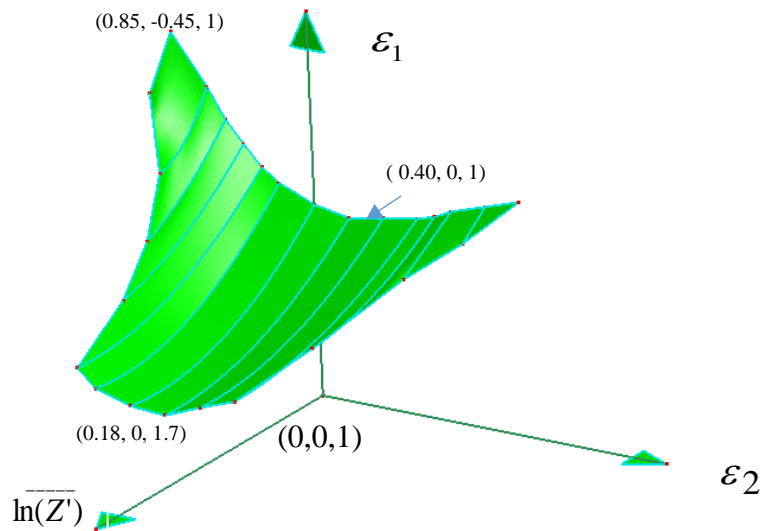


Figure 3.9 Constructed Z' - FLS for 1.5mm thick boron steel sheet material

Table 3.4 Data for constructing Z'-FLS

| T (°C) | $\ln(\bar{Z})$ | Major limit strain at minor strain of | | | | | | | | | | | | | |
|----------------|----------------|---------------------------------------|------|-------|-------|--------|-------|-------|--------|-------|--------|--------|------|------|------|
| | | -0.45 | -0.3 | -0.25 | -0.2 | -0.15 | -0.1 | 0 | 0.1 | 0.2 | 0.3 | 0.35 | 0.4 | 0.5 | 0.6 |
| 900 | 1 | 0.85 | 0.65 | 0.58 | 0.52 | 0.47 | 0.45 | 0.40 | 0.39 | 0.4 | 0.42 | 0.43 | 0.45 | 0.48 | 0.54 |
| 800 | 1.1 | | 0.55 | 0.5 | 0.44 | 0.37 | 0.36 | 0.325 | 0.31 | 0.34 | 0.36 | 0.38 | 0.4 | 0.42 | |
| 700 | 1.21 | | | 0.45 | 0.38 | 0.33 | 0.3 | 0.275 | 0.275 | 0.3 | 0.33 | 0.34 | 0.35 | | |
| 600 | 1.36 | | | 0.34 | 0.28 | 0.25 | 0.21 | 0.215 | 0.25 | 0.28 | 0.3 | 0.33 | 0.34 | | |
| 500 | 1.54 | | | | | 0.27 | 0.23 | 0.19 | 0.21 | 0.23 | 0.28 | 0.305 | | | |
| 425 | 1.70 | | | | | 0.25 | 0.21 | 0.18 | 0.18 | 0.22 | 0.25 | | | | |
| A | | | | | 1.148 | 0.569 | 0.526 | 0.564 | 0.446 | 0.428 | 0.355 | 0.681 | | | |
| B | | | | | -3.22 | -1.824 | -1.79 | -1.83 | -1.483 | -1.41 | -1.184 | -1.959 | | | |
| C | | | | | 2.586 | 1.707 | 1.803 | 1.664 | 1.414 | 1.375 | 1.24 | 1.707 | | | |
| R ² | | | | | 0.997 | 0.959 | 0.99 | 0.992 | 0.970 | 0.994 | 0.961 | 0.995 | | | |

3.3.3 Prediction of failure in Hot Stamping

The constructed Z'-FLS is used to identify localized necking and fracture failure in the FEM simulation of the forming stage of a hot stamping process. NUMISHEET 2008 Bench Mark #3 B-Pillar forming process is used for the case study (Oberpriller et al. 2008). Figure 3.10 gives the physical tool and FE model.

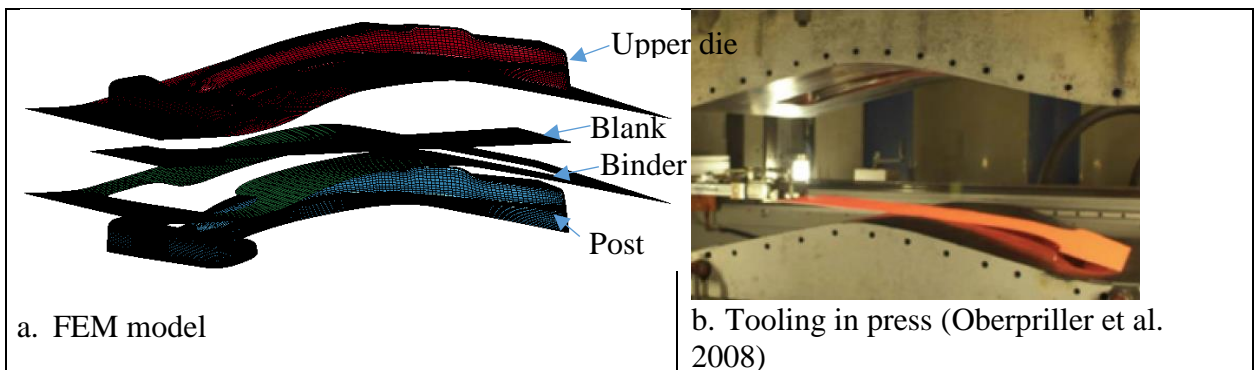


Figure 3.10 NUMISHEET 2008 #3 B-Pillar hot stamping tooling and FEM model

3.3.3.1 FEM Modeling

The thermal mechanical deformation at forming stage is modeled by the implicit and explicit code LS-DYNA (Hallquist 2006), in which the heat transformation and elastic plastic deformation of the sheet material are calculated in a sequential order. The elastic plastic deformation is calculated by an explicit dynamic algorithm while the thermal phenomenon is calculated by an implicit time integration (Shapiro 2009).

The tooling components are modeled as rigid while the sheet blank is modeled as an elastic-viscoplastic material with thermal effects (MAT 106) (Hallquist 2006). The usage of this material model is based on an assumption that the yielding of boron sheet material is isotropic and can be described by von Mises yield criterion (Åkerström 2006).

Sheet blank is initially meshed with 4 node fully integrated shell elements with an average size of 10 mm. During forming simulation, up to two levels of adaptive mesh refinement is used to divide elements on the sheet blank to a size of 2.5mm to capture the small curvature on tooling surface.

Material properties

Table 3.5 gives the material properties and dimensions of the sheet material. Figure 3.11 gives a set of baseline flow stress curves at a strain rate of 0.1/s. The strain rate effect on the flow stress is represented by Cowper-Symonds function s . C and P , which are given in Table 3.6 for temperature ranging from 20 to 1000°C.

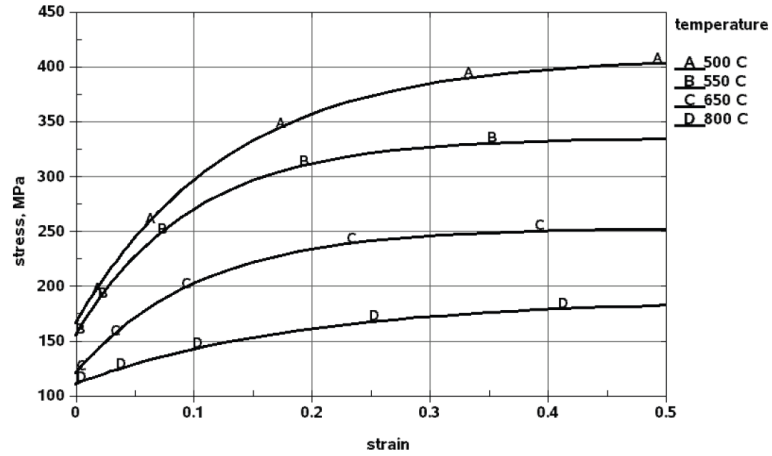


Figure 3.11 Baseline flow stress curves of boron steel 22MnB5 at strain rate of 0.1/s (Shapiro 2009)

Table 3.5 Dimensions and material properties of boron steel sheet material

| | |
|-------------------------------|--|
| Dimensions (mm x mm x mm) | Length x Width x thickness = 1000x250x1.95 |
| Material properties | |
| Density [kg/mm ³] | 7.83e-6 |
| Linear expansion [1/°C] | 1.3e-05 |
| Heat capacity [J/kgK] | 650 |
| Heat conductivity [W/mK] | 32 |
| Flow stress | See baseline in Fig. 3.11 and adjusted by Cowper-Symonds equation for strain rate effect |

Table 3.6 Material parameters C and P of boron steel sheet material (Shapiro 2009)

| | 20°C | 100°C | 200°C | 300°C | 400°C | 500°C | 600°C | 700°C | 800°C | 900°C | 1000°C |
|---|-------|-------|-------|-------|-------|-------|-------|-------|-------|-------|--------|
| C | 6.2e9 | 8.4e5 | 1.5e4 | 1.4e3 | 258.0 | 78.4 | 35.4 | 23.3 | 22.2 | 30.3 | 55.2 |
| P | 4.28 | 4.21 | 4.10 | 3.97 | 3.83 | 3.69 | 3.53 | 3.37 | 3.21 | 3.04 | 2.87 |

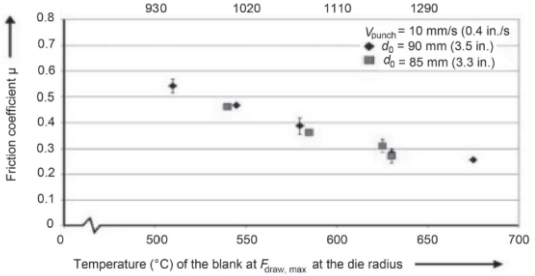
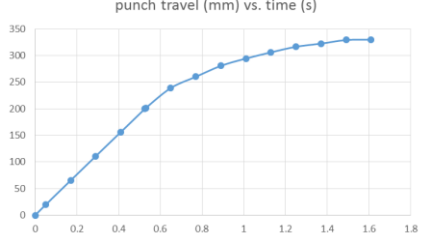
Note: C and P are parameters in Cowper-Symonds function

Boundary conditions

Table 3.7 gives the boundary conditions. At the interfaces between sheet blank and tooling components, the coulomb coefficient of friction is set as a function of temperature while heat-transfer coefficient to tooling component is pressure dependent. The displacement of low die is fixed while the upper die travels downward with a trajectory

shown in Table 3.7. Considering heat loss by convection and radiation during blank transfer from oven to die, the initial blank temperature is set at 810°C while the tool temperature is set and held at 75°C (Shapiro 2009).

Table 3.7 Boundary conditions (Oberpriller et al. 2008)

| | |
|-----------------------------------|---|
| Heat transfer coefficient to air | 160 [W/m ² K] |
| Heat transfer coefficient to tool | P=0 MPa : 1300 [W/m ² K] P=20 MPa: 4000 [W/m ² K] P=40 MPa: 4500 [W/m ² K] |
| Coefficient of Friction |  <p>(Geiger et al. 2008)</p> |
| Upper die travel |  |

3.3.3.2 Results and Discussion

Figure 3.12 gives a temperature distribution on a numerically formed part. Locally different temperatures are caused by the heat exchange with tooling during forming. The maximum temperature is 837°C while the minimum temperature is 561°C. The predicted temperature distribution pattern is similar to that in (Shapiro 2009) and the difference at most locations are within 5%. However, the difference at the predicted lowest temperature is about 11%. A possible reason for the difference is that a pressure dependent friction coefficient other than a constant friction coefficient (Shapiro 2009) is used in this study.

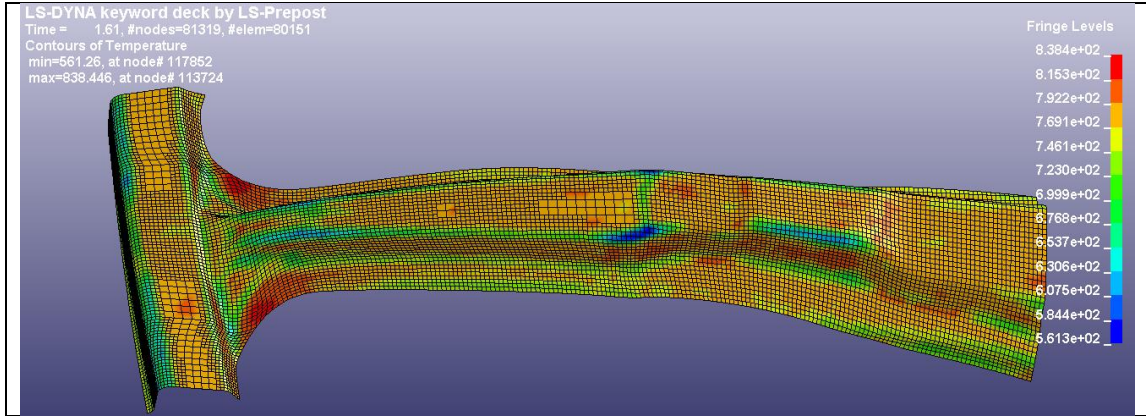
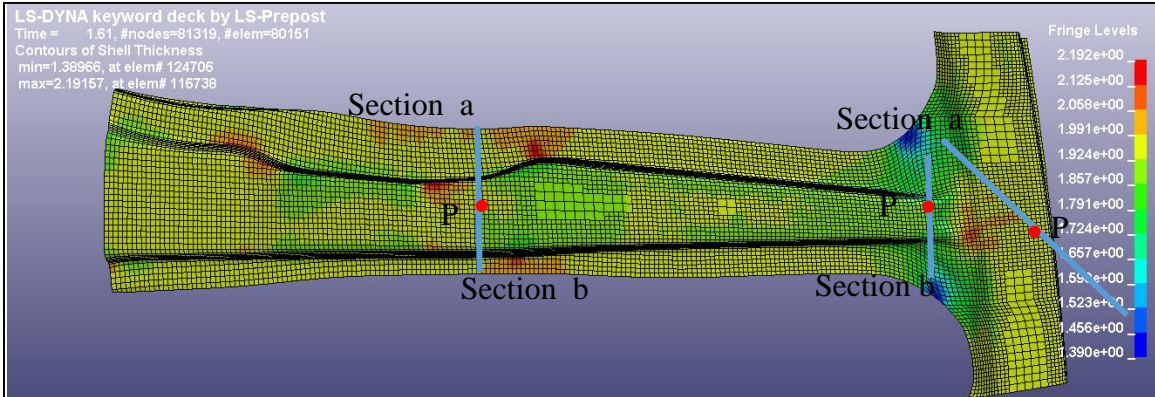


Figure 3.12 Temperature distribution of the numerically formed B-pillar part

Figure 3.13a gives thickness distribution on the numerically formed part. Figure 3.13 b-g shows the predicted thickness and measurement from experiment at six cross sections. A comparison shows that the difference between simulation prediction and experimental measurement is within 5% at most points. The section 1-a is an exception. A slightly high difference (~6.5%) is observed at the edge of the part.

Since 1.95mm thick sheet blank is used in this case study, the constructed Z' -FLS for 1.5mm thick sheet material is offset upward 0.038 in limit major strain to account for 0.45mm increase of sheet thickness. The value of the offset strain is based on the experimental study on the thickness effect on the FLCs of 22MnB5 sheet material (Li et al. 2014).



a. Thickness distribution

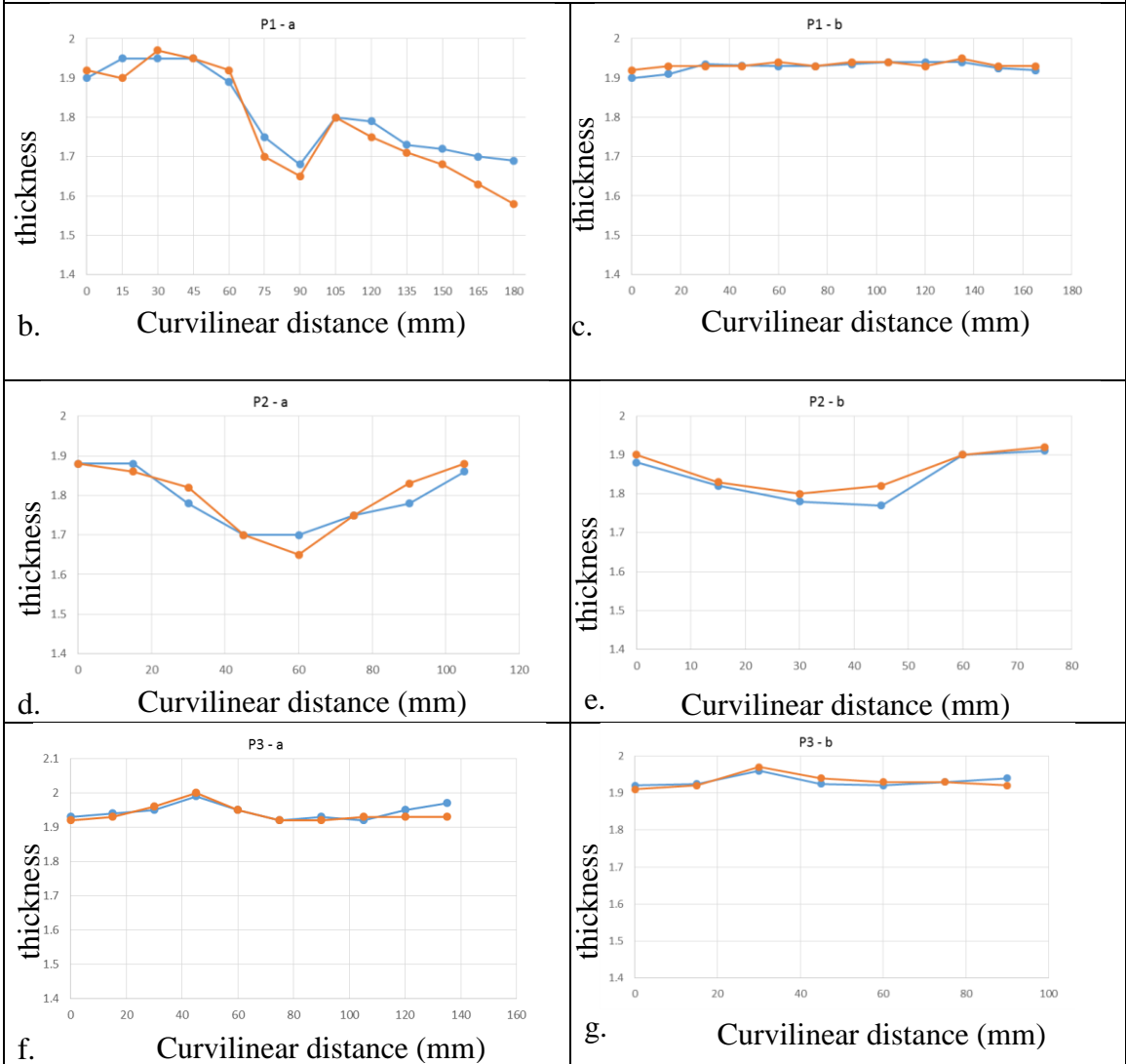


Figure 3.13 a) The thickness distribution in simulation; b-g) comparison of thickness distribution of parts formed in simulation and physical part from experiment at six cross sections from (Oberpriller et al. 2008)

Figure 3.14 provides the failure status of numerically formed B-pillar by plotting 13 representative data points ($\varepsilon_1, \varepsilon_2, \ln(\bar{Z}')$) against the Z' -FLS. Under the Z' -FLS, localized necking happens at element 1 while elements 2, 3 and 6 have a tendency of toward localized necking, but the other elements are safe. The predicted localized necking conforms to the observation in the experiment as shown in Figure 3.14b. Although thinning of element 3 and 6 is higher than that of elements 1 and 2, localized necking is not reported on those two elements due to the combined effect of higher temperatures (830 °C and 838°C) and lower strain rate (0.1/s), which lead to a higher limit major strain of about 0.66 to 0.7 on the Z' -FLS. The reason of element no. 1 necking at the end of stroke is primarily due to the lower temperature of 695°C, which lead to a low limit major strain of 0.34 on the Z' -FLS.

Thinning criterion, e.g. 15% (Cui et al. 2015) and a single FLC, whose FLD_0 is close to that of a FLC measured at 600°C in (Turetta et al. 2006), are still used by the hot stamping industry (Oberpriller B. et al. 2008). Figure 3.15 gives localized necking and fracture prediction by those two criteria. Based on 15% thinning criterion, fracture are overestimated at elements #1, 2, 3, 4, 5 and 6. The FLC predicts localized necking in elements 3 and 6 and risk of localized necking in element 1.

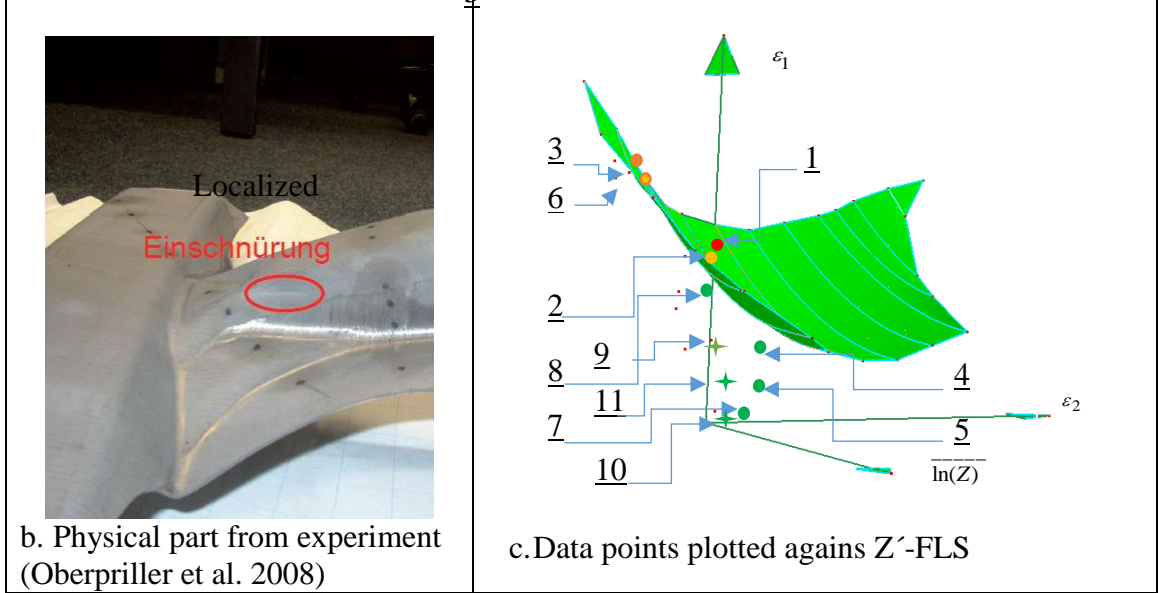
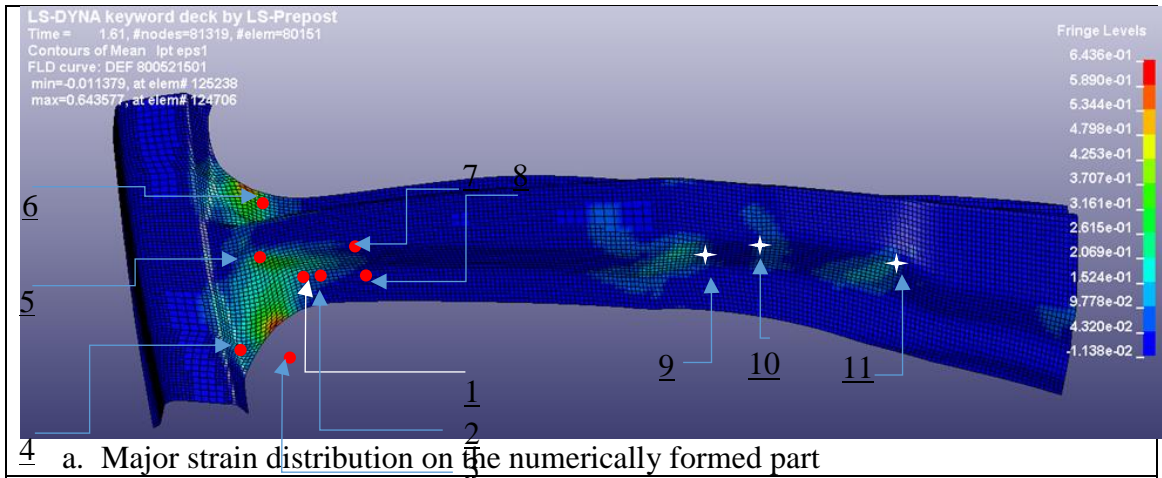
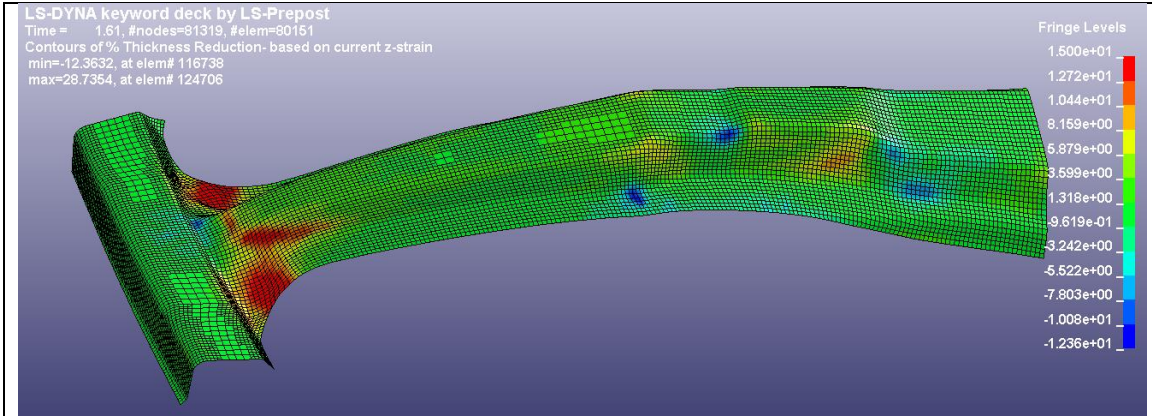
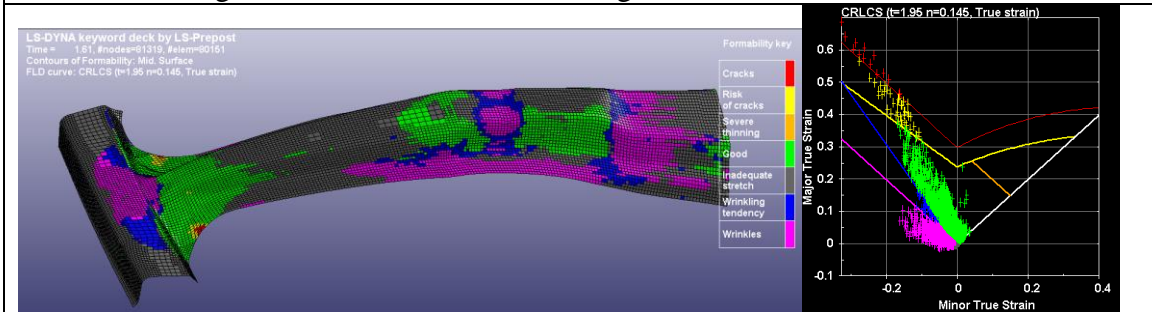


Figure 3.14 Fracture identification in hot forming B-Pillar part with the aid of Z'-FLS



a. Thinning distribution with 15% thinning as cut off value



b. Fracture/localized necking predicted by a FLC at 600°C

Figure 3.15 Fracture/necking prediction by traditional criteria

3.4 Conclusions and discussion

In this chapter, previous proposed Z-FLS concept is revised with an improved Zener-Hollomon parameter (Z'). A Z' -FLS is constructed for 22MnB5 steel sheet material. The constructed Z' -FLS is used to predict localized necking in the FEM simulation of hot stamping an automotive B-Pillar component. Compared with experimental result, the prediction correctly captures the localized necking.

3.5 References:

- Abspoel, M., Neelis, B. M., & van Liempt, P., 2015. Constitutive behaviour under hot stamping conditions. *Journal of Materials Processing Technology*, 228, p.34-42
- Abu-Farha, F. 2011. The development of a forming limit surface for 5083 aluminum alloy sheet. *JOM*, 63(11), p.72-78.
- Åkerström P., 2006. Modelling and simulation of hot stamping. PhD diss., Luleå tekniska universitet/Tillämpad fysik, maskin-och materialteknik/Hållfasthetslära
- Alexandrov, S., Wang, P.T., and Roadman R.E. 2005. A Fracture Criterion of Aluminum Alloys in Hot Metal Forming, *J. Mat. Processing Tech.*, 160, 2005, p 257-265
- Atkins, A. G., 1996. Fracture in forming. *Journal of materials processing technology*, 56(1), p.609-618.
- Balanethiram VS, Daehn GS. 1994. Hyperplasticity-Increased forming limits at high workpiece velocities. *Scripta Metallurgica* 31:p.515–520
- Banabic, D. 2010. *Sheet metal Forming Processes: Constitutive Modeling and Numerical Simulation*, Springer, Heidelberg, Germany. ISBN:978-3-540-88207-7
- Bariani, P. F., Bruschi, S., Ghiotti, A., & Turetta, A. 2008. Testing formability in the hot stamping of HSS. *CIRP Annals-Manufacturing Technology*, 57(1), p.265-268.
- Chong, E. K., & Zak, S. H. 2013. *An introduction to optimization* (Vol. 76). John Wiley & Sons.
- Cui, J., Sun, G., Xu, J., Huang, X., Li G., 2015. A method to evaluate the formability of high-strength steel in hot stamping. *Materials and Design*, 77, p.95-109
- Doege, E., & Dröder, K., 2001. Sheet metal forming of magnesium wrought alloys—formability and process technology. *Journal of Materials Processing Technology*, 115(1), p.14-19.
- Eriksson, M., Oldenburg, M., Somani, M. C., & Karjalainen, L. P., 2002. Testing and evaluation of material data for analysis of forming and hardening of boron steel components. *Modelling and simulation in materials science and engineering*, 10(3), p.277.
- Garcia Aranda, L., Chastel, Y., Fernández Pascual, J., & Dal Negro, T., 2002. Experiments and simulation of hot stamping of quenchable steels. *Adv Technol Plast*, 2, p.1135-1140.
- Geiger, M., Merklein, M., & Lechler, J., 2008. Determination of tribological conditions within hot stamping. *Production Engineering*, 2(3), p.269-276.
- Güler, H., Ertan, R., & Özcan, R., 2014. Investigation of the hot ductility of a high-strength boron steel. *Materials Science and Engineering: A*, 608, p.90-94.
- Hosford, W.F. and Caddell, R.M., 1993. *Metal Forming: Mechanics and Metallurgy*, Prentice Hall, Inc., Englewood Cliffs, USA. ISBN: 0-13-577700-3
- Hallquist, J.O., 2006. Ls-Dyna theory manual. *LSTC, Livermore-California*.LSTC
- Isik, K., Silva, M. B., Tekkaya, A. E., & Martins, P. A. F., 2014. Formability limits by fracture in sheet metal forming. *Journal of Materials Processing Technology*, 214(8), p.1557-1565.
- Jang, J., Lee, J.H., Joo, B.D., & Moon, Y.H., 2009. Flow characteristics of aluminum coated boron steel in hot press forming. *Transactions of Nonferrous Metals Society of China*, 19(4), 913-916.
- Karbasian, H., & Tekkaya, A. E., 2010. A review on hot stamping. *Journal of Materials Processing Technology*, 210(15), p.2103-2118.
- Li, D., & Ghosh, A. 2003. Tensile deformation behavior of aluminum alloys at warm forming temperatures. *Materials Science and Engineering: A*, 352(1), 279-286.

- Li, F. F., Fu, M. W., Lin, J. P., & Wang, X. N., 2014. Experimental and theoretical study on the hot forming limit of 22MnB5 steel. *The International Journal of Advanced Manufacturing Technology*, 71(1-4), p.297-306.
- Li, N., Sun, C., Guo, N., Mohamed, M., Lin, J., Matsumoto, T., & Liu, C., 2015. Experimental investigation of boron steel at hot stamping conditions. *Journal of Materials Processing Technology*, 228,p.2-10.
- Naderi, M., 2007. *Hot stamping of ultra high strength steels*. Lehrstuhl und Institut für Eisenhüttenkunde.
- Oberpriller, B., Burkhardt, L., & Griesbach, B., 2008. Benchmark 3. *continuous press hardening part B: Benchmark Analysis*.
- Patent GB1490535, 1977. Manufacturing a hardened steel article, Norrbottens Jaernverk AB.
- Pellegrini, D., Lechler, J., Ghiotti, A., Bruschi, S., & Merklein, M., 2009. Interlaboratory comparison of forming limit curves for hot stamping of high strength steels. In *Key Engineering Materials* (Vol. 410, pp. 297-304).
- Shapiro, A., 2009. Finite element modeling of hot stamping. *Steel research international* 80.9 (2009): p.658-664.
- Sheng, Z.Q., Shivpuri, R., 2006. A Hybrid Process for Forming Thin-Walled Magnesium Parts, *Mater. Sci. Eng.*, A428, p. 180-187.
- Sheng, Z.Q., 2012. A Temperature and Time Dependent Forming Limit Surface for Sheet Metal Forming at Elevated Temperatures. *SAE International J. of Materials & Manufacturing*, 5.2, p. 277-284.
- Sheng, Z., Wang, Y., Chang, T., Miller, R., & Liasi, E., 2013. *Deep Drawing by Indirect Hot Stamping* (No. 2013-01-1172). SAE Technical Paper.
- Shi, D., Hu, P., & Ying, L., 2015. Comparative study of ductile fracture prediction of 22MnB5 steel in hot stamping process. *The International Journal of Advanced Manufacturing Technology*, p.1-12.
- Somani, M.C., Karjalainen, L.P., Eriksson, M., Oldenburg, M., 2001. Dimensional changes and microstructural evolution in a B-bearing steel in the simulated forming and quenching process. *ISIJ International* 4, p.361–367.
- Stoughton, T. B., 2000. A general forming limit criterion for sheet metal forming. *International Journal of Mechanical Sciences*, 42(1), p.1-27.
- Tang, B. T., Bruschi, S., Ghiotti, A., & Bariani, P. F., 2014. Numerical modelling of the tailored tempering process applied to 22MnB5 sheets. *Finite Elements in Analysis and Design*, 81, p.69-81.
- Volvo Car Group, 2013. New Scalable product architecture enables Volvo car group to move faster towards a crash free future, Dec 12, 2013
- Wang, K., Carsley, J.E., He, B., Li, J., Zhang, L., 2014. Measuring forming limit strains with digital image correlation analysis. *J. Mater. Process. Technol.* 214, p.1120–1130,
- Zener, C., and Hollomon, J.H. (1944). "Effect of strain rate upon plastic flow of steel." *Journal of Applied physics* 15, no. 1, p.22-32.
- Zhang, X. M., Zeng, W. D., Ying, S. H. U., Zhou, Y. G., Zhao, Y. Q., Huan, W. U., & Yu, H. Q., 2009. Fracture criterion for predicting surface cracking of Ti40 alloy in hot forming processes. *Transactions of Nonferrous Metals Society of China*, 19(2), p.267-271.

CHAPTER 4: A New Ductile Failure Criterion for Predicting Sheet Metal Forming Limit

4.1 Introduction

Due to relatively small dimension and contact pressure in thickness direction, stretching driven sheet metal forming takes place under plane-stress mode, in which ductile sheet materials usually fail by localized necking (LN), which follows by fracture (Chung et al. 2014). The major strains and minor strains at vicinity of the LN failure can be plotted into a conventional Forming Limit Curve (FLC) while those at locality of fracture, if post-necking (P-N) deformation is large, can be plotted into a Fracture Forming Limit Curve (FFLC) as shown in Figure 4.1. The failure on a deformed sheet metal part can be identified by plotting its major and minor strains against the obtained FLC in a so-called Forming Limit Diagram (FLD), which is largely due to the systematic work of Keeler (1964) and Goodwin (1968). Under linear strain path or strain path without sharp change of directions, which is the situation in most first draw operations, conventional FLCs can provide an accurate prediction and are thus still widely used by industry. However, the conventional FLCs are sensitive to the change of strain path (Graf and Hosford 1993) and sharp changes of strain path could occur in sheet metal forming processes, i.e. in the first draw of a cavity with a bottom pocket feature and multi-stage forming (Stoughton 2000). To deal with the conditions with strain path changes, less strain path dependent forming limit representations were proposed by transforming conventional strain based FLC into the space of principal stresses (Arrieux 1995, Stoughton 2000, Yoshida et al. 2007) or the space

of effective strain and strain ratio or its equivalency (Zeng et al. 2008, Stoughton and Yoon 2012, Dick et al. 2015).

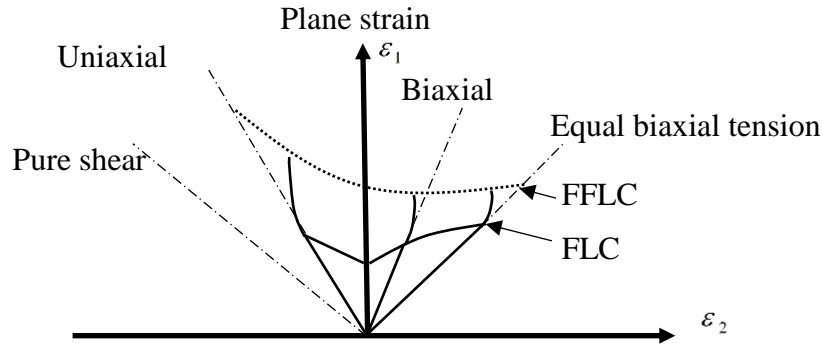


Figure 4.1 Schematic diagram for FLC and FFLC

The FLCs can be experimentally determined by conducting standardized Marciniak test and Nakajima test (ISO 2008). However, considerable time and effort are needed to obtain limit strains along different strain paths. Even with the aid of Digital Image Correlation method (Wang et al. 2014), the cost and effort are still big obstacles preventing industry from obtaining accurate FLCs. Thus, many studies were conducted to find different approaches to predict FLCs under linear and nonlinear strain path conditions. Extensive literature reviews on this subject can be found in (Stoughton and Zhu 2004, Banabic 2010, Bruschi et al. 2014). A brief summary of those approaches that are closely related with present work is given in this section. According to different strategies having been used, those approaches can be classified into four groups as: 1) phenomenological method; 2) instability analysis; 3) Marciniak-Kuczynski (M-K) method; 4) Damage theory.

- 1) Phenomenological method: Based on a semi-empirical formula proposed by Keeler and Brazier (1977), North American Deep Draw Research Group proposed a NADDRG model (Bleck et al. 1998) for calculating FLCs of steel sheet materials, which is still widely used by industry for its simplicity. Recently, based on

previously developed phenomenological method (Volk et al 2012), Volk et al. (2014) proposed a so-called Generalized Forming Limit Concept (GFLC), in which the strain path effect is represented by a metamodel, which was trained by a group of experimentally measured FLCs under different bilinear strain paths. The concept is adopted by AutoForm^{plus} to identify stretching failure under non-linear strain path. Weber et al. (2014) found that the levels of FLCs drop with the increase of effective pre-strain disregarding the pre-straining mode. Based on experimental data on AA6014 from Nakajima test, they modelled the major forming limit as a function effective pre-strain and strain path.

- 2) Instability analysis: Considère (1885) proposed Maximum Force Criterion (MFC) to capture the initiation of diffuse necking in uniaxial tension. Based on MFC, Swift (1952) proposed a formula to calculate limit strains at diffuse necking from strain paths of uniaxial tension to biaxial tension. Under an assumption of proportional strain path deformation and a constraint of zero extension at minor strain direction at initiation of LN, Hill (1952) derived a formula to calculate limit strains at LN in tension compression domain. Based on Swift model, Hora and Tong (1994) suggested the inclusion of additional hardening effect at diffuse necking, which is caused by the gradual strain path change from proportional one to plane strain at the LN, and thus proposed the Modified Maximum Force Criterion (MMFC). The MMFC was able to predict FLC in both proportional and non-proportional strain paths (Hora et al. 2013). Hill (1962) proposed the concept of acoustic tensor and proved that LN corresponds to singularity of its matrix. Chow et al. (2007) used the singularity of acoustic tensor as the critical condition for predicting LN in strain-

softening sheet material Al6061 at an elevated temperature of 450°C. Stören and Rice (1975) suggested that LN can be identified by the appearance of a vertex developed on the yield surface or so-called vertex theory. Chow and Jie (2004) used an anisotropic damage model combined with a modified vertex theory to predict FLC of Al6022 sheet material.

- 3) Marciniak-Kuczynski (M-K) method: The approach assumes the existence of initial geometrical imperfection on the sheet material and the LN is reported once the equilibrium state between the imperfect zone and outside area is broken (Marciniak and Kuczynski 1967). Using M-K theory, under bi-linear strain paths, FLCs of Al2008-T4 sheet material (Graf and Hosford 1993), FLCs of Al2008-T4 and Al6111-T4 sheet materials (Yao and Cao 2002) were predicted. Based on the M-K approach, Crach algorithm was proposed (Gese and Dell 2006). Compared with M-K algorithm, a major improvement in the Crach algorithm is the proposal of a method of calibrating the imperfect factor by measuring the limit strain from uniaxial tension test. The algorithm has been successfully used to predict forming limit under both proportional and non-proportional strain paths (Gese et al. 2013) and now included in the FEM codes PAM-Stamp.
- 4) Damage theory: These type of approaches, which are also called Ductile Failure Criterion (DFC), are based on an assumption that the damage grows during plastic deformation and finally reaches a critical value at the moment of failure. The criterion proposed in present study belongs to this type. A comprehensive review of this type of methods can be found in (Arkins 1996, Bruschi et al. 2014, Aretz et al. 2014). The damage can be defined as a relative size of voids, i.e. volume fracture

of voids, and damage growth can be defined by a function of stress triaxiality ratio $\eta = \frac{\sigma_H}{\bar{\sigma}}$ (a ratio of hydrostatic stress σ_H to the effective stress $\bar{\sigma}$) and increment of effective strain $\bar{\varepsilon}$. Failure is reported once the integration of the damage function reaches a critical value (McClintock 1968, Rice and Tracy 1969). The damage growth can also be empirically or phenomenologically defined (Cockcroft and Latham 1968, Oyane 1972, Brozzo 1972). Primarily due to their straightforward implementation into finite element code as well as their intrinsic easiness in calibration, DFC were used frequently to predict fracture in sheet metal forming processes, such as deep drawing (Takuda et al. 1999). DFC were used to calculate FFLCs for different sheet materials, such as aluminum alloy Al6111 (Jain et al. 1999), mild steel (Han and Kim 2003), mild steel AKDQ (Ozturk and Lee 2007), low carbon steels and high strength steel (Chen et al. 2010), TRIP 690 (Li et al. 2010), DP780 steel (Lou et al. 2012), aluminum alloy Al5182 (Aretz et al. 2014), and St14 steel (Ma et al. 2015).

Several criteria were developed to address the fracture at wider strain paths ranging from pure shear to equal biaxial tension. Bai and Wierzbicki (2010) modified Mohr-Coulomb criterion, which is a stress based phenomenological model, through transforming the criterion to a space of effective strain at fracture ($\bar{\varepsilon}^f$), stress triaxiality (η) and normalized Lode angle ($\bar{\theta}$). The modified criterion was successfully used by Li et al. (2010) to predict the FFLC of TRIP steel under strain paths ranging from pure shear to biaxial tension. Lou et al. (2012) proposed a model, which defines damage growth as a function of effective strain increment, stress triaxiality, and normalized shear stress. Working with FEM modeled Nakajima

dome test, the criterion is able to accurately predict a FFLC for DP780 steel sheet material.

Although a lot of DFC have been developed, those criteria generally define failure at fracture and treat critical damage as a constant. However, in sheet metal forming, for the requirement of cosmetic appearance and performance of sheet metal component, failure is reported at the initiation of LN. At LN, micromechanical studies show that critical damage is affected by both strain path and initial sheet thickness. To provide an accurate reflection of those two critical issues motivates the development of a new ductile failure criterion (DFC) in this study. The presentation of this work starts with a discussion of the definition of stretching failure and critical damage, after which the development of a new DFC is introduced. The developed DFC will be validated by: 1) predicting FLCs in proportional strain path for eight sheet materials different in grades and thicknesses; 2) predicting FLCs of A-K steel in bilinear strain path conditions; 3) predicting failure under nonlinear strain path condition in FEM simulations on reverse draw processes provided by Benchmark #1 study of Numisheet 2014.

4.2 Stretching failure and Critical damage

4.2.1 Stretching failure

As discussed, current available DFC generally define failure at fracture. The definition works fine for the sheet materials without detectable P-N deformation or fracture without LN, such as DP780 (Lou et al. 2012). However, the amount of P-N deformation, which is affected by many factors, such as contact pressure, strain path, initial yield strength, strain rate sensitivity, initial sheet thickness, and relative grain size (Aretz et al. 2014), varies among different sheet materials. Table 4.1 gives a summary of FFLD₀ (major

limit strain at fracture in plane strain), FLD_0 (major limit strain at LN in plane strain) and P-N deformation in percentage of $FFLD_0$ of several sheet metal materials from publication. For seven of eight investigated sheet materials, the measured data shows that the P-N deformation in percentage of total deformation at fracture is above 25%. For some sheet materials like Al1100, the P-N deformation in percentage can be up to 66.6%. Even for TRIP690, an Advanced High Strength Steel (AHSS), the P-N deformation in percentage can be up to 28.5%. DP780 steel sheet material is an exception and it has near zero P-N deformation. To remove the P-N deformation introduced uncertainty, failure shall be reported at LN or fracture without LN. It is worth noting that such definition is accepted by industrial practice and many forming limit studies (Stoughton 2000, Hill 2001, Strano and Colosimo 2006, Bai and Wierzbicki 2008, Volk et al. 2008, Hora et al. 2013).

Table 4.1 Post-necking (P-N) deformation in percentage of eight sheet metal materials

| | $FFLD_0$ | FLD_0 | P-N (%)** |
|-----------------------------|----------|---------|-----------|
| Al1100 (Takuda et al. 2000) | 0.66 | 0.22 | 66.6 |
| Al6111 (Jain et al. 1999) | 0.31 | 0.23 | 25.8 |
| S1 (Han and Kim 2003)* | 0.37 | 0.27 | 27.0 |
| S2 (Han and Kim 2003)* | 0.56 | 0.40 | 28.6 |
| S3 (Han and Kim 2003)* | 0.66 | 0.43 | 34.8 |
| S4 (Han and Kim 2003)* | 0.78 | 0.56 | 28.2 |
| TRIP 690 (Li et al. 2010) | 0.35 | 0.25 | 28.5 |
| DP 780 (Lou et al. 2012) | 0.19 | 0.19 | 0 |

*: S1-S4 are low carbon steels

** : the value is calculated as: $\frac{FFLD_0 - FLD_0}{FFLD_0} \times 100\%$

4.2.2 Critical damage

The critical damage is the microscopic damage at failure, which is usually represented by volume fraction of voids. Micromechanical studies show that the critical damage strongly depends on stress triaxiality. At initial porosities ranging from 10^{-5} to 10^{-3} , which are representative values of porosity in structural alloys, and stress triaxialities ranging from 0.33 to 0.67, which are equivalent to the strain paths from uniaxial tension to equivalent biaxial tension, an ascending trend of critical damage has been calculated by Perrin (1992) and Benzerga et al. (1999) through using Gurson model (1977). Their results are supported by direct microscopic measurements (Benzerga and Leblond 2010). In a study on damage in sheet metal forming, Schmitt and Janinier (1982) observed that the critical damage at LN was strongly affected by the strain path. Compared with the critical damage developed under uniaxial tension, 2 to 10 times greater damage can be developed under equal biaxial tension. Tasan et al. (2009) also found that increased critical damage at plane strain and biaxial tension in their study on DP steel sheet material. Their results show that the critical damage at LN increases slightly from 0.21% in uniaxial tension to 0.27% in plane strain then increases greatly to 1.09% in equal biaxial tension.

Janilier and Schmitt (1982) found that the initial sheet thickness also affected the damage. They defined the initial damage of sheet material as a function of $\left(\frac{r_3}{t}\right)$ - ratio between void radius r_3 and initial sheet thickness t . Under this definition, thicker sheet tends to have a lower initial damage level and thus needs larger plastic deformation to reach the critical damage. The theory can explain the commonly observed phenomenon that thicker sheets have higher forming limits (Raghavan 1995). Based on above studies, it is

proposed in current study that the effect of strain path and initial sheet thickness shall be included into the critical damage definition.

4.3 A ductile failure criterion

Based on above discussion on the stretching failure and critical damage, a ductile failure criterion is developed in this section.

4.3.1 Model

Using a simple form of McClintock model (1968), at fracture, the critical damage value can be expressed as an integration of stress triaxiality η during the plastic deformation as:

$$D_{cri} = \int \eta d\bar{\epsilon} \quad (4.1)$$

In sheet metal forming, sheet material experiences uniform plastic deformation, followed by diffuse necking, and localized necking (LN) before fracture. The occasionally observed diffuse necking stage is shallow and can be ignored due to its low possibility (Hill 2001). At the initiation of LN, the localized area deforms approximately in plane strain mode ($\eta = \frac{\sqrt{3}}{3}$). After (Atkins 1996), the limit strain in Eq.(4.1) can be integrated before and after LN as:

$$D_{cri} = \int_0^{\bar{\epsilon}^n} \eta d\bar{\epsilon} + \frac{\sqrt{3}}{3} \bar{\Delta} \quad (4.2)$$

where, $\bar{\epsilon}^n$ is the effective strain at LN while $\bar{\Delta} = \bar{\epsilon}^f - \bar{\epsilon}^n$ is the effective strain of P-N deformation. Since the failure is defined at LN, the item $\bar{\Delta}$ is dropped to reflect the definition. To reflect the effect of initial sheet thickness and strain path on the critical

damage, an effect function $f(t, \rho)$ is introduced into Eq.(4.2). t is the initial sheet thickness, which is used to represent initial sheet thickness effect on critical damage. ρ is a ratio of incremental minor strain to major strain ($\rho = \frac{d\varepsilon_2}{d\varepsilon_1}$). Eq.(4.2) then becomes:

$$f(t, \rho)D_{cri}^u = \int_0^{\bar{\varepsilon}^n} \eta d\bar{\varepsilon} \quad (4.3)$$

where D_{cri}^u is the critical damage in uniaxial tension and can be expressed by a corresponding limit strain. The effect function in uniaxial tension is chosen to be unity and is used as a reference of other strain paths. Obviously, at moment of failure, for a given sheet metal material, the left side of Eq.(4.3) suggests that the critical damage can be expressed as an envelope of limit strain, which is governed by current strain ratio ρ . Obviously, such definition is equivalent to the strain path independent effective strain FLC criterion (Zeng et al. 2008) and compatible with another path independent effective strain limit representation (Stoughton and Yoon 2012, Aretz et al. 2014). Under isotropic hardening law and associated flow rule, the definition can be transformed into the stress space representation, such as stress based FLC (Stoughton 2000). The right side of Eq.(4.3) defines the absolute damage growth. A failure is reported once the calculated absolute damage equals or larger than the critical damage defined by the left side of equation.

Under proportional loading assumption, using Hill'48 normal anisotropic plastic yield condition, which is after many studies such as Takuda et al. (1999), Stoughton (2000), and Stoughton and Yoon (2012), η and $d\bar{\varepsilon}$ can be represented by strain ratio and normal anisotropy parameter r . Eq.(4.3) becomes:

$$f(t, \rho)D_{cri}^u = \frac{1+r}{3}(1+\rho)\varepsilon_1^n \quad (4.4)$$

where, $r = \frac{r_0 + 2r_{45} + r_{90}}{4}$ and $\varepsilon_1^n(t, \rho)$ is the major limit strain along any strain path. The algebraic derivation of this equation can be found in Appendix C. The critical damage at uniaxial tension can be determined as:

$$D_{cri}^u = \frac{(1+r)(1+\rho^u)}{3} \varepsilon_1^n(t, \rho^u) \quad (4.5)$$

D_{cri}^u can be calibrated in uniaxial tension test, in which the strain ratio is defined as $\rho^u = \frac{-r}{1+r}$ for considering the effect of normal anisotropy (Banabic 2010), and can be

calculated as $D_{cri}^u = \frac{\varepsilon_1^n(t, \rho^u)}{3}$.

4.3.2 Calculation limit strains at liner strain path

From Eq.(4.4 & 4.5), major limit strain at any strain path between uniaxial tension and equal biaxial tension can be expressed as:

$$\varepsilon_1^n(t, \rho) = \frac{(1+\rho^u)f(t, \rho)\varepsilon_1^n(t, \rho^u)}{(1+\rho)} \quad (4.6)$$

Correspondingly, the effect function can be determined as:

$$f(t, \rho) = \frac{(1+\rho)\varepsilon_1^n(t, \rho)}{(1+\rho^u)\varepsilon_1^n(t, \rho^u)} \quad (4.7)$$

To determine the effect function, the expression of effect function at two critical strain paths, namely plane strain (PS) and equal biaxial tension (EBT), are determined first.

From Eq.(4.7), the effect function in PS can be expressed as:

$$f(t,0) = \frac{\varepsilon_1^n(t,0)}{(1 + \rho^u)\varepsilon_1^n(t, \rho^u)} \quad (4.8)$$

and the effect function at EBT can be expressed as:

$$f(t,1) = \frac{2\varepsilon_1^n(t,1)}{(1 + \rho^u)\varepsilon_1^n(t, \rho^u)} \quad (4.9)$$

where $\varepsilon_1^n(t,0)$ and $\varepsilon_1^n(t,1)$ are major limit strains along paths of PS and EBT.

Using linear shape function given by Hill (1952) for strain path at negative strain ratios ($\rho^u \leq \rho \leq 0$) and non-linear shape function of Stören and Rice (1975) strain path at positive strain ratios ($0 \leq \rho \leq 1$), the major limit strain at negative quadrant and positive quadrant of *FLD* can be calculated as:

$$\varepsilon_1^n(t, \rho) = \begin{cases} \varepsilon_1^n(t,0) + \frac{\rho}{\rho^u}(\varepsilon_1^n(t, \rho^u) - \varepsilon_1^n(t,0)), & (\rho^u \leq \rho \leq 0) \\ \varepsilon_1^n(t,0) + (-0.414\rho^2 + 1.414\rho)(\varepsilon_1^n(t,1) - \varepsilon_1^n(t,0)), & (0 \leq \rho \leq 1) \end{cases} \quad (4.10)$$

Dividing both sides of Eq.(4.10) by $\varepsilon_1^n(t, \rho^u)$, the effect functions can be calculated as:

$$f(t, \rho) = \begin{cases} (1 + \rho) \left\{ f(t,0) + \left[\frac{1}{1 + \rho^u} - f(t,0) \right] \frac{\rho}{\rho^u} \right\}, & (\rho^u \leq \rho \leq 0) \\ (1 + \rho) \left(f(t,0) + (-0.414\rho^2 + 1.414\rho) \left(\frac{f(t,1)}{2} - f(t,0) \right) \right), & (0 \leq \rho \leq 1) \end{cases} \quad (4.11)$$

4.3.3 Determination of $f(t,0)$ and $f(t,1)$

The material constants of effect function can be determined by using data from a set of critical forming limit test of sheet materials of same grade but with different thicknesses. The determined effect function can then be used to calculate forming limits of same class of sheet materials, which shall have similar microstructure and strengthening mechanism.

At here, test data of A-K steel and Al 3003 sheet metals from (Jalinier and Schmitt 1982) is used to determine the material constants. In their tests, both tested sheet materials were treated as isotropic and thus $\rho'' = -0.5$. For aluminum alloy Al3003, the major limit strains $\varepsilon_1^n(t, \rho_u)$, $\varepsilon_1^n(t,0)$ and $\varepsilon_1^n(t,1)$ are measured from tested FLCs at three different thicknesses of 0.4 mm, 0.8 mm and 1.2 mm. For A-K steel sheet material, the major limit strains are converted from thickness strains, which were measured from samples with three different initial sheet thicknesses of 0.4 mm, 1.0 mm, and 1.3 mm. Based on the test data, the effect functions $f(t,0)$ and $f(t,1)$, can be approximated as a linear function and a polynomial function of initial sheet thickness t , respectively as:

$$f(t,0) = A_0 t + B_0 \quad (4.12 \text{ a})$$

$$f(t,1) = A_b t^2 + B_b t + C_b \quad (4.12 \text{ b})$$

Table 4.2 gives the material constants of two types of sheet materials.

Table 4.2 Determined material constants for the effect functions

| | A_0 | B_0 | A_b | B_b | C_b |
|-----------|--------|--------|---------|--------|--------|
| A-K steel | 0.1883 | 0.9031 | -0.543 | 2.4878 | 1.9523 |
| Al3003 | 0.0871 | 1.1458 | -2.1232 | 4.4862 | 1.8239 |

4.3.3 Parametric study

To illustrate the effect of initial sheet thickness t and strain ratio ρ on the effect function $f(t, \rho)$ and FLCs, a parametric study is conducted. A given state of $t=1\text{mm}$, $\varepsilon_1^n(t, \rho^n) = 0.4$, $r=1$, and $\rho^n = -0.5$ of a steel sheet metal material is assumed as a baseline condition. The parametric study is conducted by calculating effect function and major limit strains at different sheet thicknesses and strain ratios.

Figure 4.2a plots the variation of effect function $f(t, \rho)$ under different initial sheet thickness t and strain ratio ρ . The plotted curves show that the effect function increases slightly from uniaxial tension ($\rho^n = -0.5$) to plan strain ($\rho = 0$) then increases quickly to peak values at equivalent biaxial tension ($\rho = 1$). The plotted trend conforms to the observed variation of critical damage values (Janilier and Schmitt 1982) and (Tasan et al. 2009). At same strain ratio, Figure 4.3a also shows that larger initial sheet thickness leads to greater value of effect function, which reflects that thicker sheet metal material has higher resistance to failure.

Since greater value of effect function is at thicker sheet and high strain ratio, major limit strains are plotted against strain ratio in belled-shapes while major limit strains increase with the increase of initial sheet thickness at each strain ratio, see Figure 4.2b. This conforms to generally observed shapes of FLCs and thickness effect on FLCs (Hosford and Caddell 1993).

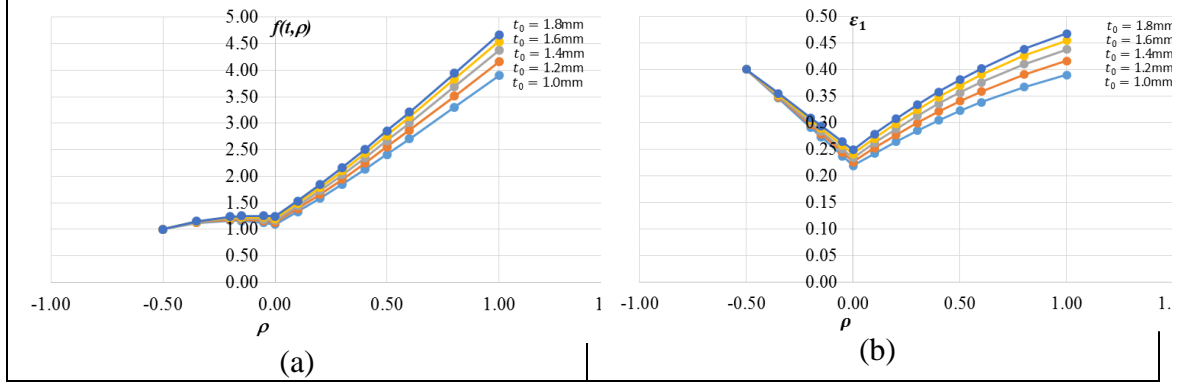


Figure 4.2 Effect of initial sheet thickness and strain path on: a. effect function; b. major limit strain

4.3.4 Working under Non-linear strain path

Along a non-linear strain path or working with a FEM simulation, the damage growth in any element on a deformed sheet material can be calculated as:

$$D = \frac{3}{\varepsilon_1^n(t, \rho^u) \langle f(t, \rho) \rangle} \int_0^{\bar{\varepsilon}^n} \eta d\bar{\varepsilon} \quad (4.13)$$

where effect function $f(t, \rho)$ is defined by Eq.(4.11). In each time step of calculation, a linear strain path is assumed. A failure is reported when the damage value D reaches a unity. Please note that the parameter t is a constant value for each target sheet material and thus does not change during the forming simulation.

4.4 Calculation of FLCs under proportional strain path

4.4.1 Calculation procedure

As discussed in section 4.3.2, the major limit strain under linear strain path can be determined by three steps: 1) measuring the $\varepsilon_1^n(t, \rho^u)$ from tests in uniaxial tension, if several data points are with minimum strain ratio ρ_{\min} , the lowest $\varepsilon_1^n(t, \rho_{\min})$ is used for a conservative prediction; 2) calculating major limit strains $\varepsilon_1^n(t, 0)$ and $\varepsilon_1^n(t, 1)$ by using

determined effect functions Eq.(4.8&4.9); 3)calculating major limit strain of any other strain paths by using Eq.(4.10).

In the test, the major limit strain $\varepsilon_1^n(t, \rho^u)$ can be measured by widely used Digital Image Correlation (DIC) analysis and recently developed necking detecting methods, such as DIC-based time dependent measurement method (Wang et al. 2014). The data point at strain ratio of ρ^u may not be available due to the difficulty of measurement, i.e. grid size is not small enough to capture the LN along the uniaxial tension strain path (Sheng 2008). Based on Eq.(4.7), the $\varepsilon_1^n(t, \rho^u)$ can be calculated by:

$$\varepsilon_1^n(t, \rho^u) = \frac{\varepsilon_1^n(t, \rho_{\min})(1 + \rho_{\min})}{(1 + \rho^u)f(t, \rho_{\min})} \quad (4.14)$$

Table 4.3 Mechanical properties, thickness of the sheet materials used for the case study

| | Thickness (mm) | UTS (Mpa) | Uniform elongation (%) | K (MPa) | n | r bar |
|--|----------------|-----------|------------------------|---------|-------|-------|
| Al-Mg-Si alloy (Wang et al. 2014)* | 1.00 | 91.2 | 21 (total) | n/a | n/a | 0.77* |
| AA 5182 (BM01-2)(Volk et al. 2008)** | 1.10 | 317.0 | n/a | 507.7 | 0.280 | 0.78 |
| 0.8mm HS-IF (BM01-1-08) (Volk et al. 2008)** | 0.8 | 460.0 | n/a | 753.0 | 0.194 | 1.83 |
| 1.6mm HS-IF (BM01-1-16) (Volk et al. 2008)** | 1.6 | 418.3 | n/a | 818.1 | 0.194 | 2.12 |
| Low carbon steel (Han and Kim 2003) | 0.3 | 385.0 | 18.6 | 608.0 | 0.160 | 1.2 |
| DP780 (lou et. al 2012) | 1.00 | 878.0 | n/a | 1429.0 | 0.180 | 1.00 |
| TRIP780 (Stoughton et al. 2013)*** | 1.05 | 775.6 | 19.9 | 1554.0 | 0.292 | 0.84 |
| TRIP690 (Li et al. 2010) | 1.60 | 690.0 | n/a | 1276.0 | 0.270 | 1.00 |

*: based two aluminum sheet materials AA6111 (Jain et al. 2000), r value is assumed at 0.77 in this study and the measured major limit strains from Marciniak test are based on ISO 12004-2 (2008) standard (Wang et al. 2014)

** : data is from Numisheet 2008 benchmark #1

***: data is from Numisheet 2014 benchmark #1

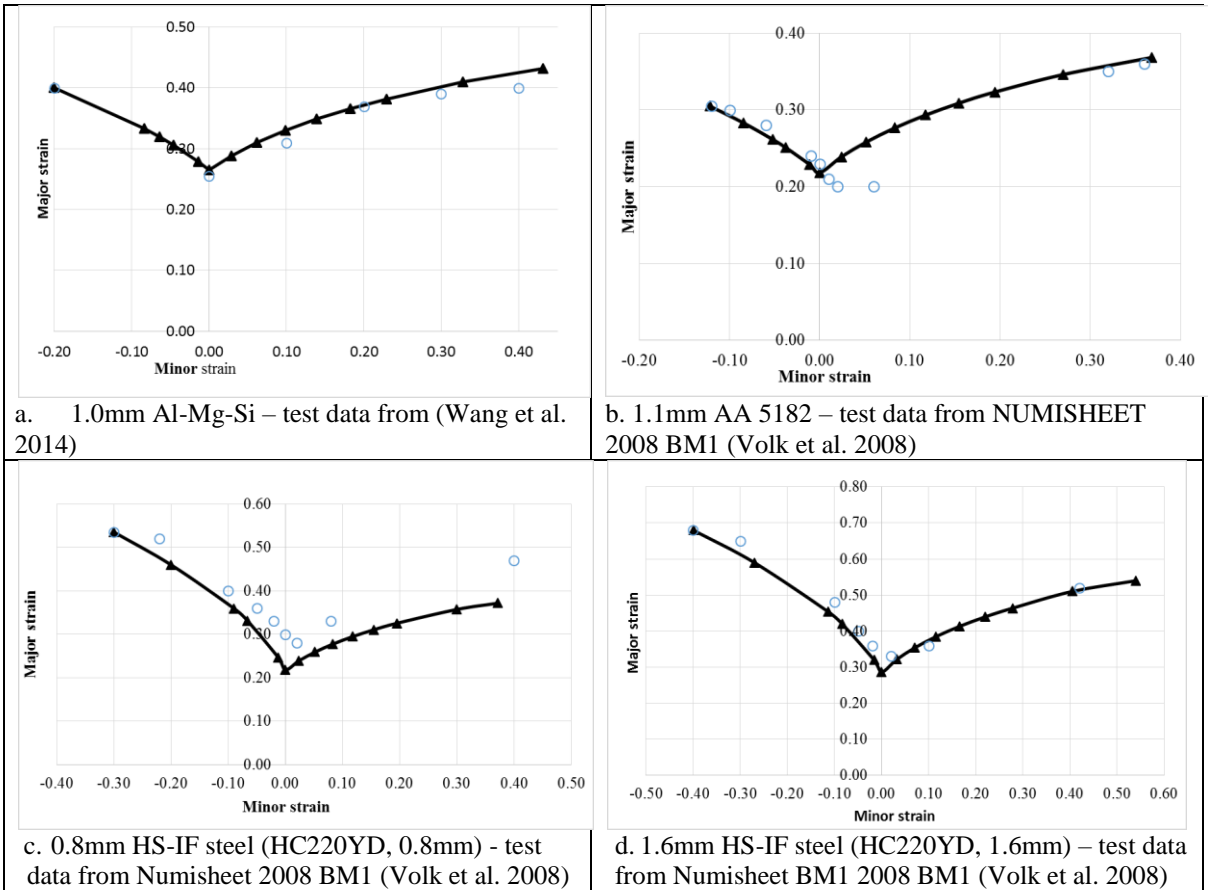
Published forming limit data of eight different sheet materials are used to validate the proposed calculation method. The sheet materials include two aluminum alloys, two high strength IF steels of different thicknesses, one thinner gauge low carbon steel, three advanced high strength steel of different thicknesses. Table 4.3 lists the mechanical properties of those sheet materials. Test data for three sheet materials (two High Strength IF (HS-IF) sheet steels and aluminum alloy sheet material A15182) are from NUMISHEET 2008 benchmark #1 (Volk et al. 2008) and 1.05mm TRIP780 is from Numisheet 2014 benchmark #1 (Stoughton et al. 2013).

4.4.2 Results and discussion

4.4.2.1 Comparison with experimental measurement

Figure 4.3 shows the calculated FLCs and experimental measurements. Comparison between the calculated FLCs and experimental measurement was conducted by calculating difference in true strain at critical strain paths of FLDu (Uniaxial Tension - UT), FLD0 (plane strain - PS) and FLDb (equal biaxial tension - EBT) as illustrated in Figure 4.4. The FLDu is measured at data point with the second smallest strain ratio as suggested by Numisheet benchmark #1 (Volk et al. 2008). Table 4.4 summarizes the calculated deviations. Since the limit major strains at smallest strain ratio were used to calibrate the criterion, the difference (Δ FLDu) is low (0~0.06 in true strain) in all cases. Comparison on other strain paths shows that in six of eight cases, calculated FLCs are quite close to the measured data points. For example, Δ FLD0 and Δ FLDb of two aluminum sheet materials and four steel sheet materials (0.3mm thick low carbon steel, 1.0mm thick DP780 steel, 1.6mm IF and 1.05mm thick TRIP780) are below 0.063 in true strain. The predicted FLC for 1.05mm TRIP780 pass through the scatter of measured data points and thus the

deviations at three strain paths are calculated as zero. Relatively large deviation can be found on the 0.8mm thick HS-IF sheet steel and 1.6mm thick TRIP690 steel, $\Delta FLDB$ are calculated at 0.149 and 0.11 in true strain for 0.8mm IF steel and TRIP690 steel, respectively. The deviations show that the effect functions for steel, which were determined by using forming limit data of AK-steel, does not reflect the strain path and thickness effect on the thin gauge HS-IF steel and thick gauge TRIP steel as effectively as it does on the DP steel and low carbon steel.



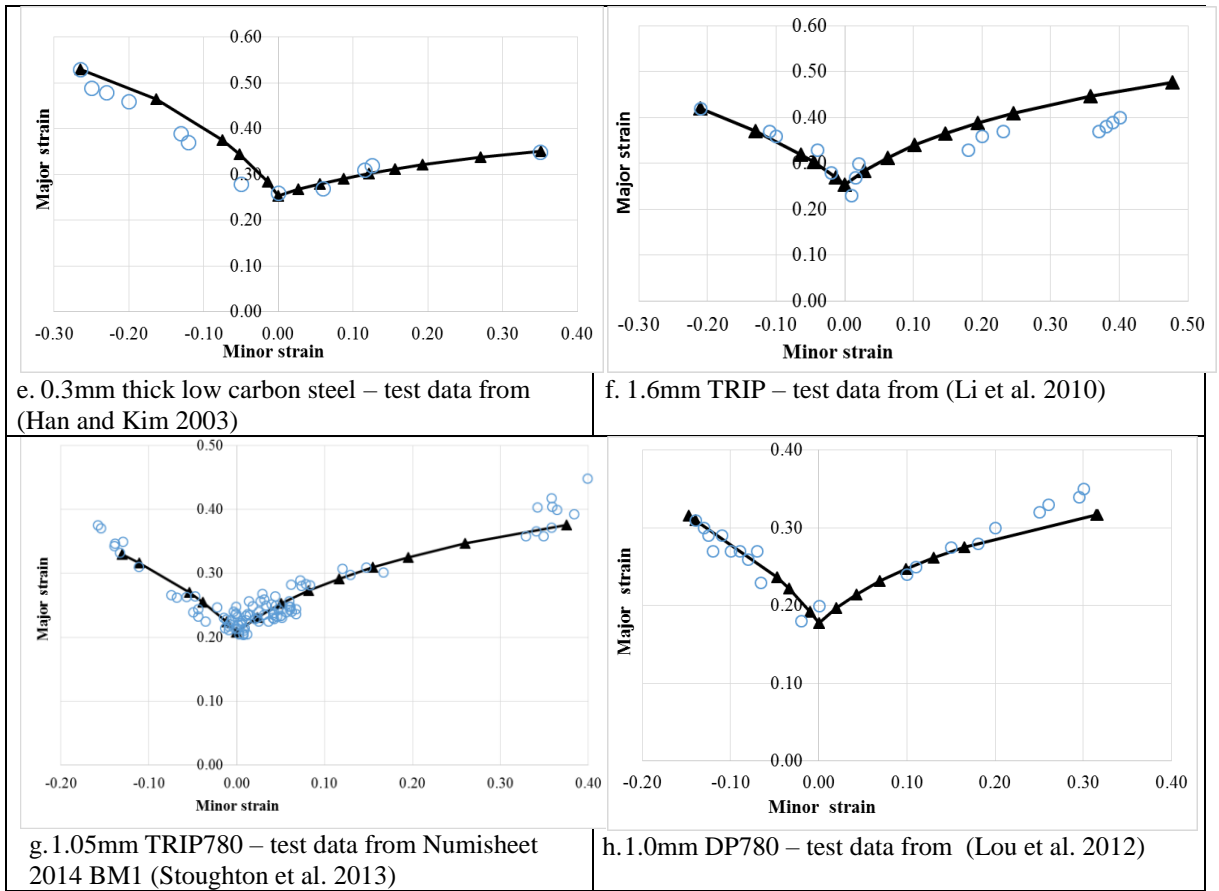


Figure 4.3 FLCs predicted by the proposed ductile failure criterion (solid line) and experimental measurements (circles)

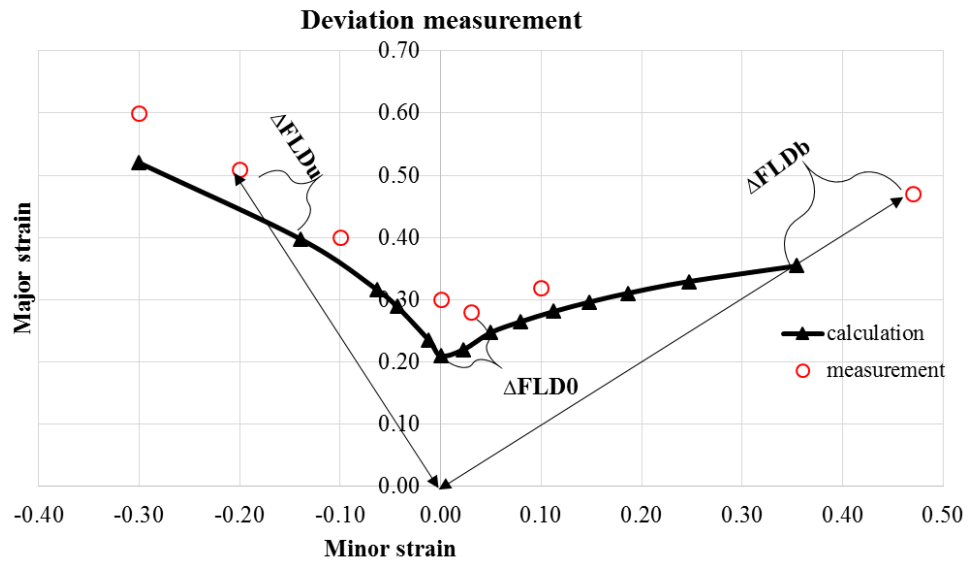


Figure 4.4 Illustration of the difference between calculated FLC and measured data points

Table 4.4 Deviations in true strain from measurement at three critical strain paths by using present algorithm

| | Deviation from experimental data | | |
|---|----------------------------------|----------------|----------------|
| | ΔFLD_u | ΔFLD_0 | ΔFLD_b |
| 1.0mm Al-Mg-Si alloy (Wang et al. 2014) | 0 | 0.005 | 0.026 |
| 1.1mm AA 5182 Numisheet BM1 (Volk et al. 2008) | 0.005 | 0.027 | 0.005 |
| 0.8mm HS-IF Numisheet 2008 BM1 (Volk et al. 2008) | 0.060 | 0.063 | 0.149 |
| 1.6mm HS-IF Numisheet 2008 BM1 (Volk et al. 2008) | 0.058 | 0.048 | 0.022 |
| 0.3mm low carbon steel (Han and Kim 2003) | 0.02 | 0.01 | 0.03 |
| 1.6mm TRIP 690 (Li et al. 2010) | 0 | 0.025 | 0.11 |
| 1.05mm TRIP780 Numisheet 2014 BM 1(Stoughton et al. 2013) | 0 | 0 | 0 |
| 1.0mm DP780 (Lou et. al 2012) | 0 | 0.015 | 0.032 |

4.4.2.2 Analysis on the results of sheet materials from Numisheet 2008 BM1

The predicted FLCs on three sheet materials from Numisheet 2008 BM1 are further compared with FLCs from other participants of the benchmark study. The purpose of Numisheet 2008 BM1 is to provide an objective evaluation of different algorithms. The reference FLCs of the three sheet materials were experimentally determined by the BMW Group using Nakajima tests. A total sixteen submissions from eight participants were included in the benchmark study. The approaches used by the participants include theoretical model with M-K approach, generalized geometry with using Crach approach, theoretical model with Modified Maximum Force Criterion (MMFC), and numerical calculation with different failure criteria etc. Table E1 in Appendix E gives a list of approaches used by each participants.

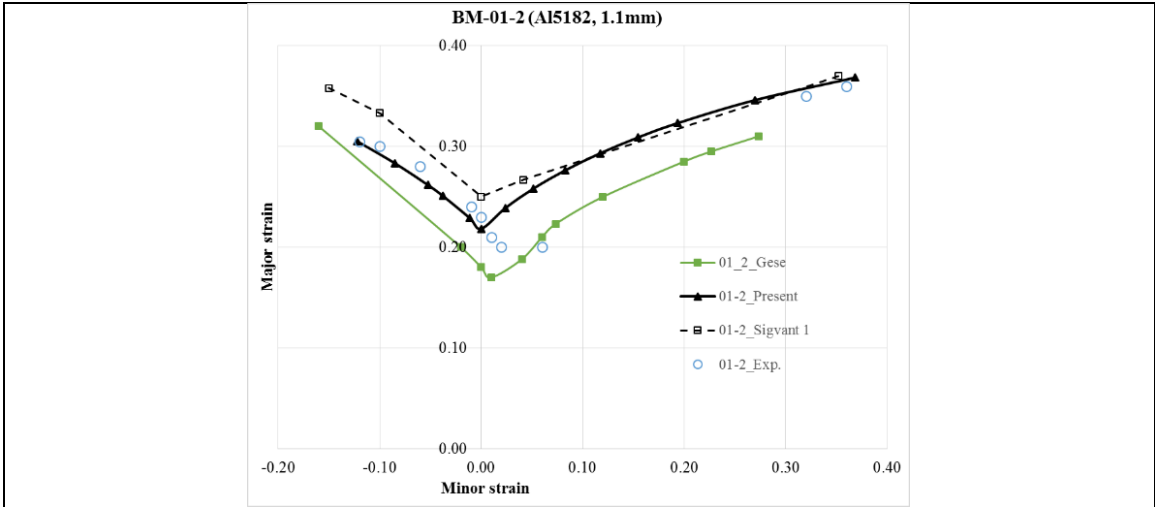
Among the sixteen submissions, Crach approach of Gese submission provided the smallest total deviation while the submission of Signant 1, which used numerical model with Nakajima geometry and a failure determination method developed by Sigvant et al. (2008), provided a result with a total deviation at about the average level of all submissions. To have a better understanding of the effectiveness of the present approach, the FLCs

calculated by the present approach, which is labeled with a suffix of “_Present”, are compared with the results from “Gese” and “Signant 1” as shown in Figure 4.5. Table 4.5 gives total and breakdown of deviations by using three approaches. The sum of deviation of three sheet materials from present algorithm is 0.437 in true strain, which is about 0.014 in true strain larger than the result of Gese and 0.301 in true strain smaller than that from the submission of Sigvant 1, respectively.

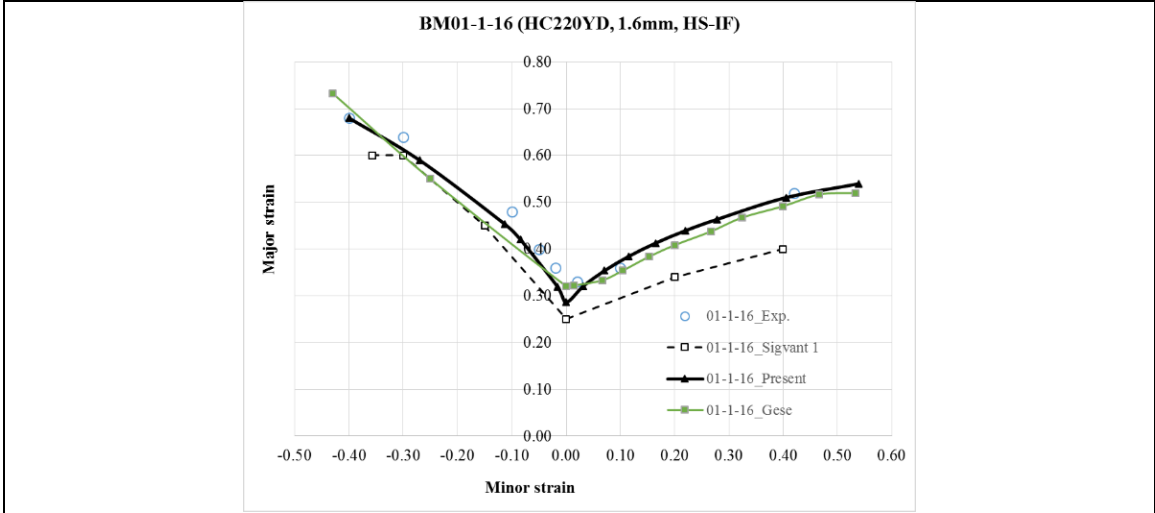
Table 4.5 Comparison on the deviations (total and breakdown) in true strain of calculated FLCs of three sheet materials from Numisheet 2008 BM1

| | 0.8mm HS-IF | 1.6mm HS-IF | 1.1mm Al 5182 | Total |
|-----------|-------------|-------------|---------------|-------|
| Sheng | 0.272 | 0.128 | 0.037 | 0.437 |
| Gese | 0.145 | 0.119 | 0.159 | 0.423 |
| Sigvant 1 | 0.287 | 0.340 | 0.113 | 0.738 |

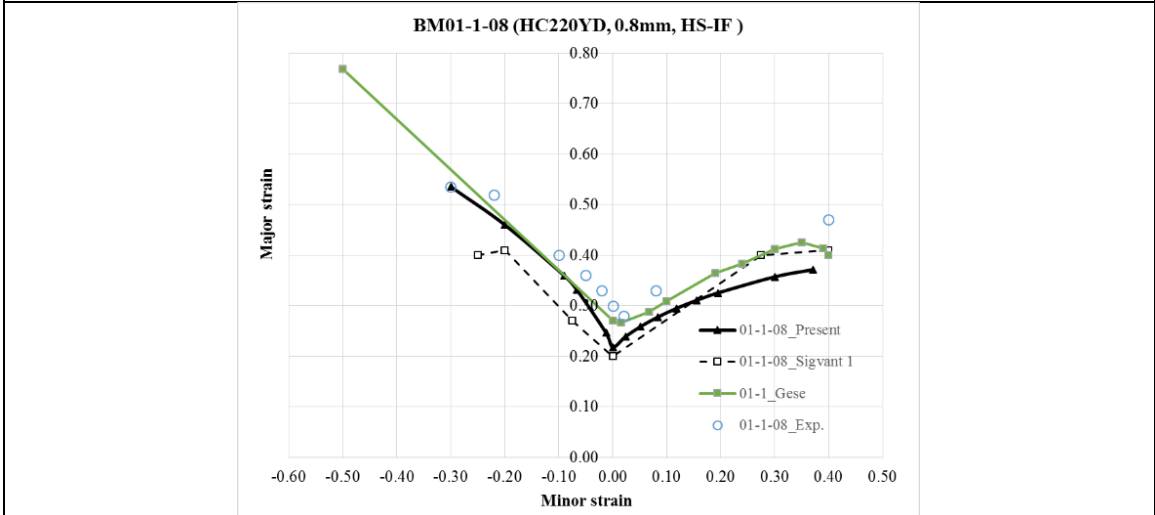
A small total deviation (0.037 in true strain) on the case of sheet material 1.1mm AA5182. The predicted FLC by using present approach pass through measured data points at UT and EBT while a deviation of 0.037 in true strain is primarily contributed by Δ FLD0. The deviation can be largely due to the spherical punch caused right shift of measurement from Nakajima test (Leppin et al. 2008). The total deviation of prediction from present approach on sheet material 1.6mm HS-IF is slightly greater (0.010 in true stain) than that from Gese, which is primarily caused by the lower prediction at FLD0. The total deviation on the sheet material 0.8mm HS-IF from present algorithm is 0.127 in true strain greater than that from Gese’s submission but 0.015 in true strain smaller than that from Sigvant 1. Comparison also shows that three predicted FLCs on 0.8mm thick HS-IF are all lower than the measurement and such trend can be also observed on other submissions (Volk et al. 2008). Despite the different amounts of deviations, the shapes of FLCs predicted by using present approach are visually very close to those from Gese submissions, which were in the best geometrical accordance with the measured FLCs (Volk et al. 2008).



a. 1.1mm Al5182



b. 1.6mm HS-IF



c. 0.8mm HS-IF

Figure 4.5 FLCs measured from test and calculated by using algorithm of present study and two representative submissions of Numisheet 2008 BM#1 (Volk 2008)

4.5 Calculation of FLCs under bilinear strain path

FLCs at bilinear strain paths are calculated to validate the path independent feature of the proposed criterion. Experimental data of 0.89mm thick A-K sheet steel from (Ghosh and Laukonis 1976 and Stoughton 2000) are used for the validation. The tensile properties of this sheet steel are given in Table 4.6.

Table 4.6 Tensile properties of A-K sheet steel (Ghosh and Laukonis 1976)*

| YS (MPa) | UTS (MPa) | Uniform strain | Total strain | K (MPa) | n | r |
|----------|-----------|----------------|--------------|---------|-------|---------|
| 160 | 286 | 0.264 | 0.403 | 508 | 0.234 | 1.1~1.9 |

*All properties are average according to $x_{avg} = \frac{x_0 + 2x_{45} + x_{90}}{4}$, where the subscripts refer to the angles between the pulling and sheet rolling directions.

The experiments were conducted on a Marciniak type tester. FLCs were measured on the sheet material: 1) as-received; 2) with Equivalent Biaxial Tension (EBT) pre-strains of 0.031, 0.067, and 0.119 of true strain; 3) with Uniaxial Tension (UT) pre-strains of 0.068, 0.0091, and 0.14 true strain parallel to the major strain axis of the secondary forming process.

The calculation is carried out by using Eq.(4.13) in two steps. First, calculate the damage growth at a pre-strain condition, i.e. under pre-strained Equivalent Biaxial Tension (EBT) 0.031, D is calculated at 0.219; Second, calculate the damage growth at different strain path and a limit major strain is determined once D reaches unity, i.e. when $\rho = 0$ (at plane strain), major limit strain ε_1^n is determined at 0.29 while the minor strain stays at 0.031 (Figure 4.6c). It is noted that r value of the sheet material decreases from 1.9 at zero pre-strain to 1.1 at 0.26 effective pre-strain (Ghosh and Laukonis 1976). To be consistent in the calculation, r is chosen at 1.1.

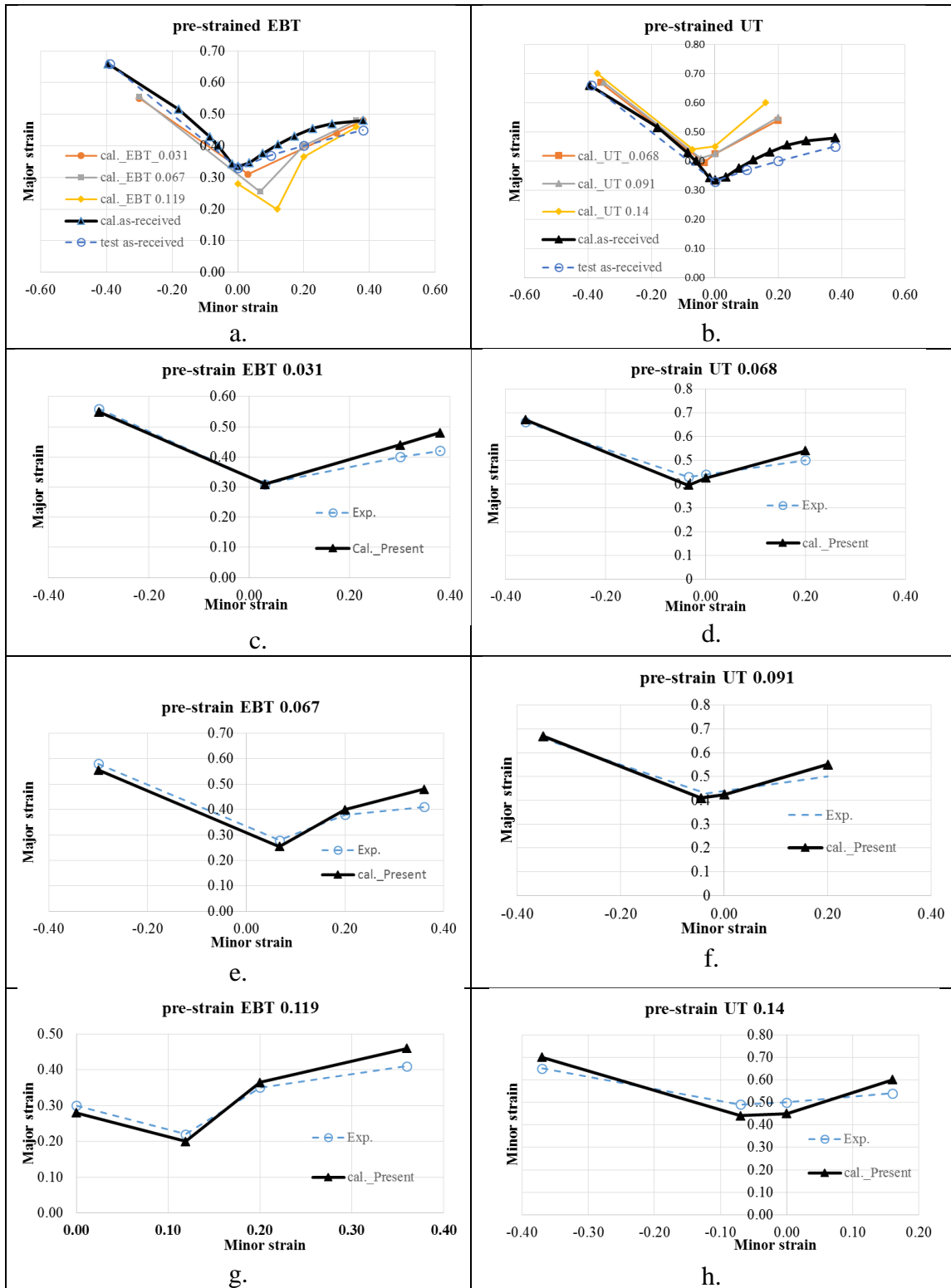


Figure 4.6 Calculated FLCs and experimentally measured FLCs: a) as-received and calculated at with different equivalent biaxial pre-strains; b) as-received and calculated at with different uniaxial tension pre-strains; c – h give comparison between calculation and measurement on each pre-strain condition.

Figure 4.6 summaries the predicted FLCs and tested FLCs from different pre-strain conditions. The calculated FLCs (Figure 4.6a) show a clear trend that FLCs shift downward to right side with the increase of EBT pre-strain. Under UT pre-strain condition (Figure 4.6b), calculated FLCs moves upward to the left side of FLD with the increase of pre-strain level. Figure 4.6c-h show that the predicted FLCs match quite well with experimental measurement. Slightly large difference can be observed at biaxial tension strain path. For example, in the case of EBT pre-strain 0.031, the calculated limit major strain is about 0.07 higher in true strain. However, such difference is within the range of experimental error as suggested by (Zeng et al. 2008).

4.6 Prediction failure in FEM simulation under non-linear strain path

The 2014 Numisheet Benchmark #1 is a benchmark study on evaluating the predictability of forming limit under nonlinear strain path. In the study, nonlinear strain path was created by conducting reverse draws (Li et al. 2013). The draw process on sheet material 1.05mm thick TRIP780 is chosen for validating the proposed criterion under non-linear strain path condition. FEM simulation results and LN identified by using the present approach are compared with experimental results and predictions from nine Benchmark submissions by using different approaches, which include Modified Mohr-Coulomb criterion – BM1-02 (Bai and Wierzbicki 2010), CrachFEM –BM1-04 (Gese et al. 2013), Generalized Forming Limit Concept (GFLC) – BM1-05 from Volk's group (Gaber et al. 2016). In Appendix E, Table E2 gives a list of algorithms used by those participants and Table E3 gives a list of abbreviation of the tests on sheet material TRIP780.

4.6.1 Experimental setup

The experiments were carried out at the Department of Mechanical Engineering, Wayne State University by using a 100-ton INSTRON™ single action hydraulic press (Wu 2013). Figure 4.7a gives the tool components, experimental setup, and corresponding forming procedure. Circular beads were formed into flat blanks in the stage 1 to restrain the metal flow in the following forming stage. Reverse draws were then conducted in stage 2, in which the punch draw the blank into die cavity with a velocity of 0.085mm/s and a strain path change was triggered by the sheet contacting the top surface of the elliptical dome shaped insert. Strain paths can be altered by changing the height of the insert using shims (one shim or four shims) and changing the blank shapes as shown in Figure 4.7. During draws, sheet blanks were clamped between the binder and die. A 3D Digital Image Correlation (3D-DIC) measurement technology was used to record the real-time strain distribution on the top surface of the deformed blank. Three replications were conducted on each condition for repeatability evaluation.

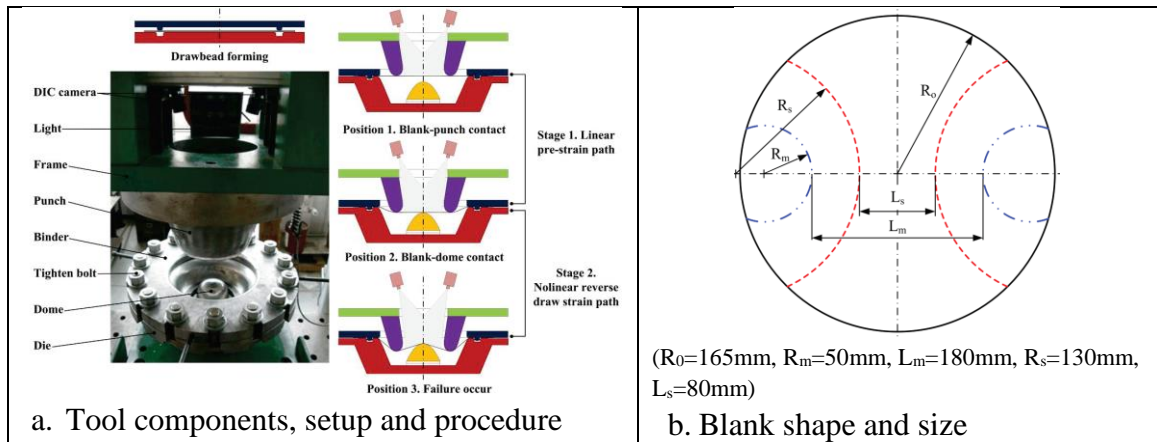


Figure 4.7 Experimental setup for Benchmark #1 of Numisheet 2014 (Wu 2013)

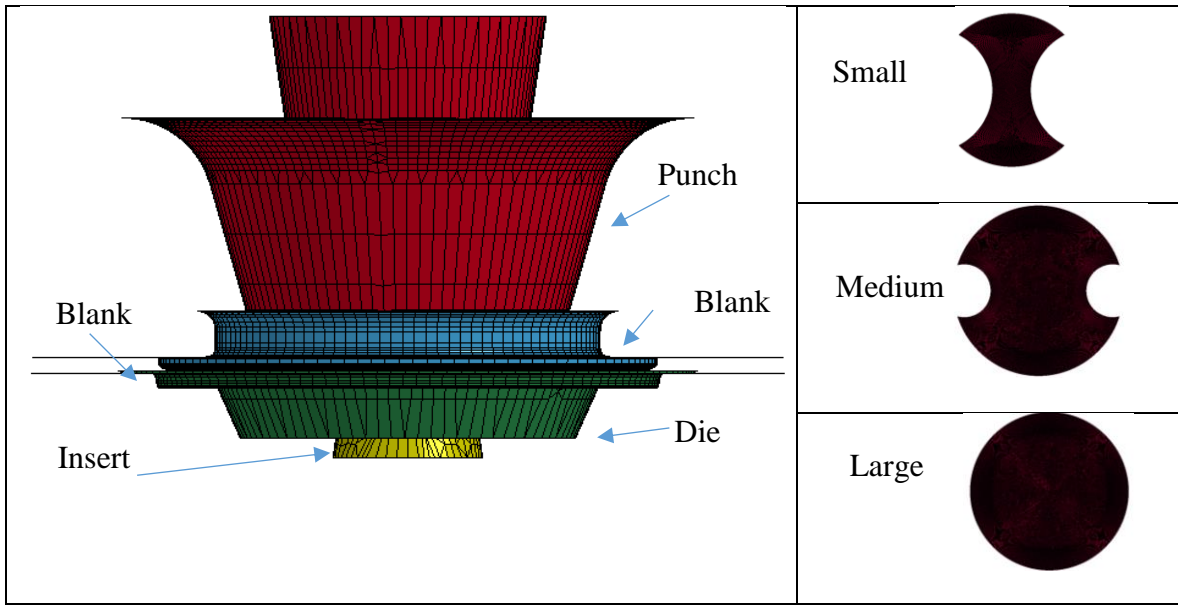


Figure 4.8 Simulation model for Numisheet 2014 BM1

4.6.2 FEM modeling

The draw process is modeled by using LS-PrePost(R) V4.3 as shown in Figure 4.8. The punch, die, binder and inserts are treated as rigid bodies and modeled by shell elements with mesh size ranging from 0.5mm to 10mm, which ensure more than eight elements distributed over radius areas. Sheet blanks are modelled by Belytschko-Tsay shell elements (Triangular and Quadrangle mixed) with an average size of 1mm. Material model 37 (MAT37) in LS-DYNA, which uses normal anisotropic Hill-48 yield function, is selected to describe the elastic-viscoplastic behavior of the sheet material. Table 4.7 gives the material properties of the sheet material TRIP780. The flow stress is described by using Swift law, in which the material constants n , k , and $\bar{\epsilon}_0$ are average values from tensile tests conducted at seven different angles distributed evenly from the rolling direction to the transverse direction to represent all in-plane directions (Tang and Pan 2007). As suggested by Wu (2013), a low constant Coulomb friction coefficient of 0.02 is chosen for the low

friction at the interfaces of punch/blank and insert/blank while a high constant Coulomb friction of 0.2 is chosen for the interfaces of binder/blank and die/blank. LS-DYNA explicit solver is used to solve the forming process as a quasi-static problem. The die is set stationary while the punch and binder are allowed to travel in the vertical direction at a speed of 0.085 mm/s. Binder holder force is set at 509KN as suggested by (Wu 2013). Increased punch speed (10mm/s) and mass scaling (1400%) is selected to reduce the computation cost while the kinematic energy is kept below 1% of internal energy.

The limit strain under uniaxial tension from the Nakajima test shown in Figure 4.3g is used to calibrate the criterion. From measured data point at LN, the major limit strain $\varepsilon_1''(t, \rho_{\min})$ at the minimum strain ratio -0.394 is measured at 0.33. Using this value and an initial sheet thickness 1.05mm, Eq.(4.13) is calibrated. The effect function determined in section 4.3.3 is used in the calculation.

Table 4.7 Material properties of 1.05mm thick TRIP780

| Friction coefficients | | Flow stress (MPa) | Young's modulus (MPa) | r |
|-------------------------|---------------------------|--|-----------------------|-------|
| Binder/blank, Die/blank | Punch/blank, Insert/blank | | | |
| 0.2 | 0.02 | $\sigma = 1554(\bar{\varepsilon}_0 + 0.012)^{0.292}$ | 200000 | 0.848 |

4.6.3 Results and discussion

To validate the simulation model, the predicted punch load trajectories at six different test setups are compared with the experimental measurements as shown in Figure 4.9. Comparison shows that prediction matches quite well with the measurements and the largest deviation is less than 5%. The observed oscillations of predicted punch loads can be due to the nature of dynamic effect and switching of contact conditions during the

dynamic explicit simulation. As shown in Figure 4.10, the LN elements are reported when the accumulated damage value exceeds unity as defined by Eq.(4.13).

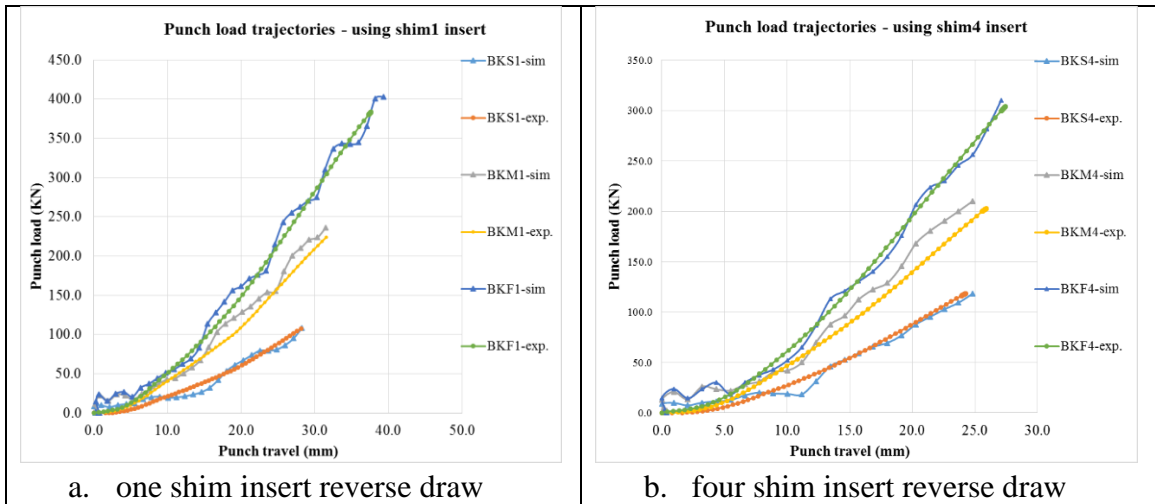


Figure 4.9 Comparison of Punch load trajectories from simulation prediction and experimental measurement

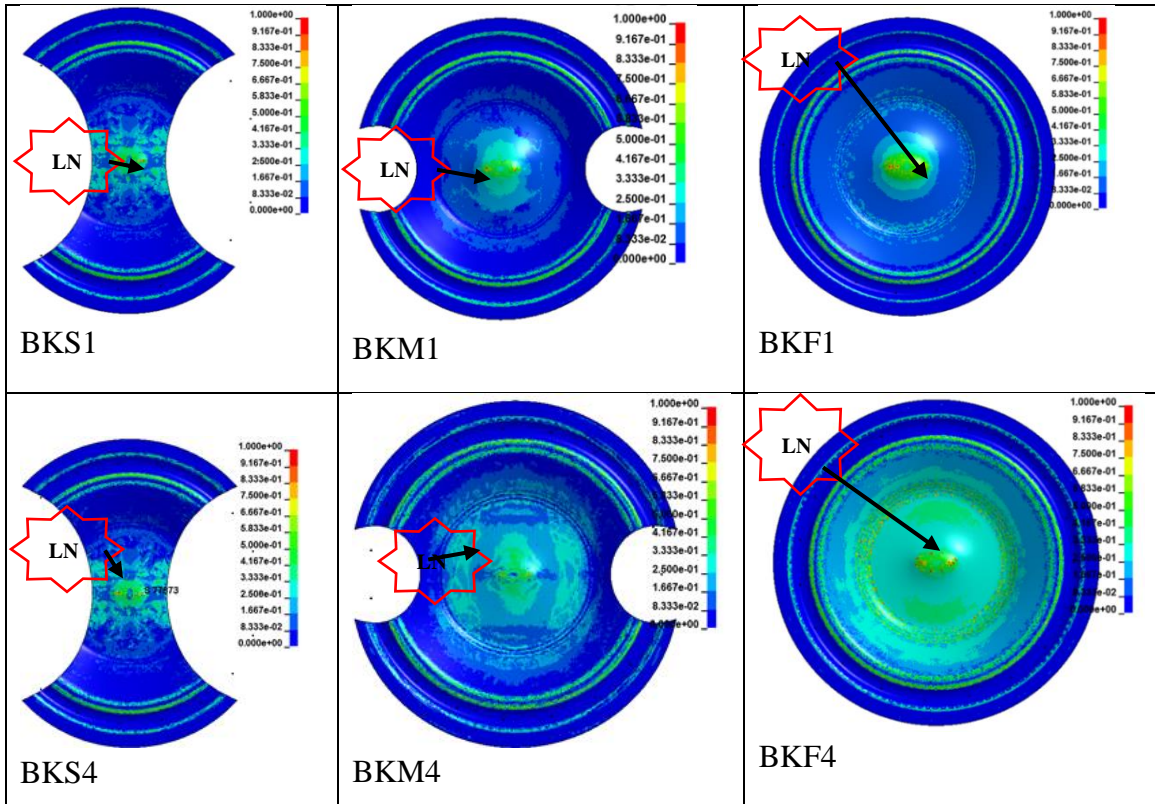


Figure 4.10 Damage distribution at moment of LN initiation and identified location of LN

Non-linear strain paths of the elements at LN initiation are plotted against experimental measurements as shown in Figure 4.11. The predicted strain paths generally match the non-linear patterns from the measurement. Relatively large deviations can be observed in the cases of BKF1, BKS4, and BKM4. The increased deviations can be due to the dynamic effect during numerical calculation and the assumed constant friction coefficients in this study. In reality the friction is a function of many factors, such as pressure, sliding interfacial speed and surface roughness, etc. (Sheng 2010).

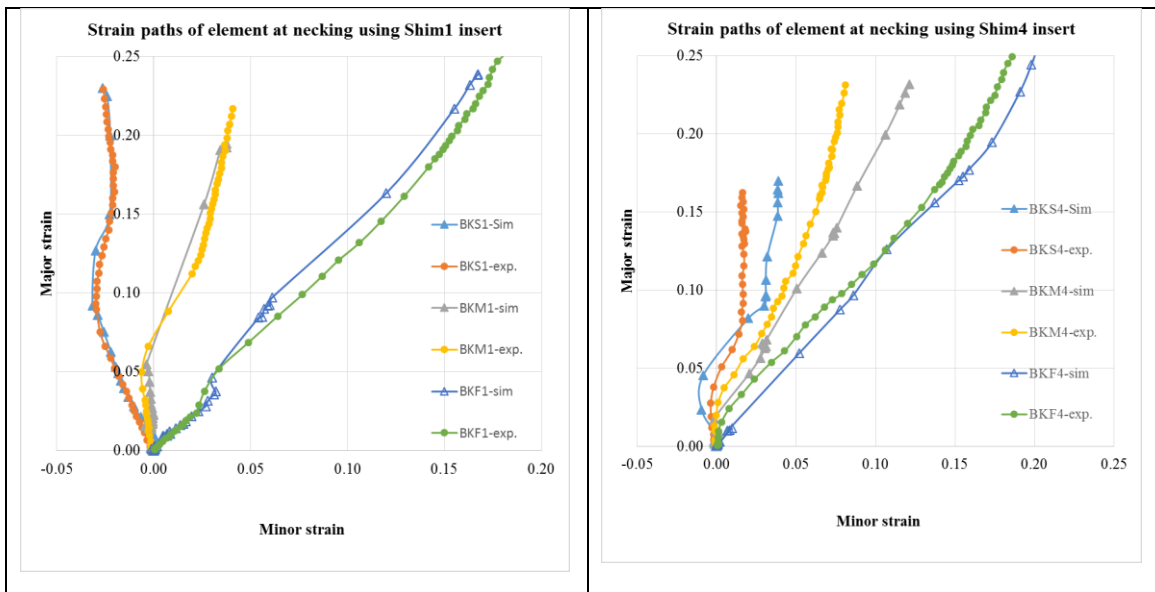
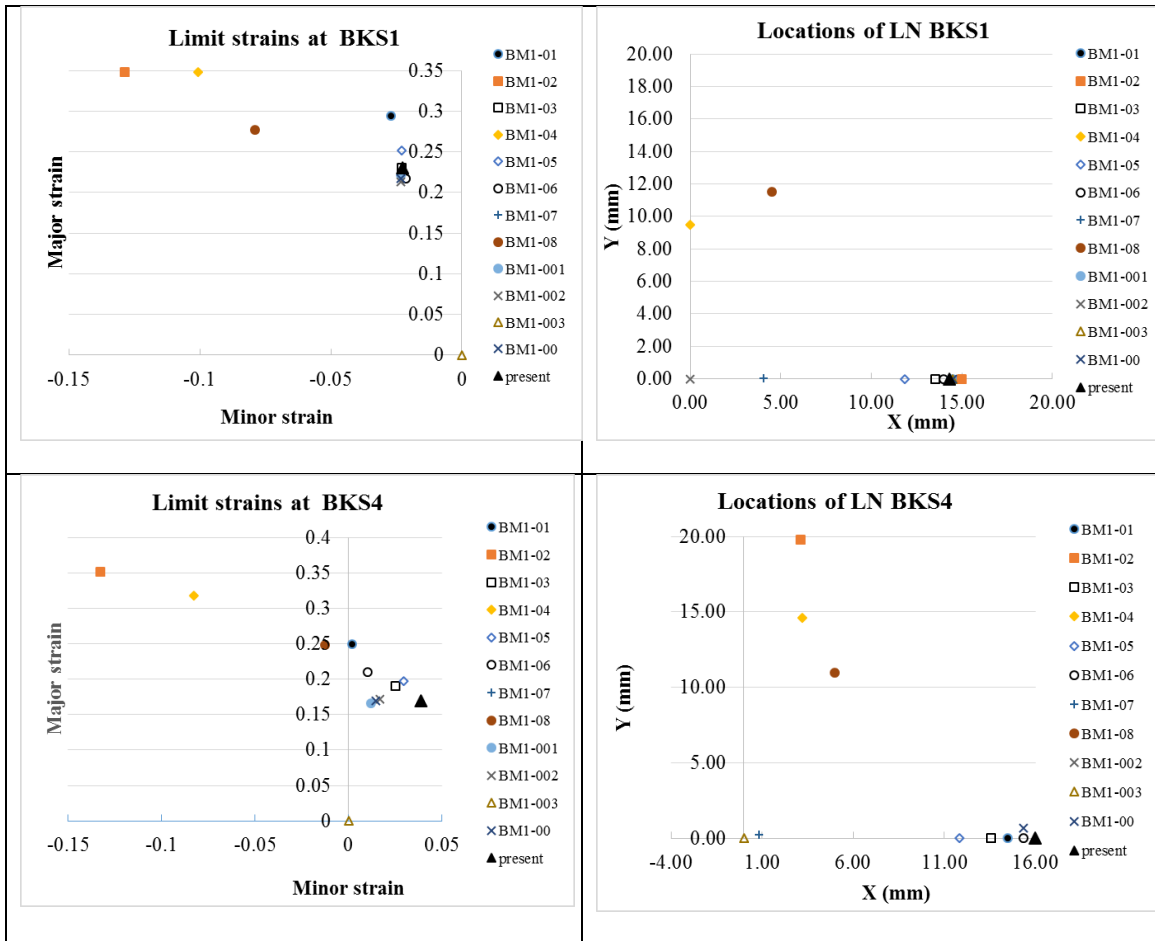
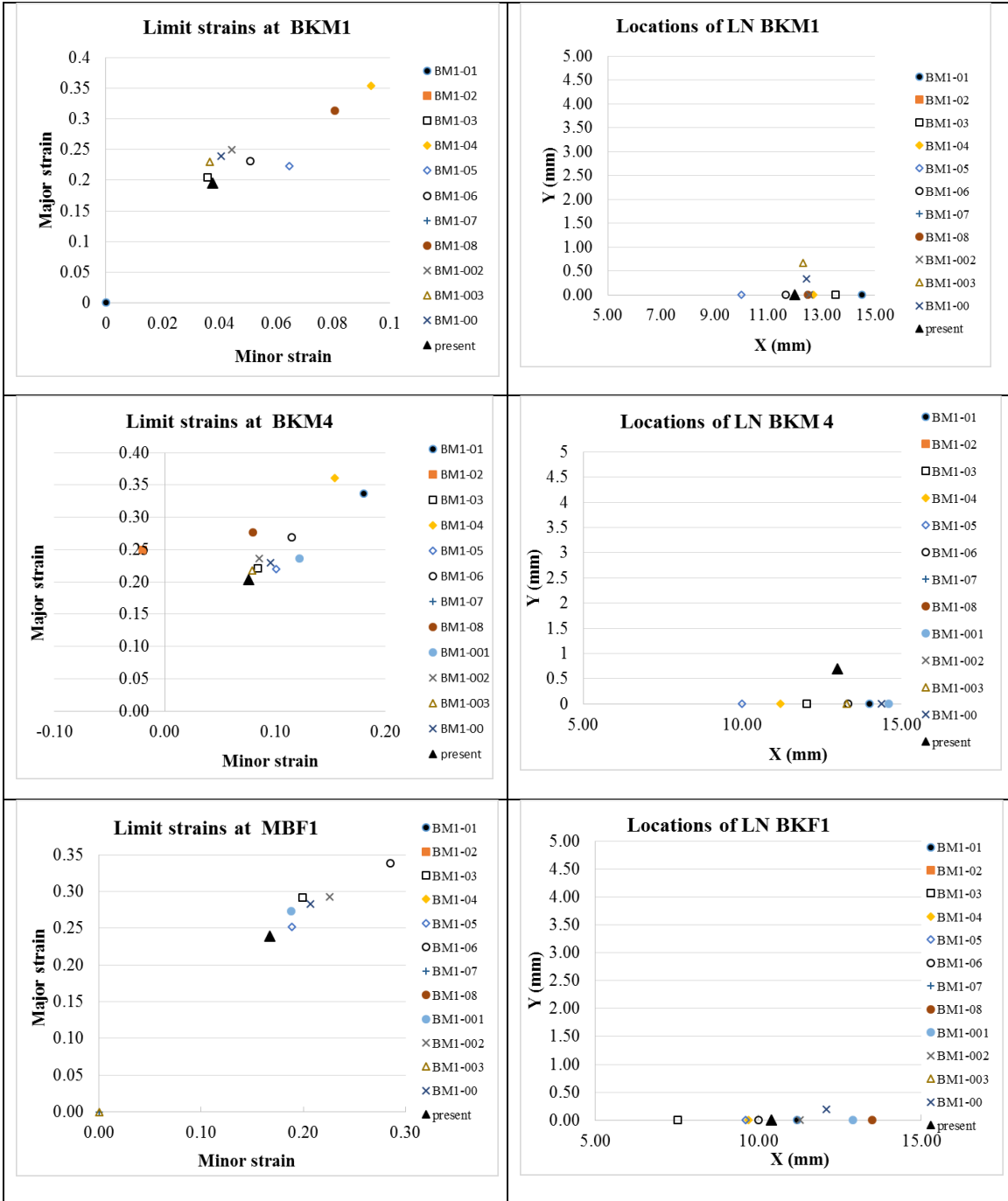


Figure 4.11 Strain paths of the element at LN from simulation prediction and experimental measurement

Figure 4.12 gives the limit strains (major strain and minor strain) at top sheet surface and its locations from simulation predictions by using different approaches and experimental measurement. Comparison shows that the discrepancies between predictions by using present approach and experimental measurements are quite small in true strain, which ranges from 0.009 in the case of small size blank with using 1 shim insert in draw (BKS1) to 0.04 in the case of full size blank with using 4 shim insert in draw (BKF4).

Comparison also shows that the predicted locations of the elements of LN initiation are close to the experimental observations. The distances between predicted locations of LN initiations and experimental observations varies from 0.07mm in the cases of BKS1 to 0.8mm in the case of BKF1. Compared with other submissions, the predictions from present algorithm are comparable to the submissions from BM1-3, BM1-5 and BM1-6, which match very well with experimental observation.





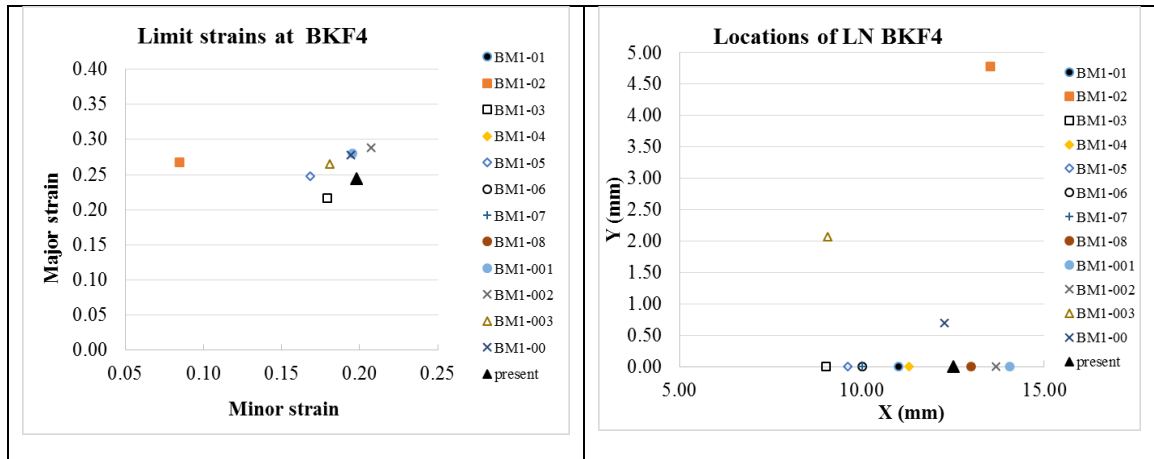


Figure 4.12 Comparison of limit strains and initial locations at LN from calculations and experiment (Note: the location is measured from the center of the sample)

4.7 Conclusions and discussion

In this study, a new ductile failure criterion is proposed to predict sheet metal forming limit in plane stress condition. The proposed criterion treats LN or fracture without LN as failure to avoid the uncertainty caused by the P-N deformation. Micromechanically observed strain path and initial sheet thickness effect on the critical damage is reflected by introducing an effect function. Under an assumption of proportional loading and normal anisotropic yield condition, the effect function is derived in an explicit form of ratio between major limit strains at different strain paths and initial sheet thickness. The material constants of effect functions can be determined by a set of critical forming limit test on certain class of sheet material.

The approach is validated by: 1) calculating FLCs under proportional strain path for eight different sheet materials, which include four experimental data from Numisheet 2008 & 2014 benchmark tests; 2) calculating FLC under several bilinear strain paths for a steel sheet material; 3) predicting limit strains at LN and their locations in FEM simulations on a set of Numisheet 2014 benchmark reverse draws. The prediction matches quite well with

experimental observations. In the cases of benchmark studies, the predictions by using present algorithm are comparable with the best results from benchmark participants.

While most FLCs predicted by present criterion match quite well with experimental observation, comparison also show that slight large deviations were observed on the thinner gauge IF steel and thicker gauge TRIP steel. The increased discrepancy shall not surprise us, since such discrepancy can be explained by the difference of microstructure and corresponding strengthening mechanism between the target sheet materials (IF and TRIP) and sheet material (AK steel) used for determining the effect functions. In future work, as suggested in section 4.3, the effect functions can be determined for each class of sheet materials by conducting critical forming limit tests on a set of representative sheet materials, which are from same grade but different in thicknesses.

The instability under stretching condition is quite complex, many issues, such as fracture at lower stress triaxiality (Li et al. 2010), normal contact pressure effect on LN and fracture (Smith et al. 2003) and forming limit at trimmed edge (Ilinich et al. 2011), are still under investigation. Those aspects can be considered in future work.

Normal anisotropic Hill'48 yield function is used in this study to arrive at a concise representation of solution. Although in-plane non-quadratic yield criterion provided a better agreement with the yield data for the aluminum alloys with anisotropy (r) less than unity (Logan and Hosford 1980), Uppaluri et al. (2012) also pointed out that Logan and Hosford yield function in quadratic form gave a better result on prediction limit strains. In future work, the effect of different yield functions can be further investigated.

Finally, the merits and limitation of this criterion are summarized:

Merits:

- Removing the uncertainty of P-N deformation and reflecting the micromechanical findings on critical damage.
- Reduced effort on calibration. Once the effect function is determined by a set of critical test, the efforts of calibration for a target sheet material can be greatly reduced, as the calibration can be done by using data from uniaxial tension test.
- There is no dependence on stress-strain hardening relation. This has big advantage in that the forming limit criterion might be extendable to material modeling in which the stress-strain relation is not monotonic, i.e. in sheet forming at elevated temperatures.
- There is no significant path dependence. This is important for the forming processes with strong non-linear strain paths.

Limitation:

- The effect functions are phenomenologically determined by a set of critical forming limit test on certain type of sheet material. The application of the effect functions is limited to the same class of sheet materials otherwise the accuracy can be compromised.

4.8 References:

- Aretz, H., Keller, S., Engler, O., & Brinkman, H. J. 2014. A simple ductile failure model with application to AA5182 aluminium sheet forming. *International journal of material forming*, 7(3), 289-304.
- Arrieux, R. 1995. Determination and use of the forming limit stress diagrams in sheet metal forming. *Journal of Materials Processing Technology*, 53(1), 47-56.
- Atkins, A. G. 1996. Fracture in forming. *Journal of materials processing technology*, 56(1), pp. 609-618.

- Bai, Y., & Wierzbicki, T. 2008. Forming severity concept for predicting sheet necking under complex loading histories. *International Journal of Mechanical Sciences*, 50(6), 1012-1022.
- Bai, Y., & Wierzbicki, T. 2010. Application of extended Mohr–Coulomb criterion to ductile fracture. *International Journal of Fracture*, 161(1), 1-20.
- Banabic, D. 2010, Sheet metal Forming Processes: Constitutive Modeling and Numerical Simulation, Springer, Heidelberg, Germany. ISBN:978-3-540-88207-7
- Benzerga, A. A., Besson, J., & Pineau, A. 1999. Coalescence–Controlled Anisotropic Ductile Fracture. *Journal of Engineering Materials and Technology*, 121, 221–229.
- Benzerga, A., & Leblond, J. B. 2010. Ductile fracture by void growth to coalescence. *Advances in Applied Mechanics*, 44, 169-305.
- Bleck, W., Deng, Z., Papamantellos, K., & Gusek, C. O. 1998. A comparative study of the forming-limit diagram models for sheet steels. *Journal of Materials Processing Technology*, 83(1), 223-230.
- Brozzo, P., Deluca, B., & Rendina, R. 1972. A new method for the prediction of formability limits in metal sheets. In Proc. 7th biennial Conf. IDDR.
- Bruschi, S., Altan, T., Banabic, D., Bariani, P. F., Brosius, A., Cao, J., & Tekkaya, A. E. 2014. Testing and modelling of material behaviour and formability in sheet metal forming. *CIRP Annals-Manufacturing Technology*, 63(2), 727-749.
- Chen, J., Zhou, X., & Chen, J. 2010. Sheet metal forming limit prediction based on plastic deformation energy. *Journal of Materials Processing Technology*, 210(2), 315-322.
- Chow, C. L., & Jie, M. 2004. Forming limits of Al 6022 sheets with material damage consideration—theory and experimental validation. *International journal of mechanical sciences*, 46(1), p.99-122.
- Chow, C. L., Jie, M., & Wu, X. 2007. A damage-coupled criterion of localized necking based on acoustic tensor. *International Journal of Damage Mechanics*.
- Chung, K., Kim, H., & Lee, C. 2014. Forming limit criterion for ductile anisotropic sheets as a material property and its deformation path insensitivity. Part I: Deformation path insensitive formula based on theoretical models. *International Journal of Plasticity*, 58, 3-34.
- Cockcroft, M. G., & Latham, D. J. 1968. Ductility and the workability of metals. *J Inst Metals*, 96(1), 33-39.
- Considère M 1885. L’emploi du fer et Lacier Dans Les Constructions. *Annales Des Ponts et Chaussées* 9:574–775
- Dick, R. E., Yoon, J. W., & Stoughton, T. B. 2015. Path-independent forming limit models for multi-stage forming processes. *International Journal of Material Forming*, 1-11.
- Gaber, C., Jocham, D., Weiss, H. A., Böttcher, O., & Volk, W. 2016. Evaluation of non-linear strain paths using Generalized Forming Limit Concept and a modification of the Time Dependent Evaluation Method. *International Journal of Material Forming*, 1-7.
- Gese, H., & Dell, H. 2006. Numerical Prediction of FLC with the Program CRACH. *Proceedings of FLC Zurich 2006*.
- Gese, H., Dell, H., Oberhofer, G., Oehm., M. , Heath, A., 2013, CRACHFEM – A comprehensive approach for the prediction of sheet failure in multi-step forming and subsequent forming and crash simulations, Forming Technology Forum 2013, September 19-20, 2013, utg, TUM, Germany

- Ghosh AK, Laukonis JV. 1976. The influence of strain-path changes on the formability of sheet steel. 9th Biennial Congress of the International Deep Drawing Research Group, Sheet Metal Forming and Energy Conservation, ASM Publication.
- Goodwin G. 1968. Application of strain analysis to sheet metal forming in the press shop. SAE paper, No. 680093, 1968.
- Graf AF, Hosford WF. 1993. Effect of changing strain paths on forming limit diagrams of Al 2008-T4, Calculations of forming limit diagram for changing strain paths. *Metallurgical Transactions A* 1993;24A: 2503-2512.
- Gurson, A. L. 1977. Continuum Theory of Ductile Rupture by Void Nucleation and Growth: Part I – Yield Criteria and Flow Rules for Porous Ductile Media. *Journal of Engineering Materials and Technology*, 99, 2–15
- Han, H. N., & Kim, K. H. 2003. A ductile fracture criterion in sheet metal forming process. *Journal of Materials Processing Technology*, 142(1), 231-238.
- Hill, R. T. 1952. On discontinuous plastic states, with special reference to localized necking in thin sheets. *Journal of the Mechanics and Physics of Solids*, 1(1), 19-30.
- Hill, R. 1962. Acceleration Waves in Solids, *Journal of Mechanics and Physics of Solids*, 10:1–16.
- Hill, R. 2001. On the mechanics of localized necking in anisotropic sheet metals. *Journal of the Mechanics and Physics of Solids*, 49(9), 2055-2070.
- Hora, P., & Tong, L. 1994, May. Prediction methods for ductile sheet metal failure using FE-simulation. In *Proc. of the IDDRG Congress. Lisbon* (pp. 363-375).
- Hora, P., Tong, L., & Berisha, B. 2013. Modified maximum force criterion, a model for the theoretical prediction of forming limit curves. *International journal of material forming*, 6(2), 267-279.
- Hosford, W.F. and Caddell, R.M. 1993. *Metal Forming: Mechanics and Metallurgy*, Prentice
- Isik, K., Silva, M. B., Tekkaya, A. E., & Martins, P. A. F. 2014. Formability limits by fracture in sheet metal forming. *Journal of Materials Processing Technology*, 214(8), 1557-1565.
- ISO Copyright office, 2008. *Metallic Materials-Sheet and strip-determination of forming limit curves- Part 2: Determination of forming – limit curves in the laboratory*, ISO/DIS 12004-2, 2008
- Jalinier, J. M., & Schmitt, J. H. 1982. Damage in sheet metal forming—II. Plastic instability. *Acta Metallurgica*, 30(9), 1799-1809.
- Jain, M., Allin, J., & Lloyd, D. J. 1999. Fracture limit prediction using ductile fracture criteria for forming of an automotive aluminum sheet. *International Journal of Mechanical Sciences*, 41(10), 1273-1288.
- Keeler SP, Backhofen WA. 1964. Plastic instability and fracture in sheet stretched over rigid punches. *ASM Transactions Quarterly* 56:pp.25-48.
- Keeler, S.P., Brazier, S.G., 1977. Relationship between laboratory material characterization and press-shop formability. In: *Proceedings of Microalloying*, vol. 75, New York, pp. 517–530
- Li, Y., Luo, M., Gerlach, J., & Wierzbicki, T. 2010. Prediction of shear-induced fracture in sheet metal forming. *Journal of Materials Processing Technology*, 210(14), 1858-1869.
- Li, H., Chen, X., Xie, X., Xu, N., & Yang, L. 2013. Benchmark 1–Nonlinear Strain Path Forming Limit of a Reverse Draw. In *AIP Conf. Proc* (Vol. 1567, pp. 27-38).

- Liang B.W., Hu X.G. 1987. Sheet metal forming plasticity theory, Mechanical Industry Publication (in Chinese)
- Ilinich, A., Smith, L., & Golovashchenko, S. 2011. *Analysis of Methods for Determining Sheared Edge Formability* (No. 2011-01-1062). SAE Technical Paper.
- Leppin, C., Li, J., & Daniel, D. 2008. Application of a method to correct the effect of non-proportional strain paths on Nakajima test based forming limit curves. In *Proc. of the NUMISHEET 2008 Conf., Interlaken, Switzerland* (pp. 217-221).
- Logan, R. W., & Hosford, W. F. 1980. Upper-bound anisotropic yield locus calculations assuming $\langle 111 \rangle$ -pencil glide. *International Journal of Mechanical Sciences*, 22(7), 419-430.
- Lou, Y., Huh, H., Lim, S., & Pack, K. 2012. New ductile fracture criterion for prediction of fracture forming limit diagrams of sheet metals. *International Journal of Solids and Structures*, 49(25), 3605-3615.
- Ma, X., Li, F., Li, J., Wang, Q., Yuan, Z., & Fang, Y. 2015. Analysis of forming limits based on a new ductile damage criterion in St14 steel sheets. *Materials & Design*, 68, 134-145.
- Mattiasson, K., Jergues, J., & Dubois, P. 2013. Models for strain path independent necking prediction in LS-DYNA. In *Proceedings of the 9th European LS-DYNA users' conference*
- McClintock, F. A. 1968. A criterion for ductile fracture by the growth of holes. *Journal of applied mechanics*, 35(2), 363-371.
- Oyane, M. 1972. Criteria of ductile fracture strain. *Bulletin of JSME*, 15(90), 1507-1513.
- Ozturk, F., & Lee, D. 2007. A new methodology for ductile fracture criteria to predict the forming limits. *Journal of Materials Engineering and Performance*, 16(2), 224-228.
- Perrin, G. 1992. Contribution à l'étude théorique et numérique de la rupture ductile des métaux. Ph.D. thesis, Ecole Polytechnique.
- Rice, J. R., & Tracey, D. M. 1969. On the ductile enlargement of voids in triaxial stress fields*. *Journal of the Mechanics and Physics of Solids*, 17(3), 201-217.
- Schmitt, J. H., & Jalinier, J. M. 1982. Damage in sheet metal forming—I. Physical behavior. *Acta Metallurgica*, 30(9), 1789-1798.
- Sheng, Z. Q. 2008. Formability of tailor-welded strips and progressive forming test. *Journal of materials processing technology*, 205(1), 81-88.
- Sheng, Z. Q. 2010. Micro-Texture Tailored Friction Modeling and Discrete Application in Drawability Improvement (No. 2010-01-0982). SAE Technical Paper.
- Sigvant, M., Mattiasson, K., Larsson, M. 2008, The definition of incipient necking and its impact on experimentally or theoretically determined forming limit curves. IDDRG2008 proceedings
- Smith, L. M., Averill, R. C., Lucas, J. P., Stoughton, T. B., & Matin, P. H., 2003. Influence of transverse normal stress on sheet metal formability. *International Journal of Plasticity*, 19(10), 1567-1583.
- Stören, S., & Rice, J. R., 1975. Localized necking in thin sheets. *Journal of the Mechanics and Physics of Solids*, 23(6), 421-441.
- Stoughton, T. B., 2000. A general forming limit criterion for sheet metal forming. *International Journal of Mechanical Sciences*, 42(1), 1-27.
- Stoughton, T. B., & Zhu, X., 2004. Review of theoretical models of the strain-based FLD and their relevance to the stress-based FLD. *International Journal of Plasticity*, 20(8), 1463-1486.

- Stoughton, T. B., & Yoon, J. W., 2012. Path independent forming limits in strain and stress spaces. *International Journal of Solids and Structures*, 49(25), 3616-3625.
- Stoughton, T. B., Shi, M. F., Huang, G., & Yoon, J. W., 2013. Material characterizations for Benchmark 1 and Benchmark 2. In *NUMISHEET 2014: The 9th International Conference and Workshop on Numerical Simulation of 3D Sheet Metal Forming Processes: Part A Benchmark Problems and Results and Part B General Papers* (Vol. 1567, No. 1, pp. 9-14). AIP Publishing.
- Strano, M., & Colosimo, B. M., 2006. Logistic regression analysis for experimental determination of forming limit diagrams. *International Journal of Machine Tools and Manufacture*, 46(6), 673-682.
- Tang, S.C. and Pan, J., 2007. *Mechanics modeling of sheet metal forming*. SAE International.
- Tasan, C. C., Hoefnagels, J. P. M., Ten Horn, C. H. L. J., & Geers, M. G. D., 2009. Experimental analysis of strain path dependent ductile damage mechanics and forming limits. *Mechanics of Materials*, 41(11), 1264-1276.
- Takuda, H., Mori, K., Fujimoto, H., & Hatta, N., 1999. Prediction of forming limit in bore-expanding of sheet metals using ductile fracture criterion. *Journal of Materials Processing Technology*, 92, 433-438.
- Takuda, H., Mori, K., Takakura, N., & Yamaguchi, K., 2000. Finite element analysis of limit strains in biaxial stretching of sheet metals allowing for ductile fracture. *International Journal of Mechanical Sciences*, 42(4), 785-798.
- Uppaluri, R., Reddy, N. V., & Dixit, P. M., 2011. An analytical approach for the prediction of forming limit curves subjected to combined strain paths. *International Journal of Mechanical Sciences*, 53(5), 365-373.
- Volk, W., Illig, R., Kupfer, H., Wahlen, A., Hora, P., Kessler, L., & Hotz, W., 2008. Benchmark 1–Virtual forming limit curves. *Hora, P. et al (eds.): The Numisheet 2008*.
- Volk, W., Hoffmann, H., Suh, J., & Kim, J., 2012. Failure prediction for nonlinear strain paths in sheet metal forming. *CIRP Annals-Manufacturing Technology*, 61(1), 259-262.
- Wang, K., Carsley, J. E., He, B., Li, J., & Zhang, L., 2014. Measuring forming limit strains with digital image correlation analysis. *Journal of Materials Processing Technology*, 214(5), 1120-1130.
- Werber, A., Liewald, M., Nester, W., Grünbaum, M., Wiegand, K., Simon, J., & Hotz, W., 2014. Development of a new failure prediction criterion in sheet metal forming. *International Journal of Material Forming*, 7(4), 395-403.
- Wu, X., 2013. Benchmark 1-Nonlinear strain path forming limit of a reverse draw: Part C: Benchmark analysis. In *NUMISHEET 2014: Part A Benchmark Problems and Results* (Vol. 1567, No. 1, pp. 39-176). AIP Publishing.
- Yao, H., & Cao, J., 2002. Prediction of forming limit curves using an anisotropic yield function with prestrain induced backstress. *International journal of plasticity*, 18(8), 1013-1038.
- Yoshida, K., Kuwabara, T., & Kuroda, M., 2007. Path-dependence of the forming limit stresses in a sheet metal. *International Journal of Plasticity*, 23(3), 361-384.
- Zeng, D., Chappuis, L., Xia, Z. C., & Zhu, X., 2009. A path independent forming limit criterion for sheet metal forming simulations. *SAE International Journal of Materials & Manufacturing*, 1(1), 809-817.

CHAPTER 5: Predicting Forming Limit of Aluminum Alloys at Elevated Temperatures by Using an Improved Ductile Failure Criterion

5.1 Introduction

Due to their high strength-weight ratio and good corrosion resistance, aluminum alloy sheet materials are attractive alternatives to make lightweight automotive body panels and structures (Mallick 2010). However, compared with conventionally used mild steel sheet materials, the formability of aluminum alloy sheet materials at room temperature is much inferior, i.e. two-thirds of drawing quality steel (Li and Ghosh 2003). Significant enhancement can be achieved at warm forming temperatures ranging from 200°C to 350°C by activating additional sliding systems and reducing defect growth by recovery (Neugebauer et al. 2006). To take advantage of the improved formability, recent years have witnessed increased interests in warm forming aluminum sheet materials (Tebbe and Kridli 2004). Nevertheless, since the recovery process is rate-sensitive, the formability of aluminum sheet materials is sensitive to the strain rate and such sensitivity increases with the increase in temperature. In warm forming, the stretching failure of aluminum sheet materials can be due to ductile fracture mechanism (Ashby et al. 1979). To predict the stretching failure, which occurs by either localized necking (LN) or fracture without LN, strain-based Forming Limit Curves (FLCs) are widely used by industry and academia. FLCs at elevated temperatures can be measured by conducting Nakajima dome tests (Abu-

Farha 2011), Machiniak tests (Naka et al. 2001) or box forming test (Li and Ghosh 2004). Regardless of the different test methods, the levels of measured FLCs increase with increase in temperature and/or decrease in strain rate. However, in the warm forming processes, especially in non-isothermal conditions, spatially and temporally different distributions of temperature and strain rate can be created on a workpiece due to transient heat transformation and tool movement (Lin et al. 2014). Thus, the prediction of stretching failure in such situations require a complete representation of forming limit that is governed by both strain rate and temperature. Three-dimensional forming limit diagrams with either temperature (Kröhn et al. 2007) or strain rate (Abu-Farha 2011) as the third axis have been proposed. A three-dimensional forming limit surface that takes into account both temperature and strain rate was proposed by Sheng (2012). In this concept, the Zener-Hollomon parameter (Z), or the so-called temperature-compensated strain rate (Zener and Hollomon 1944), is used to represent the effects of strain rate and temperature on the forming limit.

Due to the difficulty of achieving and/or maintaining the required test conditions, such as temperature, strain rate, and failure mode (Hsu et al. 2008), the tests of obtaining FLCs at elevated temperatures are costly and time consuming. Among many strategies (Stoughton and Zhu 2004, Banabic 2010, Bruschi et al. 2014), M-K theory was widely used to predict FLCs. Several representative studies include predicting FLCs of Al5083-O by Naka et al.(2001), Al2008-T4 and Al6111-T4 by Yao and Cao (2002), Al 3003-H111 by Abedrabbo et al. (2006), AC300 by Gese and Dell et al. (2006), and Al 5086 by Chu et al. (2016). Studies have also pointed out that the results of M-K methods strongly depend

on the selection of yield function, constitution law (Bruschi et al. 2014) and initial imperfection (Graf and Hosford 1990).

Primarily due to their straightforward implementation into finite element code as well as their intrinsic easiness in calibration, ductile fracture criteria are another type of strategy widely used to predict fracture FLCs. Based on Oyane's criterion, Alexandrov et al. (2005) proposed a fracture criterion for hot metal forming aluminum alloys, in which Zener-Hollomon parameter was used to represent both strain rate and temperature effect. Such criterion was analytically demonstrated to predict failure in a cup draw process. Jie et al. (2011) proposed an isotropic damage-coupled FLD for warm forming Al6061 at a temperature of 450°C. Lin et al. (2014) developed a plane-stress continuum damage model for prediction of FLCs of aluminum sheet material Al5574 at elevated temperatures. The model has 21 material constants to be calibrated and was validated by using the test data from (Li and Ghosh 2004). Based on Lemaitre's damage model, Hu et al. (2015) proposed a ductile damage model coupled with FEM simulation for predicting failure in hot stamping boron steel 22MnB5. Seven material constants are needed to be calibrated in this model.

In this Chapter, the DFC proposed in the Chapter 4 is further developed by using the improved Zener-Hollomon parameter Z' , which was proposed in Chapter 3, to predict forming limit of aluminum alloy sheet materials at elevated temperatures.

With the introduction of Zener-Hollomon parameter Z' , the effect function in the proposed DFC is improved to include strain rate and temperature effect on the critical damage. The developed DFC is used to predict FLCs for sheet material Al5083 in warm forming condition and failure in rectangular cup warm forming process on Al 5182+Mn sheet material.

5.2 Effect function at elevated temperatures

As discussed in Chapter 4, the strain rate and initial sheet thickness effect on critical damage can be expressed by the ratio of limit strains at different strain paths as represented by Eq.(4.7). To reflect the temperature and strain rate effect on the critical damage, the effect function at elevated temperature (EFT) can be expressed as $F(t, \rho, \ln(Z'))$ and can be calculated as:

$$F(t, \rho, \ln(Z')) = \frac{(1 + \rho)\varepsilon_1^n(t, \rho, \ln(Z'))}{(1 + \rho'')\varepsilon_1^n(t, \rho'', \ln(Z'))} \quad (5.1)$$

where $\varepsilon_1^n(t, \rho, \ln(Z'))$ is the limit strain of a sheet material with initial thickness of t , current moment strain ratio of ρ , at certain strain rate and temperature condition, which can be represented by $\ln(Z')$. Using effect function $f(t, \rho)$ determined at room temperature as baseline, an adjusting function $adz(\rho, \ln(Z'))$ is introduced and $F(t, \rho, \ln(Z'))$ can be defined as:

$$F(t, \rho, \ln(Z')) = f(t, \rho)adz(\rho, \ln(Z')) \quad (5.2)$$

At room temperature, $adz(\rho, \ln(Z')) = 1$. At elevated temperatures, the adjusting function can be determined as:

$$adz(\rho, \ln(Z')) = \frac{F(t, \rho, \ln(Z'))}{f(t, \rho)} \quad (5.3)$$

In this study, the adjust function is determined at plane strain and equal biaxial tension. Then, the EFT at any other strain paths is interpolated by using H-SR formula as shown in Appendix B.

The forming limit data from Marciniak type test on 1mm thick JIS-A5083P-O sheet material at temperatures (25°C to 300°C) and strain rates (0.0001/s to 0.1/s) from (Naka et

al. 2001) is used to determine the EFT. Table 5.1 gives the chemical composition in weight percentage of the sheet material. Circles with diameter of 6.35mm are printed on specimen surface and are monitored by a CCD camera with video recording function. Strains are calculated and identified from the recording data.

Table 5.1 Chemical composition of JIS-A5083-P-O (wt.%) (Naka et al. 2001)

| Si | Fe | Cu | Mn | Mg | Cr | Zn | Ti |
|------|------|-------|------|------|------|-------|------|
| 0.04 | 0.04 | Trace | 0.64 | 4.58 | 0.11 | Trace | 0.01 |

Based on test data in (Naka et al. 2001), the values of $adz(0, \ln(Z'))$ and $adz(1, \ln(Z'))$ are plotted as shown in Figure 5.1. The data points show that $adz(0, \ln(Z'))$ varies at a narrow range around 1, which means the strain rate and temperature effect is not significant and thus it can be assumed as a constant of 1. In biaxial tension, $adz(\ln(Z'))$ increases with the increase of $\ln(Z')$ and can be approximated by a polynomial equation. Then, the adjust function at plane strain and equal biaxial tension can be expressed as:

$$adz(\rho, \ln(Z')) = \begin{cases} 1, & -\rho'' \leq \rho \leq 0 \\ -0.0003 \ln^2(Z') + 0.0292 \ln(Z') + 0.2272, & 0 < \rho \leq 1 \end{cases} \quad (5.4)$$

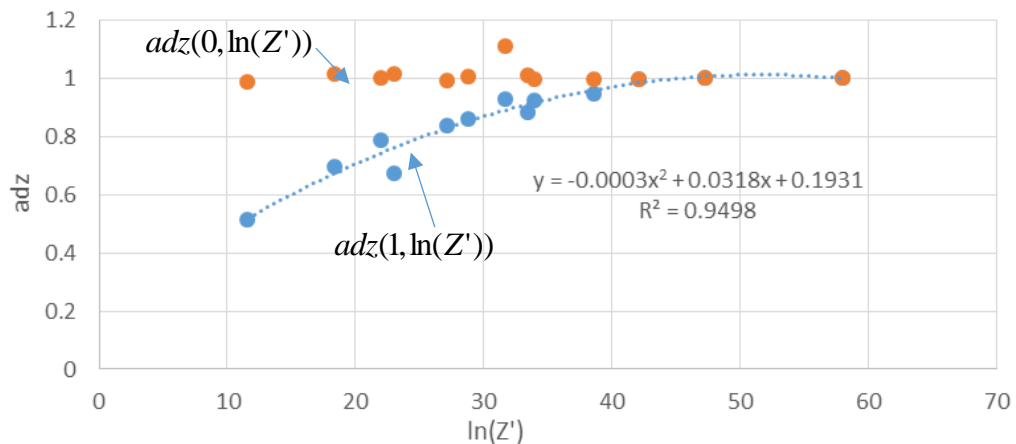


Figure 5.1 Plots of adjust function at two critical strain paths (data points in red are in plane strain while data points in blue are in equal biaxial tension)

5.3 Calculation of Forming Limit Curves

With the determined adjust function and effect function, the forming limit curves can be predicted by using the limit strain under uniaxial tension.

5.3.1 Procedure

Under different strain rates and temperatures, FLCs can be calculated by:

- 1) Measure limit major strain $\varepsilon_1^n(t, \rho^u, \ln(Z'))$ at a few representative temperatures and effective strain rates in uniaxial tension.

- 2) Calculate $F(t, 0, \ln(Z'))$ and $F(t, 1, \ln(Z'))$ using Eq.(5.2 & 5.4) as:

$$F(t, 0, \ln(Z')) = f(t, 0) \quad (5.5 \text{ a})$$

$$F(t, 1, \ln(Z')) = f(t, 1)(-0.0003 \ln^2(Z') + 0.0292 \ln(Z') + 0.2272) \quad (5.5 \text{ b})$$

- 3) Calculate the limit major strain in plane strain $\varepsilon_1^n(t, 0, \ln(Z'))$ and limit major strain at equal biaxial tension $\varepsilon_1^n(t, 1, \ln(Z'))$ using following equations:

$$\varepsilon_1^n(t, 0, \ln(Z')) = F(t, 0, \ln(Z')) \varepsilon_1^n(t, \rho^u, \ln(Z')) (1 + \rho^u) \quad (5.6a)$$

$$\varepsilon_1^n(t, 1, \ln(Z')) = \frac{F(t, 1, \ln(Z')) \varepsilon_1^n(t, \rho^u, \ln(Z')) (1 + \rho^u)}{2} \quad (5.6b)$$

- 4) Since the shape function of H-SR formula is assumed, from Eq.(5.10), the limit major strain at other strain paths in left hand quadrant and right hand quadrant can be calculated as:

$$\varepsilon_1^n(t, \rho, \ln Z') = \begin{cases} \varepsilon_1^n(t, 0, \ln(Z')) + \frac{\rho}{\rho^u} (\varepsilon_1^n(t, \rho^u, \ln(Z')) - \varepsilon_1^n(t, 0, \ln(Z'))), & (\rho^u \leq \rho \leq 0) \\ \varepsilon_1^n(t, 0, \ln(Z')) + (-0.414\rho^2 + 1.414\rho) (\varepsilon_1^n(t, 1, \ln(Z')) - \varepsilon_1^n(t, 0, \ln(Z'))), & (0 \leq \rho \leq 1) \end{cases} \quad (5.7)$$

For a sheet material of an initial thickness of t , Eq. (5.7) shows that the forming limit can be represented as a function of strain ratio ρ and $\ln(Z')$, which can construct a

3D surface with three axis of major strain, strain ratio and $\ln(Z')$. Obviously, the surface can be transformed to a space of $(\varepsilon_1, \varepsilon_2, \ln(Z'))$ as below:

$$\begin{bmatrix} \varepsilon_1^n(\varepsilon_2, \ln(Z')) \\ \varepsilon_2 \end{bmatrix}_{failure} = \begin{bmatrix} 1 \\ \rho \end{bmatrix} \varepsilon_1^n(\rho, \ln(Z')) \quad (5.8)$$

when s is taken at 1, above transformation explains the Z-FLS that has been phenomenologically constructed by Sheng (2012).

5.3.2 Calculation FLCs for 1.0mm thick JIS-A5083P-O

Following the procedure given above, FLCs of fine grain sheet material JIS-A5083P-O at different temperatures and strain rates are calculated. Figure 5.2 gives the calculated FLCs and experimental data published by Naka et al. (2001). In the calculation, isotropic deformation was suggested by Naka et al. (2001). Figure 5.2 shows that at five different temperatures and three different strain rates, the calculated FLCs match quite well with most measured data points. High deviations are only found at three measurements at strain paths in positive quadrant at temperature of 200°C and the low strain rate of 0.01/s and 0.0001/s, see Figure 5.2 d. For comparison, frequently used Oyane criterion was used to calculate FLCs at room temperature and temperature of 80°C as shown in Figure 5.2 a and b. The FLCs predicted by using the Oyane criterion monotonically slope down from the left hand quadrant to the right hand quadrant of FLD. Obviously, the calculated FLCs only match the measurement at left hand quadrant of FLD while increasing deviation can be found at right hand quadrant.

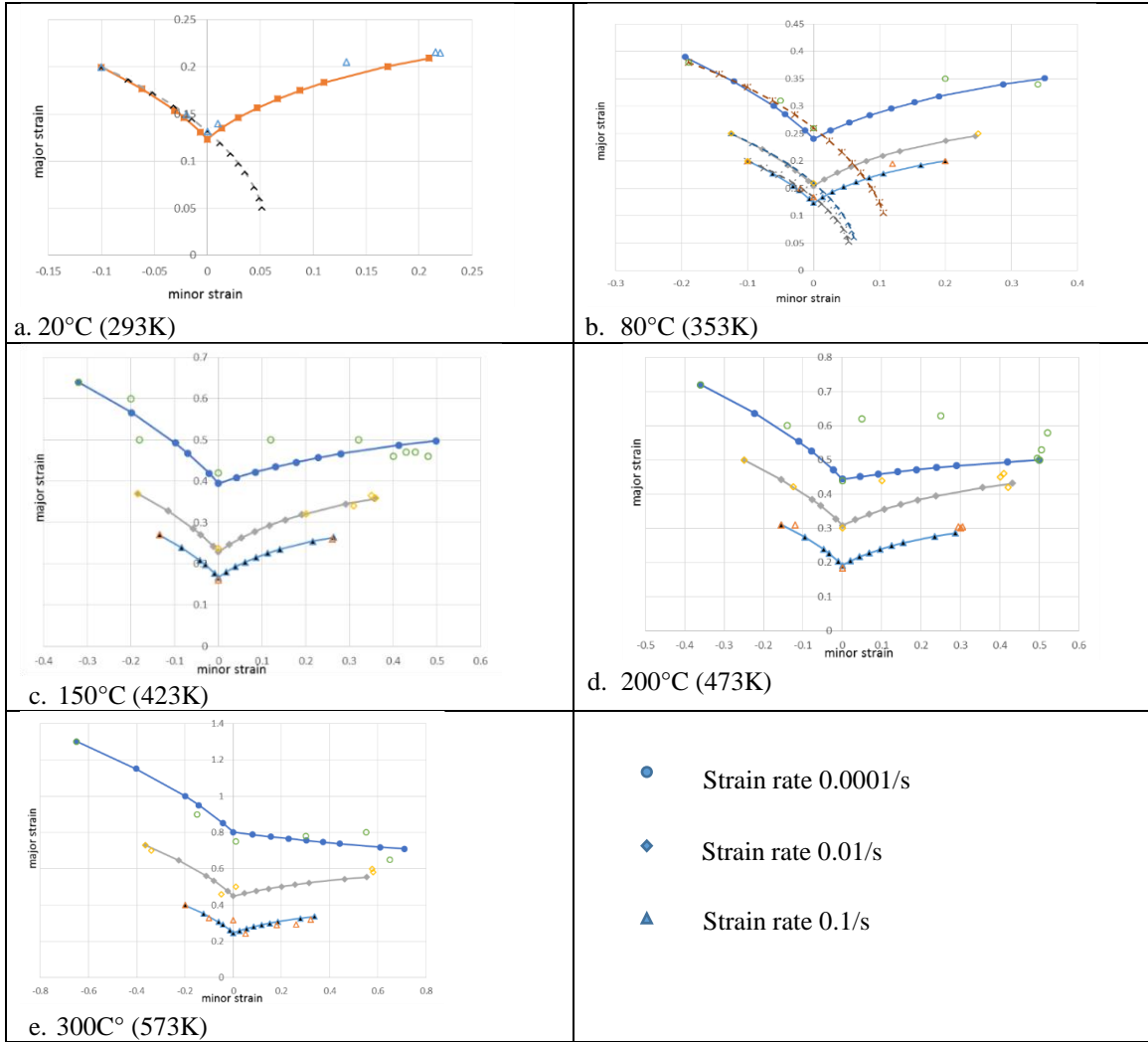


Figure 5.2 Calculated FLCs (solid markers and solid line) and data points (unfilled markers) from tests at different temperatures and strain rates for sheet material JIS-A5083P-O
 *Note: FLCs calculated by using Oyane criterion (cross markers and dash line)

5.4 Predicting failure in FEM simulation

Working with a FEM simulation, effect function $f(t, \rho)$ and limit major strain under uniaxial tension $\varepsilon_1^n(t, \rho^u)$ in Eq.(4.13) are replaced by Eq.(5.2) and Eq.(5.2), respectively. The damage growth of any element on a sheet material being deformed can be calculated as:

$$D = \frac{3}{\varepsilon_1^n(t, \rho^u, \ln(Z')) \langle F(t, \rho, \ln(Z')) \rangle} \int_0^{\bar{\varepsilon}^n} \eta d\bar{\varepsilon} \quad (5.9)$$

$$F(t, \rho, \ln(Z')) = \begin{cases} (1 + \rho) \left\{ f(t, 0) + \left[\frac{1}{1 + \rho^u} - f(t, 0) \right] \frac{\rho}{\rho^u} \right\}, & (\rho^u \leq \rho \leq 0) \\ (1 + \rho) adz(\rho, \ln(Z')) \left(f(t, 0) + (-0.414\rho^2 + 1.414\rho) \left(\frac{f(t, 1)}{2} - f(t, 0) \right) \right), & (0 \leq \rho \leq 1) \end{cases}$$

For a given sheet material of initial sheet thickness t , $\varepsilon_1^n(t, \rho^u, \ln(Z'))$, the limit major strain in uniaxial tension, can be represented by a function of $\ln(Z')$ as given by Eq.(3.2) as:

$$\varepsilon_1^n(t, \rho^u, \ln(Z')) = A(t)(\ln(Z'))^2 + B(t)(\ln(Z')) + C(t) \quad (5.10)$$

In each time step of calculation, a proportional strain path is assumed. Failure is reported when the damage value D reaches unity.

5.5 Rectangular cup warm forming

A systematic investigations on the formability of 0.9mm thick aluminum sheet materials (Al 5754, Al 5182+Mn, and Al 6111 T4) under warm forming conditions were conducted by Prof. Ghosh's group at the University of Michigan (Li and Ghosh 2003, Li and Ghosh 2004, Kim et al. 2006). Under warm forming conditions, they determined formability using tensile tests (Li and Ghosh 2003), and using a rectangular cup draw (Li and Ghosh 2004). They also include FEM simulation modeling and failure analysis of the rectangular cup draw process (Kim et al 2006). The systematic study provided valuable data to validate the other developments, i.e. based on the experimental data from the rectangular cup draw, Kim et al. (2007) developed an ANN based optimization algorithm to optimize the warm forming process. Recently, Lin et al. (2014) used the forming limit results from the rectangular cup draw to validate their continuum damage model for predicting forming limit.

In this study, the experimental data from the tensile tests and the rectangular cup experiment on 0.9mm thick sheet material Al 5182+Mn under non-isothermal warm forming condition is used to calibrate and validate the developed criterion. Table 6.2 gives the chemical composition of Al 5182+mn.

Table 5.2 Chemical composition of Al 5182+Mn (wt.%) (Li and Ghosh 2003)

| Si | Fe | Cu | Mn | Mg | Al |
|------|------|------|------|------|---------|
| 0.07 | 0.22 | 0.03 | 1.26 | 4.05 | Balance |

Figure 5.3a gives schematic of the cup draw experiment equipment setup. The forming experiment was carried out in three steps: 1) the die and punch were preheated to the desired temperature levels of 200°C-350° by embedded heating elements; 2) a rectangular sheet blank was clamped and heated by blank holder and die; 3) after thermal equilibrium was reached between sheet blank and die surfaces, punch draw sheet material into die opening at a constant speed of 10mm/s.

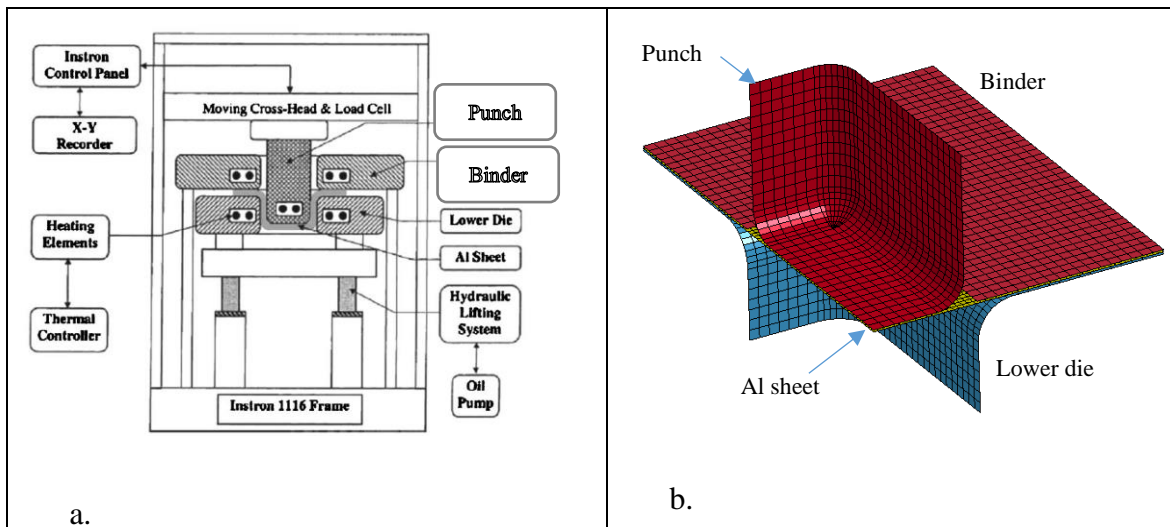


Figure 5.3 Experimental and simulation setup for warm forming: (a) experimental tooling setup; (b) a quarter of simulation model setup. Dimensions are listed in Table 5.3 (Li and Ghosh 2004)

5.5.1 FEM model

In this study, the warm forming process is modeled by using thermal mechanical coupled explicit and implicit FEM codes LS-DYNA 971 R7. Due to the symmetric nature of the problem, only a quarter of the geometry was modeled as shown in Figure 5.3 b. Table 5.3 gives the detail geometrical dimensions of the tooling components and boundary conditions.

Table 5.3 Dimensions of the tools and boundary conditions in simulation (Li and Ghosh 2004)

| Material | A15182+Mn |
|--|-----------------|
| Cross-section of die opening (mm x mm) | 110 x 50 |
| Cross-section of punch (mm x mm) | 104 x 44 |
| Die corner radius (mm) | 8.5 |
| Punch corner radius (mm) | 6.5 |
| Blank geometry (mm x mm x mm) | 0.9 x 200 x 140 |
| Thermal conductivity of the sheet material (W/°C) | 220 |
| Heat capacity of the sheet material (J/kg K) | 904 |
| Thermal conductivity of the tool material (W/°C) | 70 |
| Heat capacity the tool material (J/kg °C) | 450 |
| Interface contact heat conductance (W/°C) | 4.5 |
| Punch speed (mm/s) | 10 |
| Die/Binder/Punch temperature (°C) | 200,250,300,350 |
| Initial blank temperature (°C) | 25 |
| Blank holder pressure (MPa) | 1.1 |

The sheet blank is meshed with 4158 quad elements of an average edge length of 1.3mm while tooling components are meshed with mixed elements (quad and triangular) of sizes ranging from 2mm to 0.5mm. With such setup, punch and die radii are meshed by more than 6 elements to provide a good representation of curvature (Tang and Pan 2007). Tooling components and sheet metal blank were modeled as thermal shell elements. Tooling components were modeled as rigid body while the sheet blank was modeled as an elastic-viscoplastic material with thermal effects (MAT 106). After Kim et al. (2006), Isotropic material behavior and a Von Mises yield surface were assumed. Fully integrated formulation was chosen for the shell elements. A mass scaling of 8400% was used to

artificially increase calculation time step. Under this setup, the kinematic energy is kept below 0.1% of internal energy, at which the dynamic effect is trivial (Tang and Pan 2007).

Regarding the boundary condition, the displacement of die is constrained while the punch and binder are allowed to move freely in vertical direction. The gap between blank holder and die surface is kept at 0.95mm to ensure around 5MPa pressure at interfaces between blank and die/blank holder to prevent wrinkling. The friction at interfaces between tooling components and sheet material plays an important role in regulating the metal flow. For given lubrication and surface condition, the coefficient of friction at the interfaces between blank and tooling components is a function of many factors, such as pressure, temperature, and velocity of metal flow. Different friction coefficients were used by different studies. For example, Kurukuri et al. (2009) suggested that friction coefficients ranging from 0.12 to 0.18 at temperature above 150°C in their warm forming FEM modeling study on Al-Mg sheet material. Based on flat sheet drawing tests on Al-Mg alloy (Al5083), Naka et al. (2000) reported that the friction coefficient increases with increasing temperature ($\mu=0.25\sim 0.3$ at 200°C). Kim et al. (2006) found that using a high value of 0.5 can achieve a good correlation of strain prediction in their simulation modeling on Al5182+Mn. In this study, based on preliminary comparisons of strain distribution between FEA and experiments, the coefficient of friction at the interfacial contact between the tooling components and the blank is chosen at a constant value of 0.25. The thermal properties used in this study are suggested by (Kim et al. 2006).

5.5.2 Modeling flow stress

The flow stress at different temperatures and strain rates are expressed by a set of baseline flow stress curves while the strain rate effect is calculated by the Cowper-

Symonds equation Eq.(2.8). The strategy used in Chapter 2.4.1 is used to determine values of C and P at different temperatures. Based on FEM simulation calculation on the investigated cup draw process, the strain rate on the deformed area ranges from 0.1 s^{-1} to 1.0 s^{-1} . Flow stress curves at temperatures ranging from 200°C to 350°C at strain rate of 0.1 s^{-1} were chosen as baseline while those at strain rate of 1.0 s^{-1} were used as target values for determining C and P in Eq. (2.8). Based on tensile test data from (Li and Ghosh 2004), the baseline flow stress curves and target flow stress curves were generated by using the flow stress model (Sheng and Shivpuri 2006¹) given by below:

$$\sigma = K(\log(Z/2))\bar{\varepsilon}^{n(\log(Z/2))} \quad (5.11)$$

From the tensile stress-strain diagrams at temperatures from 200°C to 350°C and strain rates from $0.015/\text{s}$ to $1.5/\text{s}$ in (Li and Ghosh 2003), K and n in Eq. (5.11) were determined by regression as:

$$K = -9.33\log^2(Z/2) + 381.33\log(Z/2) - 2893.2 \text{ MPa}$$

$$n = -0.00008\log^2(Z/2) + 0.0125\log(Z/2) + 0.0197$$

The R^2 for the data fit were at 0.956 and 0.96, respectively for these two approximation functions. The model calculated flow stress curves match well with the tensile test measurement as shown in Figure 5.4 a and b. Based on this model, flow stress curves for work hardening stage at four different temperatures (200°C , 250°C , 300°C , and 350°C) and two different strain rates of $0.1/\text{s}$ and $1.0/\text{s}$ are calculated as shown in Figure 5.4 c and d.

C and P at different temperatures were generated by minimizing the difference between the target flow stress at strain rate of $1.0/\text{s}$ and the flow stress obtained from Eq.

(5.12) using flow stress curves at strain rate of 0.1/s. Table 5.4 gives the obtained C and P values.

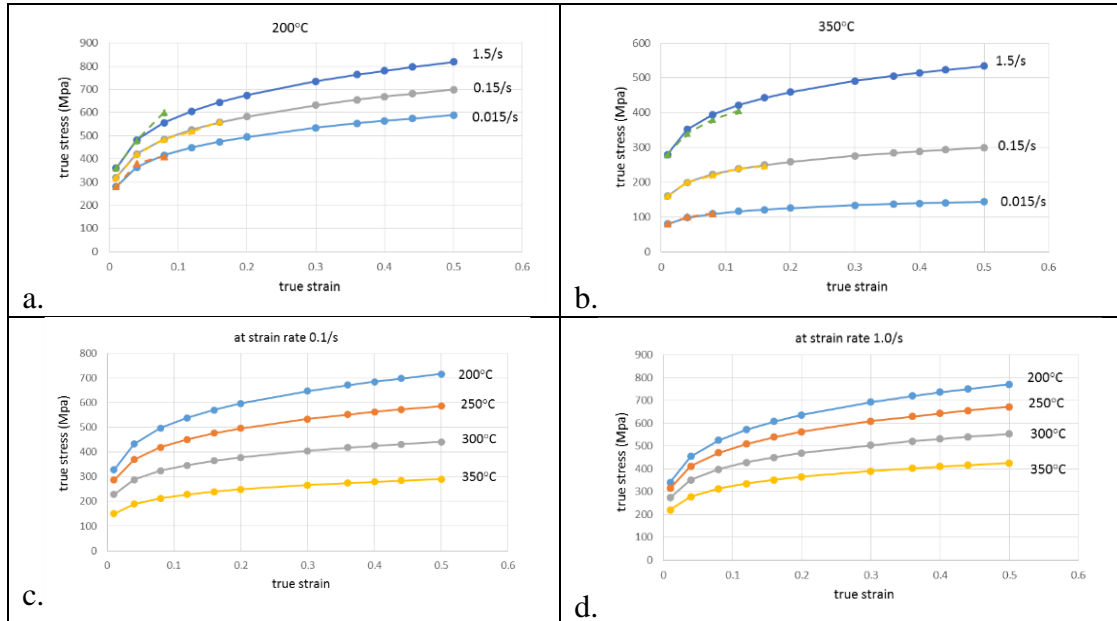


Figure 5.4 Flow stress curves for Al5182+Mn at elevated temperatures – solid line and round marked curves are calculated from Eq.(5.11); in a and b, dash line and triangular marked curves are from tensile test (Li and Ghosh 2004)

Table 5.4 Material parameters C and P in the Cowper and Symonds equation

| | Temperature (°C) | | | |
|-----|------------------|-----|------|-----|
| | 200 | 250 | 300 | 350 |
| C | 80 | 14 | 8.0 | 3.2 |
| P | 1.6 | 1.3 | 1.45 | 1.6 |

5.5.3 Calibration the DFC criterion

The material constants for approximating limit major strain under uniaxial tension $\varepsilon_1^n(t, \rho'', \ln(Z'))$ are determined by using tensile test from (Li and Ghosh 2003), see data points and approximation process in section 5.2. For a given sheet material the initial sheet

thickness t is a constant value. Then, the limit major strain under uniaxial tension can be expressed as:

$$\varepsilon_1^n(t, \rho'', \ln(Z')) = 0.0027 \ln^2(Z') - 0.228 \ln(Z') + 4.9 \quad (5.12)$$

The material constants in the effect function of Eq.(6.9), which was determined by using forming limit data on Al5083 sheet material, will be used. The use of this effect function is based on an assumption that the strain path and thickness effect on the forming limit of sheet materials of Al-Mg alloy system can be represented by same effect function.

The calibrated DFC is then used to identify failure in two non-isothermal forming conditions. In case one, the blank holder and die temperature is kept at 350°C while the punch temperature is kept at 200°C. In case two, the blank holder and die temperature is kept at 350°C while punch temperature is kept at 200°C.

5.5.4 Results and discussion

Case 1. $T_{\text{die-binder}}=350^\circ\text{C}$, $T_{\text{punch}}=200^\circ\text{C}$

The accuracy of the FEM modeling is validated by comparing the strain distribution along both major and minor axes of the rectangular cup part at moment of failure (part depth of 21mm). Figure 5.5 gives predicted in-plane principal strains and comparison with experimental measurement along longitudinal and transverse directions. To consider the bending effects, the predicted in-plane principal strains are reported at integration point locates at inner surface (towards punch surface). Comparison shows that simulation predicted strains match quite well with experimental measurement. Relatively large discrepancies can be observed at the transverse direction. The ignorance of anisotropic

effect and uncertainties in the measurement of small strains could be factors for causing the discrepancies.

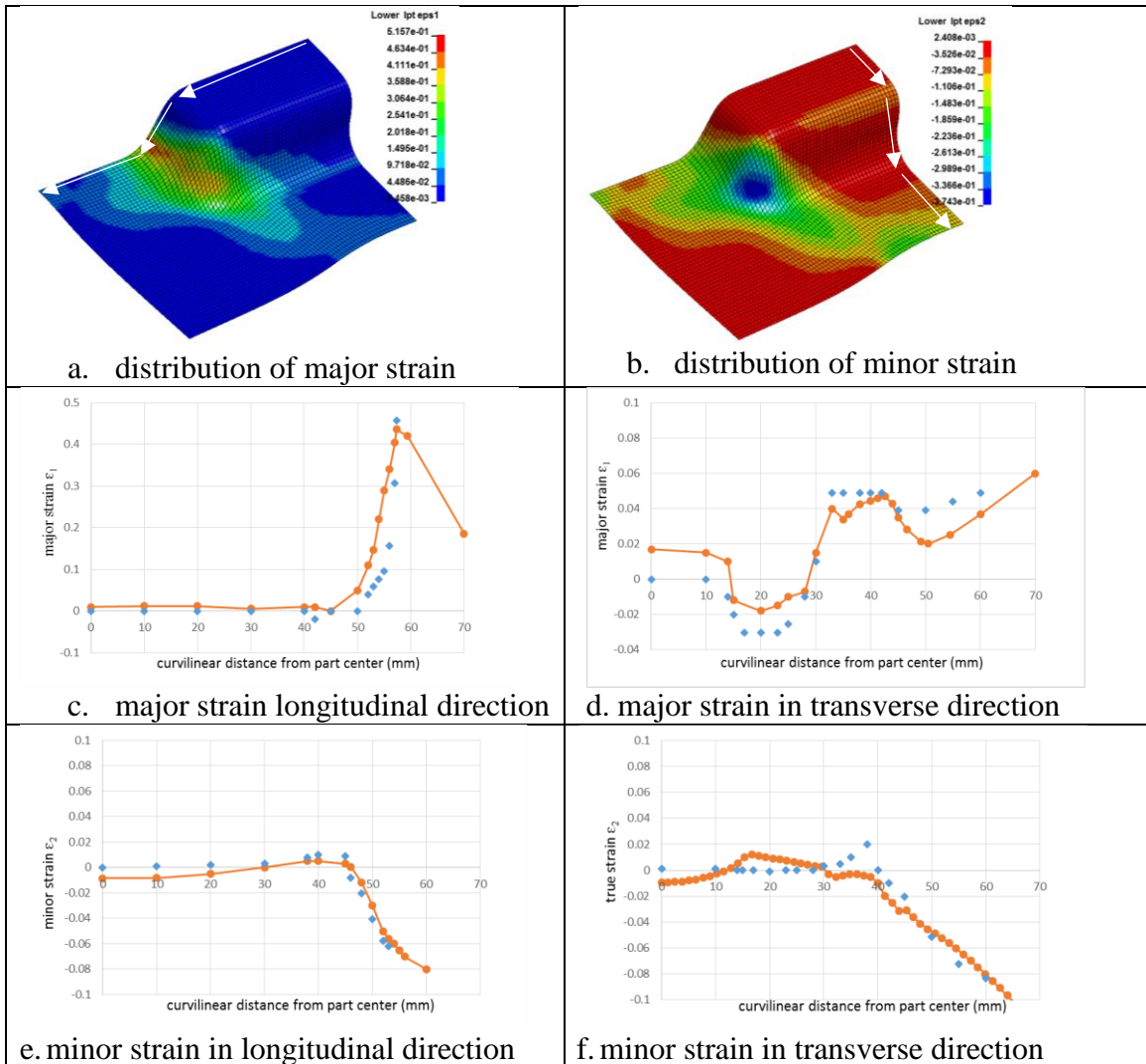


Figure 5.5 Comparison on in-plane principal strain distribution at failure depth of 21.0mm

Figure 5.6a and b show the calculated damage distribution at the outer surface (towards die cavity) and inner surface (towards punch) of the formed cup. At draw depth of 21.0mm, the calculated damage of inner surface at die curves area reaches unity while the damage values of the outer surface are still below unity. This can be explained by the bending effecting (Li et al. 2010). The predicted location of failure and failure draw depth

matches very well with experimental observation, in which the cup failure was measured at depth of 21.0mm as shown in Figure 5.6c. Figure 5.6d gives a plot of damage evolution at the cross section, which shows the maximum damage is always around the die curve area and increases with the progress of punch motion.

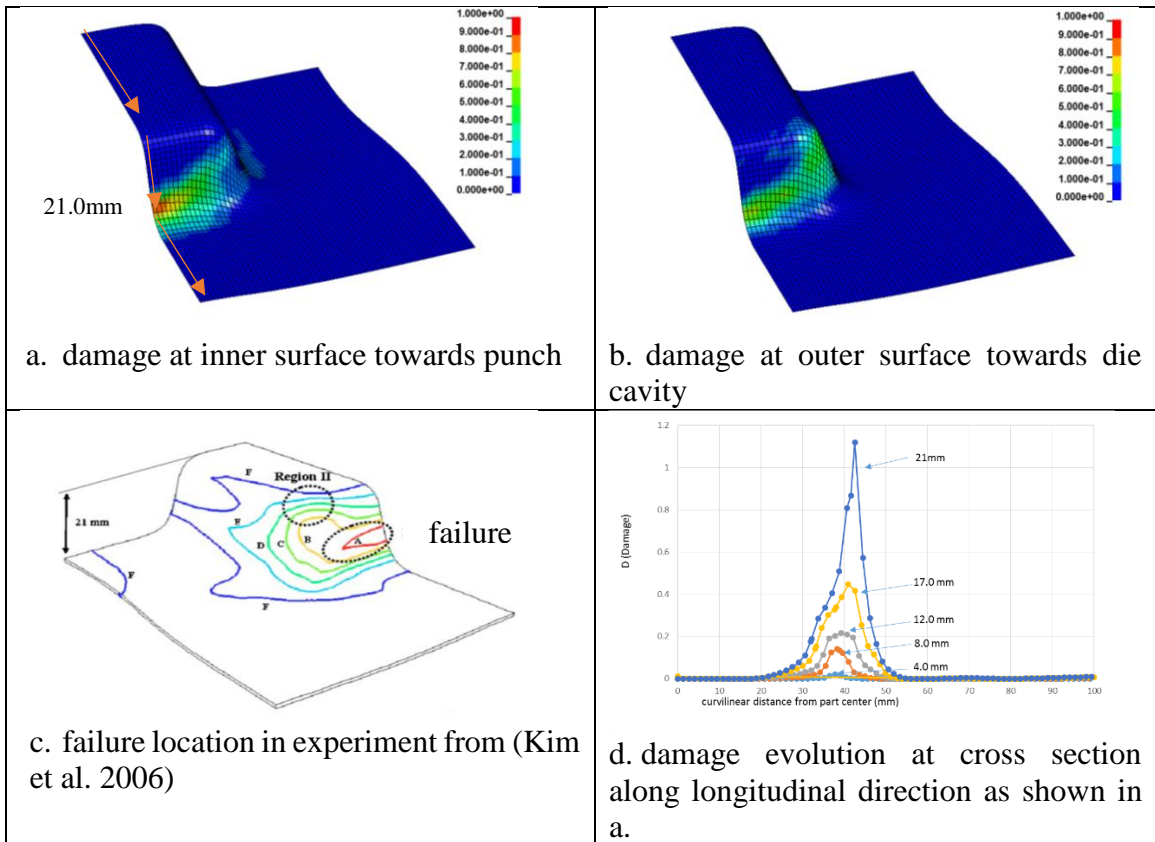


Figure 5.6 Damage prediction on the case 1

Figure 5.7a and b give temperature distribution and effective strain rate distribution, respectively. The temperature distribution shows that the temperature of workpiece under punch ranges from 218°C to 245°C while the area under blank holder is around 350°C. The strain rate distribution shows that majority of deformation happens at effective strain rate from 0.1/s to 1.0/s.

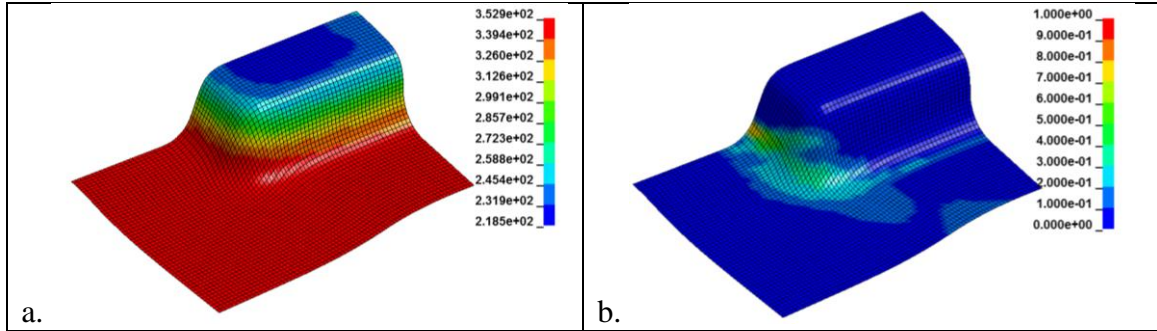
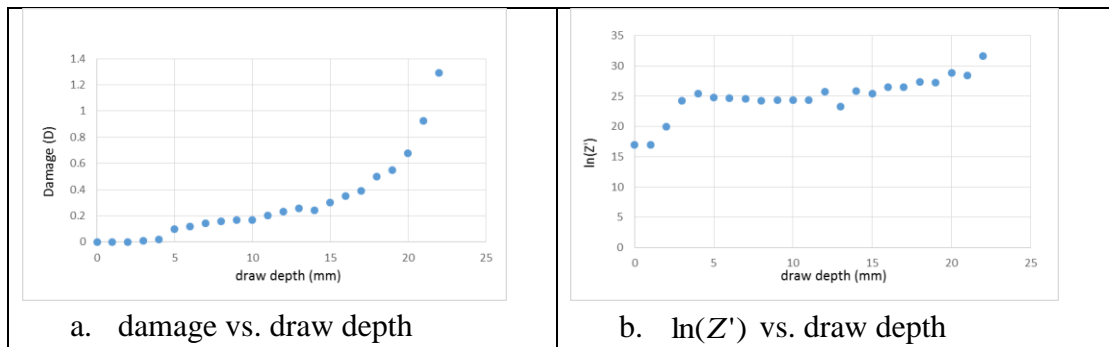


Figure 5.7 Prediction on the case 1:a. temperature distribution at draw depth of 21.0mm; b. effective strain rate distribution at draw depth of 21.0mm

Figure 5.8 gives the details of damage calculation of the critical failure element, at which the failure initiation was detected at draw depth of 21.0mm. Figure 6.8a shows that its damage value increase slowly till draw depth of 15mm, then increases at a faster pace and finally passes unity at draw depth of 21mm. The increase of damage is a combination effect of $\ln(Z')$ (Figure 5.8b), which increases with the increase of draw depth due to the drop of temperature (Figure 5.8c) and increase of effective strain rate (Figure 5.8d), and increase of major strain (Figure 5.8e). Due to the strain path (Figure 5.8f) is in the compression tension domain, the strain ratio at each time step starts at plane strain then descends to uniaxial tension (-0.5) at draw depth of 10mm, then gradually increases to plane strain at draw depth of 21mm as shown in Figure 5.8g. Correspondingly, the effect function value varies between 1.0 to 1.24 as shown in Figure 5.8h.



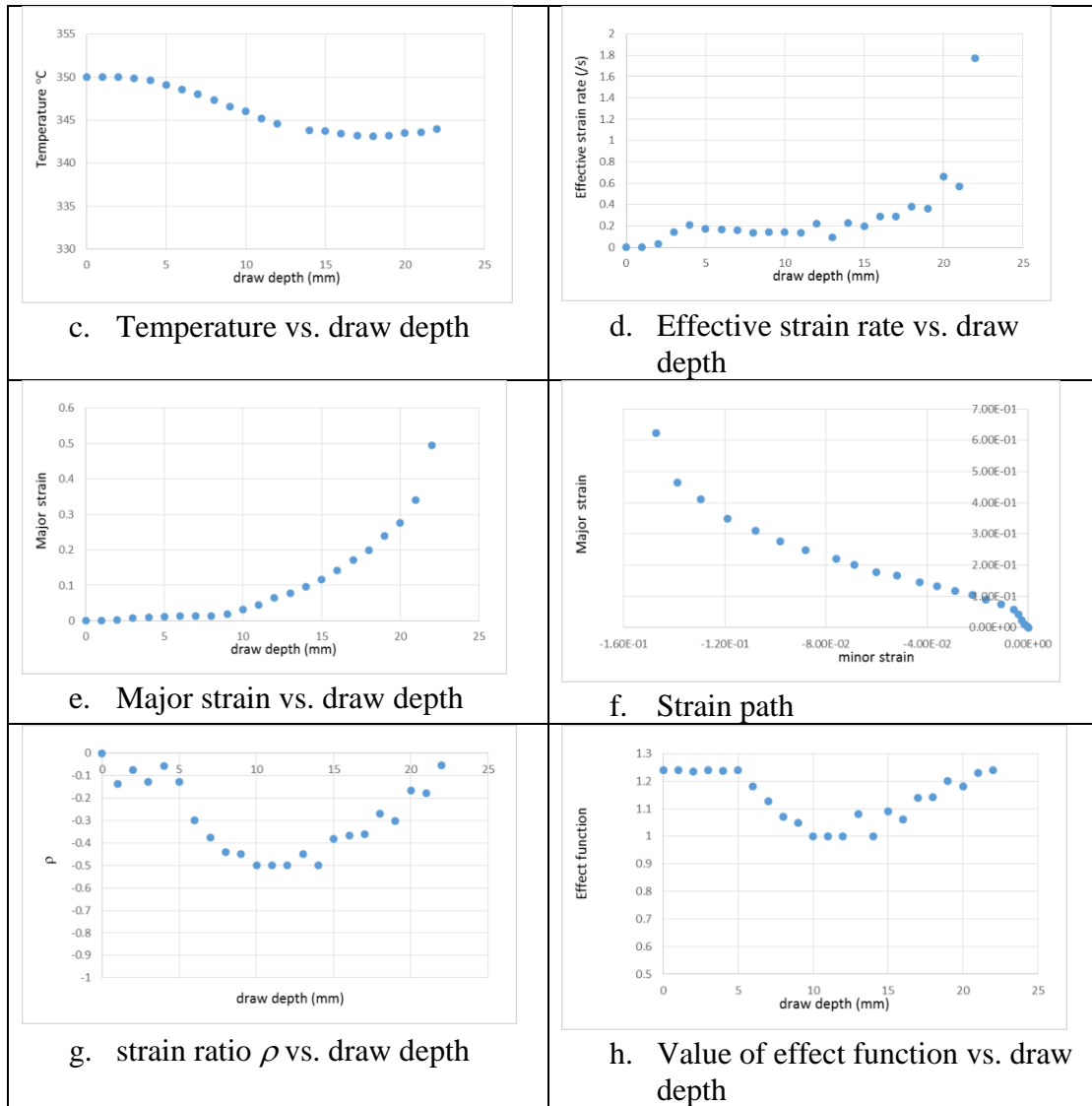


Figure 5.8 Evolution of damage of the critical element

Case 2 $T_{\text{die-binder}}=200^{\circ}\text{C}$, $T_{\text{punch}}=350^{\circ}\text{C}$

In the case 2, the damage is calculated at outer surface to consider the bending effect. The failure is identified at draw depth of 11.0 mm, at which the calculated max damage reaches a unity at area under the punch radius, see damage distribution shown in Figure 5.9 a. The damage evolution at the cross section shows that the maximum damage always around punch radius and grows with the increase of draw depth as show in Figure 5.9 b. The predicted location and failure depth match quite well with experimental

observation as given in Figure 5.9 c. The predicted failure depth is only 0.5mm deeper than the experimental observation (<5%). Such difference is within the error of experimental measurement. Compared with Case 1, the failure location shifts from die curve to punch radius is majorly due to softening tendency caused by the higher punch temperature. Due to the bending effect, at same depth, the damage values on the formed cup on the inner surface do not reach unity as shown in Figure 5.9 d.

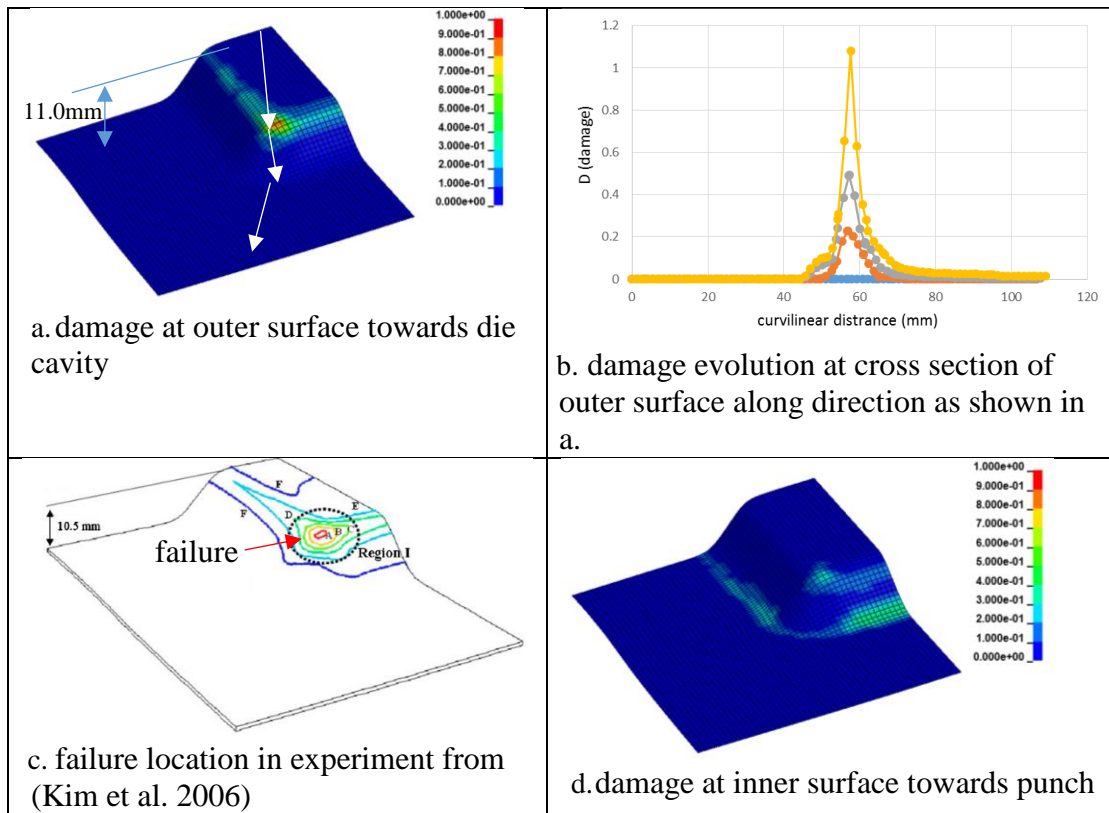


Figure 5.9 Damage prediction on the case 2

5.6 Conclusions and discussion

The ductile failure criterion proposed in Chapter 4 is further improved for modeling forming limit in warm forming conditions. In the improvement, the improved Zener-Hollomon parameter Z' , which is proposed in Chapter 3, is used to represent strain rate and temperature effect on the limit strain and effect function. The proposed the method is

validated by predicting a set of FLCs for sheet material JIS-A5083P-O and stretching failure in a rectangular cup draw on Al5182+Mn sheet material in warm forming conditions. Comparison shows that the prediction match quite well with experimental observations.

Besides the demonstrated accuracy, the benefits of this proposed DFC can be summarized as:

- 1) Easiness of calibration. With the determined effect function, the DFC only needs a calibration at uniaxial tension test. Because of this, the cost and time for obtaining forming limit can be largely reduced, which is especially valuable for the determination of FLCs at elevated temperatures.
- 2) Easiness of implementation with FEM simulation. Since the risk of failure is represented by only one parameter of D, the method is quite user friendly.

5.7 References:

- Abu-Farha F. 2011. The development of a forming limit surface for 5083 aluminum alloy sheet. *JOM* 63.11, p 72-78.
- Alexandrov, S., Wang, P.T., and Roadman R.E. 2005. A Fracture Criterion of Aluminum Alloys in Hot Metal Forming, *J. Mat. Processing Tech.*, 160, 2005, p 257-265
- Ashby, M.F., Gandhi, C. and Taplin, D. M. R. 1979. Overview No. 3 Fracture-mechanism maps and their construction for fcc metals and alloys. *Acta metallurgica* 27, no. 5. Pp. 699-729.
- Banabic D. 2010. *Sheet metal forming processes: constitutive modelling and numerical simulation*. Springer Science & Business Media.
- Bruschi, S., Altan, T., Banabic, D., Bariani, P. F., Brosius, A., Cao, J., & Tekkaya, A. E. 2014. Testing and modelling of material behaviour and formability in sheet metal forming. *CIRP Annals-Manufacturing Technology*, 63(2), 727-749.
- Chong, E. K., & Zak, S. H. 2013. *An introduction to optimization* (Vol. 76). John Wiley & Sons.
- Jie, M., Chow, C. L., & Wu, X. 2011. Damage-coupled FLD of sheet metals for warm forming and nonproportional loading. *International Journal of Damage Mechanics*, 20(8), 1243-1262.

Gese, H., & Dell, H. 2006. Numerical Prediction of FLC with the Program CRACH. *Proceedings of FLC Zurich 2006*.

Graf, A., & Hosford, W. F. 1993. Calculations of forming limit diagrams. *Metallurgical Transactions A*, 21(1), 87-94.

Hsu, E., Carsley, J. E., & Verma, R. (2008). Development of forming limit diagrams of aluminum and magnesium sheet alloys at elevated temperatures. *Journal of materials engineering and performance*, 17(3), 288-296.

Kim, H.K. and Kim, W.J., 2010. Failure prediction of magnesium alloy sheets deforming at warm temperatures using the Zener-Holloman parameter. *Mechanics of Materials*, 42(3), pp.293-303.

Kim, H. 2005. Investigations for warm forming of lightweight sheet materials: Process optimization. *University of Michigan*.

Kim, H. S., Koc, M., Ni, J., & Ghosh, A. 2006. Finite element modeling and analysis of warm forming of aluminum alloys—validation through comparisons with experiments and determination of a failure criterion. *Journal of Manufacturing Science and Engineering*, 128(3), 613-621.

Kröhn, M.A., Leen, S.B. and Hyde, T.H., 2007. A superplastic forming limit diagram concept for Ti-6Al-4V. *Proceedings of the Institution of Mechanical Engineers, Part L: Journal of Materials Design and Applications*, 221(4), pp.251-264.

Kurukuri, S., Van den Boogaard, A.H., Miroux, A. and Holmedal, B., 2009. Warm forming simulation of Al–Mg sheet. *Journal of Materials Processing Technology*, 209(15), pp.5636-5645.

Li, D., & Ghosh, A. 2003. Tensile deformation behavior of aluminum alloys at warm forming temperatures. *Materials Science and Engineering: A*, 352(1), 279-286.

Li, D., Ghosh, A. 2004. Biaxial warm forming behavior and stretchability of sheet alloys, *J. Mater. Process. Technol.* 145, pp.281-293. DOI: 10.1016/j.jmatprotec.2003.07.003

Lin, J., Mohamed, M., Balint, D., & Dean, T. A. (2014). The development of continuum damage mechanics-based theories for predicting forming limit diagrams for hot stamping applications. *International Journal of Damage Mechanics*, 23(5), 684-701.

Mallick, P.K. (Ed.). 2010. *Materials, design and manufacturing for lightweight vehicles*. Elsevier.

Naka T., Torikai G., Hino R., Yoshida F. 2001. The effects of temperature and forming speed on the forming limit diagram for type 5083 aluminum-magnesium alloy sheet, *J. of Mat. Proc. Technol.*, 113, pp.648-653.

Neugebauer, R., Altan, T., Geiger, M., Kleiner, M., Sterzing, A. 2006. Sheet metal forming at elevated temperatures, *CIRP Annals-Manufacturing Technology* 55(2), pp. 793-816

Sheng, Z. Q., & Shivpuri, R. 2006¹. Modeling flow stress of magnesium alloys at elevated temperature. *Materials Science and Engineering: A*, 419(1), 202-208.

Sheng Z.Q., and Shivpuri R. 2006². A Hybrid Process for Forming Thin-Walled Magnesium Parts, *Mater. Sci. Eng.*, A428, pp. 180-187. DOI: 10.1016/j.msea.2006.04.115

Sheng Z.Q. 2012. A Temperature and Time Dependent Forming Limit Surface for Sheet Metal Forming at Elevated Temperatures. *SAE International J. of Materials & Manufacturing*, 5.2, 2012, pp. 277-284.

Sheng Z.Q. 2015. A ductile necking criterion for sheet forming limit, *North American Deep Draw*

Research Group Fall Meeting, Oakland University, Oakland Center, December 10th, 2015

Stoughton, T. B., & Yoon, J. W. (2012). Path independent forming limits in strain and stress spaces. *International Journal of Solids and Structures*, 49(25), 3616-3625.

Tang, S. C., & Pan, J. 2007. *Mechanics modeling of sheet metal forming*. SAE international.

Tari, D. G., & Worswick, M. J. 2015. Elevated temperature constitutive behavior and simulation of warm forming of AZ31B. *Journal of Materials Processing Technology*, 221, 40-55.

Tebbe, P.A., Kridli, G.T. 2004. Warm forming of aluminium alloys: an overview and future directions. *International Journal of Materials and Product Technology*, 21(1), pp. 24-40.

Toros, S., Ozturk, F., & Kacar, I. 2008. Review of warm forming of aluminum–magnesium alloys. *Journal of materials processing technology*, 207(1), 1-12.

Yao, H., & Cao, J., 2002. Prediction of forming limit curves using an anisotropic yield function with prestrain induced backstress. *International journal of plasticity*, 18(8), 1013-1038.

Zener, C., and Hollomon, J.H. 1944. Effect of strain rate upon plastic flow of steel, *Journal of Applied physics* 15, no. 1, 1944, p 22-32.

Zhang, X. M., Zeng, W. D., Ying, S. H. U., Zhou, Y. G., Zhao, Y. Q., Huan, W. U., & Yu, H. Q. 2009. Fracture criterion for predicting surface cracking of Ti40 alloy in hot forming processes. *Transactions of Nonferrous Metals Society of China*, 19(2), 267-271.

CHAPTER 6: Conclusions and Recommendations of Future Work

Several developments have been carried out in this PhD study to improve the proposed the Z-FLS concept. Those developments include: 1) developing a ductile failure criterion (DFC), which provides a correct reflection of micromechanical findings on the strain path effect and initial sheet thickness effect on the critical damage; 2) proposing an improved Zener-Hollomon parameter (Z'), which can provide enhanced capability on reflecting strain rate and temperature effect on limit strain; 3) based on the proposed DFC and Z' , developing a method to predict forming limit under different strain rates and different temperatures. The developed approaches are validated by predicting: 1) FLCs for more than fourteen different steel, aluminum and magnesium sheet materials under linear and nonlinear strain paths; 2) failure in warm forming on the sheet materials of aluminum alloys and magnesium alloys; 3) failure in hot stamping of boron steel. The predictions match quite well with the published experimental data and observations.

Compared with numerous available approaches for predicting and modeling sheet metal forming limit, merits of the developed approach can be summarized as follows:

- 1) A correct reflection of strain path and initial sheet thickness effect on the critical damage.

- 2) Due to the correct reflection and proposed phenomenological determination of effect function, the criterion can be calibrated by the test data from uniaxial tension only. Such a feature is especially valuable for predicting forming limits at elevated temperatures, at which experimentally determining forming limits is very costly, and sometimes is even impossible.
- 3) With the proposing Z' , which considers the strain rate and temperature effect, the damage in warm sheet forming can be succinctly represented by one relative damage parameter D .
- 4) Due to the strain path independent feature, the DFC is less sensitive to the strain path change.

For future work, the developed technologies in this study can be implemented to predict failure in forming more complex geometries at both room and elevated temperatures. Since stretching failure in sheet metal forming is a complex issue, other failure modes, such as shear fracture in the low stress triaxiality range and fracture in connection with pure bending or bending with tension, can be investigated in the future work.

PUBLICATIONS AND PRESENTATIONS

Publications

Sheng Z.Q. 2012. A Temperature and Time Dependent Forming Limit Surface for Sheet Metal Forming at Elevated Temperatures. SAE International J. of Materials & Manufacturing, 5.2, 2012, pp. 277-284.

Sheng, Z., Wang, Y., Chang, T., Miller, R., & Liasi, E., 2013. Deep Drawing by Indirect Hot Stamping (No. 2013-01-1172). SAE Technical Paper.

Sheng, Z., Mallick, P.K., Predicting Forming Limit Curve by Using a New Ductile Failure Criterion, (No.2017-17M-0121). SAE Technical Paper. (Accepted)

Sheng, Z.Q, Mallick, P.K., Predicting Sheet Forming Limit of Aluminum Alloys for Cold and Warm Forming by Developing a Ductile Failure Criterion, MACE 2017-2956, Proceedings of the Manufacturing Science and Engineering Conference ASME 2017 MSEC, June 4-8, 2017, Los Angeles, CA, USA (Accepted and recommended for ASME journal publication)

Sheng, Z.Q., Mallick, P.K., A Ductile Failure Criterion for Predicting Sheet Metal Forming Limit, International Journal of Mechanical Science (submitted)

International presentations

Sheng, Z.Q., Forming limit surface: Theoretical Study and Implementation, SAE 2014 World Congress, April 8-10, Detroit, MI, USA

Sheng, Z.Q., Prediction of Fracture in Warm/Hot Forming using Strain Rate and Temperature Dependent Forming Limit Surface, SAE 2016 World Congress, April 12-14, Detroit, MI, USA

Sheng, Z.Q., Predict fracture in warm forming magnesium alloy sheet material by using Zener-Hollomon parameter based forming limit surface, Modeling, Simulation & Crash Safety congress, Jan. 26-27, 2016, Detroit, MI, USA (Invited speaker)

Sheng, Z.Q., Model and Predict Forming Limit of Aluminum Alloy Sheet materials at room and elevated Temperatures by Developing a Ductile Failure Criterion, Global Automotive Lightweight Materials ASIA, Sep. 28-29, 2016, Grand Hyatt Shanghai, Shanghai, China (Invited speaker)

APPENDIX A: NADDRG Formula

Based on a survey of a wide range of steels, Keeler and Brazier (1977) came up with following equation to calculate limit major strain at plain strain:

$$FLD_0 = \ln\left(1 + 1.11 * n * \left(1 + \frac{t}{1.65mm}\right)\right) \quad (A.1)$$

Where t is metal thickness measured in millimeters.

North American Deep Draw Research Group (NADDRG 1996) suggested that right and left side of FLC are approximated by two lines with slopes of about 20° and 45°, respectively.

APPENDIX B: Hill-Stören Rice (H-SR) Formula

Based on an assumption that LN instability occurs in the direction where zero extension holds in the plane of the sheet in the negative quadrant (Hill 1952), and bifurcation occurs in the positive quadrant of the FLD (Storen and Rice, 1975), a formula to calculate FLC is given as:

$$\varepsilon_1^{n-HSR} = \begin{cases} \frac{n}{1+\rho}, & (-1 \leq \rho \leq 0), \quad \text{negative quadrant} \\ \frac{3\rho^2 + n(2+\rho)^2}{2(2+\rho)(1+\alpha+\alpha^2)}, & (0 \leq \rho \leq 1), \quad \text{positive quadrant} \end{cases} \quad (\text{B.1})$$

APPENDIX C: Algebraic transformation of DFC

Considering the Cartesian reference axes which are parallel to the three symmetry planes of anisotropic behavior, assuming in-plane isotropy and proportional strain path, a special case of Hill's 48 yield criterion (Hill 1964) can be expressed as:

$$F = \sigma_1^2 - \frac{2r}{1+r} \sigma_1 \sigma_2 + \sigma_2^2 \quad (\text{C.1})$$

After (Liang and Hu 1987), under associated flow rule, rate of plastic strain can be expressed as:

$$\text{Major strain- } d\varepsilon_1 = \frac{d\bar{\varepsilon}}{\bar{\sigma}} \left(\sigma_1 - \frac{r}{1+r} \sigma_2 \right) \quad (\text{C.2})$$

$$\text{Minor strain- } d\varepsilon_2 = \frac{d\bar{\varepsilon}}{\bar{\sigma}} \left(\sigma_2 - \frac{r}{1+r} \sigma_1 \right)$$

$$\text{Effective strain- } d\bar{\varepsilon} = \frac{1+r}{\sqrt{1+2r}} \sqrt{d\varepsilon_1^2 + \frac{2r}{(1+r)} d\varepsilon_1 d\varepsilon_2 + d\varepsilon_2^2}$$

The effective stress can be calculated as:

$$\bar{\sigma} = \sqrt{\sigma_1^2 - \frac{2r}{(1+r)} \sigma_1 \sigma_2 + \sigma_2^2} \quad (\text{C.3})$$

In-plane stress ratio is defined by in-plane strain ratio $\rho = \frac{d\varepsilon_2}{d\varepsilon_1}$ as:

$$\alpha = \frac{\sigma_2}{\sigma_1} = \frac{(1+r)\rho + r}{(1+r) + r\rho} \quad (\text{C.4})$$

Replacing minor stress in Eq.(C.3) with Eq.(C.4), effective stress can be expressed as:

$$\bar{\sigma} = \sigma_1 \frac{\sqrt{1+2r} \sqrt{1 + \frac{2r\rho}{1+r} + \rho^2}}{((1+r) + r\rho)} \quad (\text{C.5})$$

Then, hydrostatic stress σ_m can be expressed as:

$$\sigma_m = \frac{(1+\alpha)}{3} \sigma_1 = \frac{(1+2r)(1+\rho)}{3((1+r) + r\rho)} \sigma_1 \quad (\text{C.6})$$

Replacing minor strain in Eq.(C.2), the incremental effective strain can be expressed as:

$$d\bar{\varepsilon} = \frac{1+r}{\sqrt{1+2r}} \sqrt{1 + \frac{2r\rho}{1+r} + \rho^2} d\varepsilon_1 \quad (\text{C.7})$$

From Eq.(C.5-7),

$$\eta d\bar{\varepsilon} = \frac{(1+r)(1+\rho)}{3} d\varepsilon_1 \quad (\text{C.8})$$

APPENDIX D: Calculation FLC based on Oyane's criterion

Oyane's criterion

$$\int_0^{\bar{\varepsilon}^f} \left(1 + \frac{\rho}{c_1}\right) d\bar{\varepsilon} = c_2 \quad (\text{D.1})$$

Where c_1 and c_2 are material constants. Under proportional strain path and isotropic material deformation assumption, Eq.D1 becomes:

$$\bar{\varepsilon}^f = \frac{c_1 c_2}{c_1 + \rho} \quad (\text{D.2})$$

Calibrating c_1 and c_2 by measuring failure effective strains at uniaxial tension ($\bar{\varepsilon}_u^f$) and plane strain ($\bar{\varepsilon}_p^f$). Then, c_1 and c_2 can be determined as:

$$c_1 = \frac{0.5\bar{\varepsilon}_u^f}{\bar{\varepsilon}_u^f - \bar{\varepsilon}_p^f} \quad (\text{D.3})$$

$$c_2 = \bar{\varepsilon}_p^f \quad (\text{D.4})$$

With determined c_1 and c_2 , replacing effective strain by Eq.C7, major limit strain can be calculated as:

$$\varepsilon_1^f = \frac{\sqrt{3}\bar{\varepsilon}_u^f \left(\frac{0.5\bar{\varepsilon}_u^f \bar{\varepsilon}_p^f}{(\bar{\varepsilon}_u^f - \bar{\varepsilon}_p^f)} \right)}{2 \left(\frac{0.5\bar{\varepsilon}_u^f}{(\bar{\varepsilon}_u^f - \bar{\varepsilon}_p^f)} + \rho \right) \sqrt{1 + \rho + \rho^2}} \quad (\text{D.5})$$

APPENDIX E: Abbreviations of approaches and tests of Benchmark #1 of Numisheet 2008 and 2014

Table E1 Approaches used in Numisheet 2008 Benchmark #1 (Volk et al. 2008)

| Participant | algorithm |
|--------------|-------------------------------------|
| Brunet | T_MF |
| Eyckens | T_MK |
| Gese | T_GG (Crach approach) |
| IVP | T_MF |
| Nara | N_GG |
| Sigvant 1 | N_NG |
| Sigvant 2 | N_NG |
| Vegter 1 | N_NG |
| Vegter 2 | N_NG |
| Vegter 3a -f | T_MK with different material models |
| Wagoner | N_GG |

Note: abbreviations of the algorithms: T_MF:= theoretical model with maximum force approach; T_MK:= theoretical model with Marcianiak-Kuzynski approach; T_GG: theoretical model (Crach approach) with generalized geometry; N_NG:= numerical model using the Nakajima geometry; N_GG:= numerical model using a generalized geometry

Table E2 Approaches used in Numisheet 2014 Benchmark #1(Wu 2013)

| Participants | Method |
|--------------|--|
| BM1-01 | FLC from BM |
| BM1-02 | Modified Mohr-Coulomb criterion |
| BM1-03 | Non-linear FLC |
| BM1-04 | CrachFEM |
| BM1-05 | Generalized Forming Limit Concept (GFLC) |
| BM1-06 | FLC analysis |
| BM1-07 | Keeler goodwin diagram |
| BM1-08 | N/A |
| BM1-09 | N/A |

Table E3 Abbreviations of test on TRIP780 sheet material in Numisheet 2014 Benchmark #1

| Abbreviation | Test |
|--------------|---|
| BKS1 | small size blank sample on die with insert using 1 shim |
| BKS4 | small size blank sample on die with insert using 4 shims |
| BKM1 | medium size blank sample on die with insert using 1 shim |
| BKM4 | medium size blank sample on die with insert using 4 shims |
| BKF1 | full size blank sample on die with insert using 1 shim |
| BKF4 | full size blank sample on die with insert using 4 shims |

APPENDIX F: Script for Damage Calculation in LS-Prepost

```
void main(void)
{
    Int numState;
    Int numShellEle;
    Int i = 0;
    Int j = 0;
    char buf[256];
    Float *TF = NULL;
    Float *stress1 = NULL;
    Float *stress2 = NULL;
    Float *stress3 = NULL;
    Float *stress4 = NULL;
    Float *stress5 = NULL;
    Float *stress6 = NULL;
    Float *strain1 = NULL;
    Float *strain2 = NULL;
    Float *strain3 = NULL;
    Float *fldeps1 = NULL;
        Float *fldeps10 = NULL;
    Float *fldeps2 = NULL;
        Float *fldeps20 = NULL;
        Float *luo = NULL;
        Float *luo0 = NULL;
    Float *VMstress = NULL;
    Float *meanstress=NULL;
    Float *effectiveStrain=NULL;
    Float *effectiveStrain0=NULL;
    Float *damage=NULL;
    Float *damage0=NULL;
        Float *relatdamage=NULL;
        Float *effectFunction=NULL;
        Float *effectFunction0=NULL;
        Float *effectFunction1=NULL;
        Float *temp=NULL;
        Float *effectFunction_o=NULL;
    numState = SCLGetDataCenterInt("num_states");
    numShellEle = SCLGetDataCenterInt("num_shell_elements");
```

```

TF = malloc(numShellEle*sizeof(Float));
stress1 = malloc(numShellEle*sizeof(Float));
stress2 = malloc(numShellEle*sizeof(Float));
stress3 = malloc(numShellEle*sizeof(Float));
stress4 = malloc(numShellEle*sizeof(Float));
stress5 = malloc(numShellEle*sizeof(Float));
stress6 = malloc(numShellEle*sizeof(Float));
strain1 = malloc(numShellEle*sizeof(Float));
strain2 = malloc(numShellEle*sizeof(Float));
strain3 = malloc(numShellEle*sizeof(Float));
fldeps1 = malloc(numShellEle*sizeof(Float));
    fldeps10 = malloc(numShellEle*sizeof(Float));
fldeps2 = malloc(numShellEle*sizeof(Float));
    fldeps20 = malloc(numShellEle*sizeof(Float));
    luo=malloc(numShellEle*sizeof(Float));
    luo0=malloc(numShellEle*sizeof(Float));
VMstress = malloc(numShellEle*sizeof(Float));
meanstress = malloc(numShellEle*sizeof(Float));
effectiveStrain = malloc(numShellEle*sizeof(Float));
effectiveStrain0 = malloc(numShellEle*sizeof(Float));
damage = malloc(numShellEle*sizeof(Float));
damage0 = malloc(numShellEle*sizeof(Float));
    relatdamage=malloc(numShellEle*sizeof(Float));
    effectFunction=malloc(numShellEle*sizeof(Float));
    effectFunction0=malloc(numShellEle*sizeof(Float));
    effectFunction1=malloc(numShellEle*sizeof(Float));
    temp=malloc(numShellEle*sizeof(Float));
    effectFunction_o=malloc(numShellEle*sizeof(Float));

for ( i = 1; i < (numState+1); i = i+1)
{
    SCLSwitchStateTo(i);

    /*Get stress for shell and middle layer*/
    /* char* username: compenont name
    * Int typename: 0=Whole, SHELL, TSHELL, BEAM, SOLID
    * Int ipt: MID, INNER, OUTER
    * Float** results: results array
    */

    numShellEle = SCLGetDataCenterFloatArray("stress_x",SHELL,INNER,&stress1);
    numShellEle = SCLGetDataCenterFloatArray("stress_y",SHELL,INNER,&stress2);
    numShellEle = SCLGetDataCenterFloatArray("stress_z",SHELL,INNER,&stress3);
    numShellEle =
SCLGetDataCenterFloatArray("stress_xy",SHELL,INNER,&stress4);

```

```

    numShellEle =
SCLGetDataCenterFloatArray("stress_yz",SHELL,INNER,&stress5);
    numShellEle =
SCLGetDataCenterFloatArray("stress_zx",SHELL,INNER,&stress6);
    numShellEle =
SCLGetDataCenterFloatArray("strain_1stprincipal_infin",SHELL,INNER,&strain1);
    numShellEle =
SCLGetDataCenterFloatArray("strain_2ndprincipal_infin",SHELL,INNER,&strain2);
    numShellEle =
SCLGetDataCenterFloatArray("strain_3rdprincipal_infin",SHELL,INNER,&strain3);
    numShellEle =
SCLGetDataCenterFloatArray("effective_plasitc_strain",SHELL,INNER,&effectiveStrain);
    numShellEle =
SCLGetDataCenterFloatArray("von_mises",SHELL,INNER,&VMstress);
    numShellEle =
SCLGetDataCenterFloatArray("lower_eps1",SHELL,OUTER,&fldeps1);
    numShellEle =
SCLGetDataCenterFloatArray("lower_eps2",SHELL,OUTER,&fldeps2);

/*process*/
for(j = 0; j < numShellEle; j = j+1)
{
    if ( i == 1)
    {
        damage[j] = 0.0;
        damage0[j] = 0.0;
        effectiveStrain0[j] = 0.0;
        fldeps10[j]=0;
                                fldeps20[j]=0;
                                effectFunction_o[j]=1.101;
    }
}

//effectiveStrain[j]=1.1547*(strain1[j]*strain1[j]+strain2[j]*strain2[j]+strain1[j]*strain2[j]);
//VMstress[j] = sqrt(0.5*((stress1[j]-stress2[j])*(stress1[j]-stress2[j])+(stress2[j]-stress3[j])*(stress2[j]-stress3[j])+(stress3[j]-stress1[j])*(stress3[j]-stress1[j])+6.0*(stress4[j]*stress4[j]+stress5[j]*stress5[j]+stress6[j]*stress6[j])));

    meanstress[j] = (stress1[j]+stress2[j]+stress3[j])/3.0;
    if ( VMstress[j] < 1.0e-7 )
    {
        TF[j] = 0;
    }
    else

```

```

{
  TF[j] = meanstress[j]/VMstress[j];
}
      if((fldeps1[j]-fldeps10[j])<1.0e-7)
      {
        if((fldeps1[j]-fldeps10[j])>0){
          luo[j]=1;
        }else{
          luo[j]=-0.5;
        }
      }else
      {
        luo[j]=(fldeps2[j]-fldeps20[j])/(fldeps1[j]-fldeps10[j]);
      }
      if (luo[j]>1.0){
        luo[j]=1;
      }else{
        if(luo[j]<-0.5){
          luo[j]=-0.5;
        }
      }
      effectFunction0[j]=1.101;
      effectFunction1[j]=3.966;
      if(((effectiveStrain[j]-effectiveStrain0[j])*abs(luo[j]-
luo0[j]))>0.0001){
        if(luo[j]<1e-7)
        {
          temp[j]=(1+luo[j])*(effectFunction0[j]-2*luo[j]*(2-
effectFunction0[j]));
          effectFunction[j]=temp[j];
        }
        else
        {
          effectFunction[j]=(1+luo[j])*(effectFunction0[j]+(-
0.414*luo[j]*luo[j]+1.414*luo[j])*(effectFunction1[j]*0.5-effectFunction0[j]));
        }
        }else{
          effectFunction[j]=effectFunction_o[j];
        }
      }
      damage[j] = TF[j]*(effectiveStrain[j]-effectiveStrain0[j])+damage0[j];
      relatdamage[j]=damage[j]*3/(0.33*effectFunction[j]);

effectiveStrain0[j] = effectiveStrain[j];
damage0[j] = damage[j];
      fldeps10[j]=fldeps1[j];
      fldeps20[j]=fldeps2[j];

```



```
        effectFunction_o[j]=effectFunction[j];
    }

    sprintf(buf, "damage_state_%d",i);
    // SCLSaveDCToFile(buf,numShellEle,damage);

    /* Int option: 0 = Whole element, SHELL, BEAM, TSHELL, SOLID, NODE
    * Int num: array size
    * Float* TF: TF array
    * Int ist: state index
    */
    SCLFringeDCToModel(SHELL,1,numShellEle,relatdamage,i,buf);
}
}
main();
```